

ELECTRICAL RESISTIVITY TOMOGRAPHY AND SELF-POTENTIAL SURVEYS TO CHARACTERIZE AND MONITOR THE VOLCANIC HYDROTHERMAL SYSTEM OF GUNNUHVER (ICELAND)

Elieen Vrancken

Student number: 01700282

Promotor: Prof. dr. Thomas Hermans

Jury: Prof. dr. Tom Bultreys , Prof. dr. Corentin Caudron

Master's dissertation submitted in partial fulfilment of the requirements for the degree of master in geology

Academic year: 2022-2023

Dedicated to my uncle, Tony († 28/01/2022) and my grandfather, Robert († 29/12/2022)

Acknowledgements

I would like to express my gratitude towards all the people who have supported and advised me during the past year. Without them this Master's dissertation would not be realised.

First of all I want to thank my thesis promoter professor Thomas Hermans for giving me the opportunity to work on this subject and join the team on the Gunnuhver field campaign. He invested a lot of time in me by giving continuous guidance, constructive feedback, support and motivation.

I am very grateful to Lore Vanhooren for her continuously guidance, even on sick leave, my questions were still answered. Thank you Lore for helping me to learn the working of CRTomo, making the meshes for the inversions in CRTomo, for always helping me with encountered problems and motivating me throughout the thesis semester.

I would like to thank everyone that helped during the field work in Iceland to collect the ERT and SP measurements. A special thanks to Warre, Hanne, Olivier, Lore and professor Hermans for setting up and testing the ERT equipment, digging a lot of holes for the SP measurements and helping with making and digitalizing the visual observations.

A word of thanks goes to my fellow geology students and Geologica for the great company during the last years. Some of them I would like to thank specifically for the welcome distraction of lunch talks from the long days of working on this dissertation. Thank you Hanne, Rosalia and Kimberly.

A very special thanks goes to my boyfriend Simon, for the continuous support, believing in me and encouraging me not to give up.

The last thanks goes to my family without whom all of this would never have been possible. Thank you little sister for bearing with me. And my parents, thank you for giving me the freedom to develop independently, for letting me follow my interests, for letting me choose my field of study and the chance to study at Ghent University. You always believed in me and supported me in every step of my life. Thank you!

Table of Contents

1	Introduction	1
1.1	General context	1
1.2	Research objectives	2
1.3	Thesis layout.....	2
2	Geological and literature overview	3
2.1	Geology of the study area	3
2.2	Volcanic hydrothermal systems.....	7
2.3	Electrical resistivity tomography in VHS	7
2.4	Self-potential in VHS.....	9
3	Material and methods	11
3.1	Electrical resistivity tomography	11
3.1.1	Principle of ERT	12
3.1.2	Measuring principle.....	12
3.1.3	Noise considerations	13
3.1.4	Inversion principle.....	14
3.1.5	Inversion principle with a reference model	15
3.1.6	Time-lapse inversion principle	15
3.1.7	ERT image appraisal tools	16
3.1.8	ERT field measurements	17
3.1.9	Pre-processing of ERT data	18
3.2	Self-potential method.....	19
3.2.1	General acquisition	20
3.2.2	Fundamentals of the self-potential method	21
3.2.3	SP measurements in the study area	22
3.3	Temperature, soil moisture, CO ₂ and precipitation data	23
4	Characterization study	25
4.1	Absolute inversion with error model	25
4.1.1	The constant error model	26
4.1.2	The variable error model	27
4.1.3	The individual error	27

4.2	Absolute inversion with a homogeneous reference model.....	28
4.2.1	The constant error model	28
4.2.2	The variable error model	30
4.2.3	The individual error	30
4.2.4	Discussion	31
4.3	Self-potential results	31
4.4	Discussion	32
5	Monitoring study	37
5.1	Absolute inversion with error model	37
5.2	Absolute inversion with a homogeneous reference model.....	39
5.3	Time-lapse inversion.....	40
5.3.1	Time-constrained inversion	41
5.3.2	Difference inversion	42
5.4	Results of temperature, soil moisture, CO ₂ and precipitation data.....	44
5.5	Discussion	47
6	Conclusion and future recommendations	50
	Bibliography	52
	Appendices	61
A.	Grid	61
B.	Characterization study	61
C.	Monitoring study	65

1 Introduction

1.1 General context

Volcanic hydrothermal systems (VHS) are three-phase reservoirs located between magma intrusions and the Earth's surface and can be found in most volcanoes on Earth. The complex interplay between gas, liquid, and rocks results in the dynamic behaviour of VHS, which is up to now poorly understood.

Geophysical and hydrochemical signals such as ground vibrations, self-potential, variable surface resistivity observables, or gas outflow can be created by fluid circulation in a VHS (Caudron et al., 2023; Finizola et al., 2002; Isaia et al., 2021). However, before volcanic eruptions occur, magmatic gases are not always observable. According to Symonds et al. (2001), many terrestrial volcanoes contain abundant surface or groundwater that scrubs magmatic gases until a dry pathway to the atmosphere is established (Symonds et al., 2001). Seismic methods are commonly used to monitor volcanic environments (Chouet & Matoza, 2013). The precursory signals such as local earthquakes can however remain limited before an explosion (Caudron et al., 2019).

The detection of pre-eruptive signals, the interpretation of the observed volcanic activity, and the linking between periods of volcano unrest and the actual events are complicated by the complex dynamics of fluid circulation. Volcanoes remain therefore on alert for months/years without experiencing any eruption. This affects the credibility of the agencies responsible for monitoring volcano activities.

Phreatic or hydrothermal eruptions can cause casualties such as during the Ontake eruption (Japan) in 2014 and the White Island eruption (New Zealand) in 2019 causing respectively 58 (Yamaoka et al., 2016) and 22 victims (Burton et al., 2021). Characterizing the dynamic behaviour of VHS is needed to understand the volcanic hydrothermal systems in more detail and its implications on geothermal systems and geohazards.

Variations in temperature, saturation, pore connections, and alteration are examples of dynamic processes occurring in the shallow part (< 150 m) of a VHS. The geophysical methods electrical resistivity tomography (ERT), induced polarization (IP), and self-potential or spontaneous potential (SP) are based on the electrical properties of the subsurface. These electrical properties can change through time because of e.g. water and gas flow created by volcanic activity and temperature changes (Dimech et al., 2022). Although ERT, IP, and SP are sensitive to volcanic activity, they have not been widely investigated to monitor VHS at a daily resolution so far, while using them to characterize volcanic environments is common practice (e.g. Grobber & Barde-Cabusson, 2019; Lévy et al., 2019).

For the research project ERupT, ERT monitoring was carried out to investigate if ERT can reveal the dynamic behaviour of a volcanic hydrothermal system. ERT, IP, and SP surveys were performed to characterize the study area. The Gunnhver area is the first study area in the scope of the ERupT project. It is a hydrothermal system located in the Reykjanes geothermal area in the southwest of Iceland. This Master's dissertation is carried out in the context of the ERupT project.

The Gunnhver area consists of Holocene lavas and tuff formations (Marks et al., 2010). Steam vents, hot ground, mud pools, emanating warm air from fractures, and surface alteration are geothermal manifestations occurring in this part of the Reykjanes geothermal area (Fridriksson et al., 2016).

1.2 Research objectives

The first research objective of this Master's dissertation is to characterize the study area with the results of the ERT, SP, and IP surveys. The ERT results are obtained by absolute inversions with different types of error models, and with and without a reference model. The results of the IP measurements are obtained by Warre Dekoninck in a companion thesis (Dekoninck, 2023).

Secondly, investigations of advanced inversion techniques for time-lapse ERT for the monitoring study using the knowledge obtained from the characterization study are performed. Except for the absolute inversions with and without a reference model, time-lapse inversions (difference and time-constrained inversion) are carried out with different types of error models.

1.3 Thesis layout

The relevant geologic information about the study area, more information about volcanic hydrothermal systems, and the use of the geophysical methods ERT, IP, and SP in volcanic hydrothermal systems are described in chapter two.

In chapter three, the geophysical methods ERT and SP, and the temperature, soil moisture, CO₂ flux, and precipitation measurements are explained. The methodology of the IP method can be found in the Master's dissertation of Dekoninck (2023).

To characterize the study area, the results obtained from the ERT, SP, and IP measurements are used in chapter four. These geophysical measurements were carried out along five profiles in the Gunnuhver area. For ERT, absolute inversions with three types of error models, and with and without a homogeneous reference model are carried out. The three types of error models are the constant linear error model, the variable linear error model, and the individual error. The constant linear error model has parameters that remain constant during the inversion of the five profiles. The variable linear error model has specific parameters for each profile. While the individual error consists of specific parameters for each measuring point of each profile. The SP signal is processed with the drift and reference correction.

In chapter five, the monitoring study is discussed using the data of ERT monitoring and the knowledge of the characterization study. Five chosen days are explained in more detail as examples for the monitoring results between 23 October 2022 and 27 February 2023. Absolute inversions with and without reference models, and with the constant and the variable linear error model are carried out. Also, two types of time-constrained inversions are used, namely the difference inversion and time-constrained inversion, with the constant and the variable linear error models.

The conclusion of the characterization and monitoring study of the Gunnuhver area and future recommendations are drawn in chapter six. The list of references is added after chapter six and is followed by the appendices.

2 Geological and literature overview

2.1 Geology of the study area

Iceland is located in the North Atlantic Ocean between Greenland and the Faroe Islands, at the junction of two large submarine physiographic structures, namely the Mid-Atlantic Ridge and the Greenland-Iceland-Faeroes Ridge. Iceland is a geologically young island formed 25 million years ago (Thordarson & Hoskuldsson, 2002). The Iceland Basalt Plateau results from the interaction of a deep-seated mantle plume and the spreading of the Mid-Atlantic Ridge (Marks et al., 2010). This Plateau rises 3000 m above the surrounding seafloor and 30% of the area is located above sea level. The Mid-Atlantic Ridge is the suture controlled by plate motions resulting in the divergent movement of the American plate in the west and the Eurasian plate in the east (Thordarson & Hoskuldsson, 2002). The hotspot under the ridge, the Iceland mantle plume is active since c. 61 Ma (Eiríksson & Símonarson, 2021). The volcanic activity is situated in the southwest to northeast aligned volcanic rift zones and intraplate volcanic belts (Thordarson & Hoskuldsson, 2002) (Fig. 1). The combination of the spreading ridge and the Icelandic mantle plume results in Iceland's unique character of volcanic activity (Óladóttir, 2012).

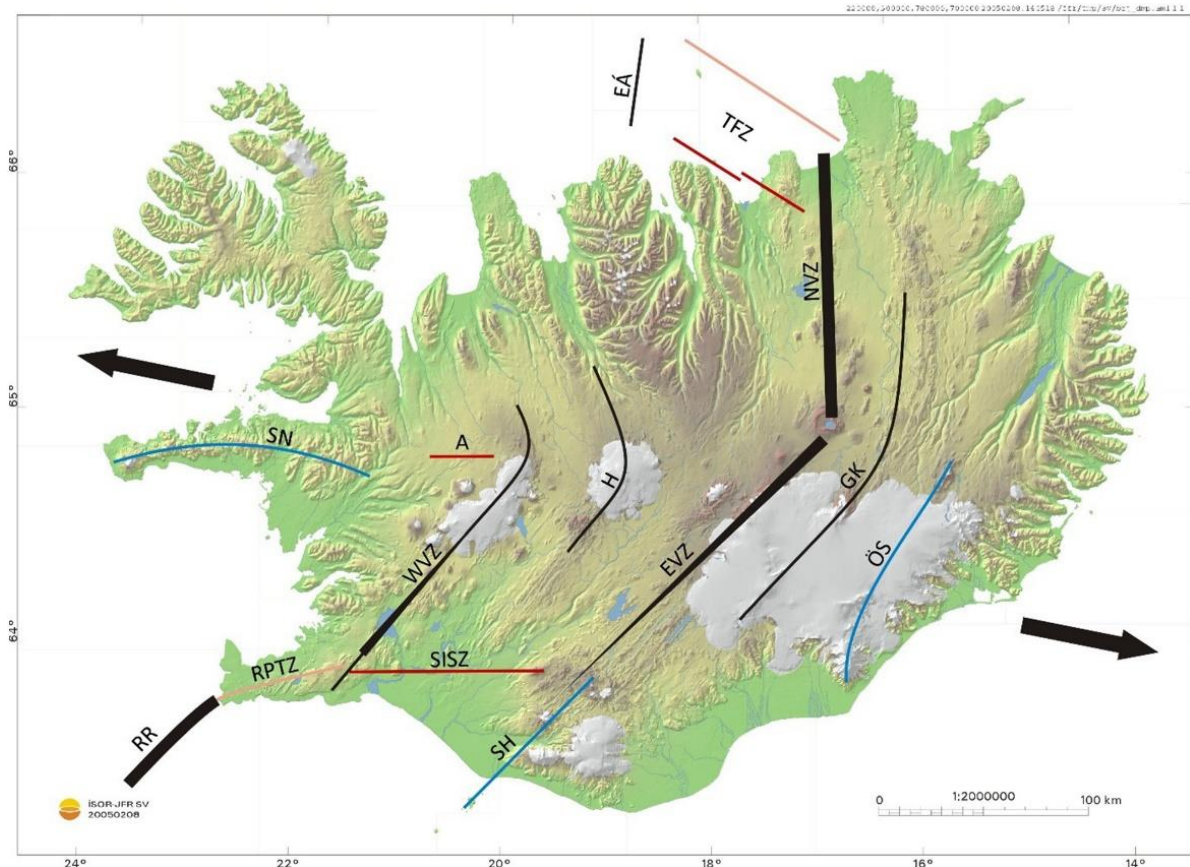


Figure 1: a schematic overview of main tectonic elements of Iceland: the volcanic spreading zones (black), the non-volcanic fracture zones (red), the volcanic trans-tensional rift zones (pink), the volcanic flank zones of transitional rock composition (blue), spreading direction (arrows), Eyjafjörður Deep (EÁ), Tjörnes Fracture Zone (TFZ), South Iceland seismic zone (SISZ), Arnarvatn fault zone (A), Northern (NVZ), Eastern (EVZ) and Western (WVZ) Volcanic Zones, Hofsjökull volcanic system (H), South Iceland flank zone (SH), Grímsvötn–Kverkfjöll volcanic systems (GK), Reykjanes Ridge (RR), Örfæjökull–Snæfellflank zone (ÖS), Reykjanes Peninsula trans-tensional zone (RPTZ) (Sæmundsson et al., 2020)

In the southwest tip of Iceland, the Reykjanes peninsula is located (Fig. 2). This tectonically active area consists of young, highly faulted, and porous basaltic formations. Due to the high permeability of the rocks, rainwater can easily infiltrate the ground (Marks et al., 2010). Four volcanic systems (Reykjanes, Krisuvik, Brennisteinsfjöll, and Hengill) can be observed in the Reykjanes peninsula (Clifton & Schlische, 2003). These systems have a northeast strike and extend across the peninsula. The most western-located volcanic system in the Reykjanes peninsula is the Reykjanes volcanic system (Thordarson & Hoskuldsson, 2002).

The landscape of the Reykjanes volcanic system is characterized by recent, low-relief lava flows, volcanic crater rows, a few Pleistocene hyaloclastite ridges protruding younger Holocene lavas, and the lack of central volcanoes with shallow secondary magma chambers (Fridriksson et al., 2016; Marks et al., 2010). Oblique extensional tectonics and episodic fissure eruption volcanism have been observed in this area (Fridriksson et al., 2016). Dikes intruded at depth provide heat to the geothermal system located in the Reykjanes volcanic system (Marks et al., 2010).

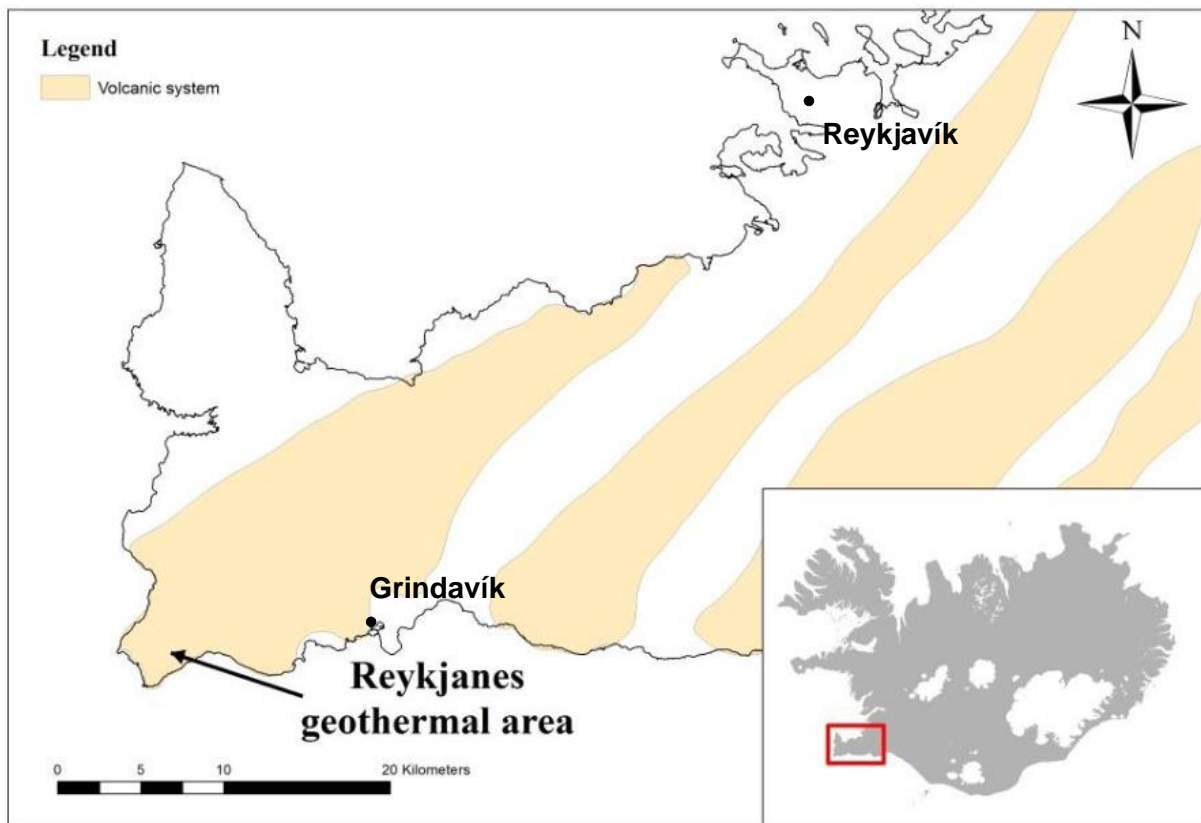


Figure 2: situation of the Reykjanes volcanic system, the Reykjanes geothermal area, Grindavík, and Reykjavík on a map of the Reykjanes peninsula (modified from Óladóttir, 2012)

The Reykjanes geothermal area is located southwest of the Reykjanes volcanic system and is a seawater-recharged hydrothermal system. The geothermal activity is controlled by complex local tectonics and ongoing volcanic activity (Marks et al., 2010). Tectonic and magmatic activity results in the circulation of groundwater and seawater through the basaltic crust. Frequently small earthquakes result in the movement of fractures and the maintenance of good permeability (Sigurdsson, 2010). The Reykjanes thermal area is situated at the centre of swarms of active faults which results in hydrologic

convection. The groundwater nearly flows to the surface due to the high heat of the thermal area (Marks et al., 2010).

According to Marks et al. (2010), the hydrothermal fluids of the Reykjanes geothermal area consist of chemically modified seawater through interaction with the basaltic host rocks. The total chloride content is nearly equal to seawater concentrations. Investigations of other major chemical elements (e.g. Ca, Na, Al, K) of the hydrothermal fluids of Reykjanes conclude that these fluids underwent substantial chemical modification through boiling, water-rock interaction, and perhaps evaporation. The ratio of meteoric water to seawater varies through time as a function of changing pressure, temperature, and permeability investigated by the deuterium isotopic concentration which is considerably lower than that of seawater. The hydrothermal fluids of Reykjanes geothermal area show geochemical affinities with hydrothermal fluids of the mid-ocean ridge. In Reykjanes geothermal area, the pH of the hydrothermal fluid is at a temperature of 267 °C calculated as 5.3 (Marks et al., 2010).

The uppermost 1000 m of the Reykjanes geothermal area is made up of hyaloclastite tuffs, breccias, tuffaceous and marine sediments. The uppermost 312 m of the Reykjanes geothermal area, the smectite-zeolite zone consists of the lowest grade alteration zone with abundant secondary calcite and quartz (Marks et al., 2010). Holocene lavas extend down to about 150 m in the Reykjanes field. A cold groundwater system and the outflow of geothermal fluids are present in the highly permeable Holocene lavas and in the uppermost part of the hyaloclastites (down to about 500 m). In part of the Gunnuhver area, south of the Grey Lagoon, ascent hot fluids towards the surface (Fridriksson et al., 2016). Heat flow from the system is 130 ± 16 MW (Fridriksson et al., 2006) and the lateral extent of the 280 °C isotherm at 1 km depth is about 1 km² (Marks et al., 2010). Quartz, calcite, zeolites, sulphides, and clay minerals are secondary minerals occurring in the Reykjanes geothermal area and are formed by geothermal alteration (Sternbergh, 2016).

A thin lens of fresh water (< 30 m thick) overlies the seawater outside the Reykjanes geothermal area (Marks et al., 2010; Sigurðsson et al., 1995). However, in the central part of the geothermal field, a freshwater lens does not exist because of the up-flow of hot brine and steam (Sigurdsson, 2010). The groundwater flow velocity, the thickness of the groundwater body, and the areal extent of the steam and groundwater interaction zone are still uncertain (Fridriksson et al., 2006).

The Gunnuhver geothermal area is part of the Reykjanes geothermal area and consists of Holocene lavas and tuff formations at the surface (Fig. 3). Extensive normal faulting and high-temperature geothermal activity are observed in this area (Marks et al., 2010). The landscape of the Gunnuhver area is dominated by recent lava flows, volcanic crater rows, and a few Pleistocene hyaloclastite ridges between the younger Holocene lavas. Most of the lavas have an age between 10000 and 2000 years. The youngest volcanic formation occurring in the Gunnuhver area was formed during the so-called Reykjanes Fires, a major volcano-tectonic episode in the Reykjanes system between 1210 and 1240. The geothermal system in this area is recharged by seawater due to the high permeability of the bedrock, the proximity of the ocean, and the low topographic relief (Óladóttir, 2012). Surface manifestations of the geothermal system in the Gunnuhver area are steam-heated mud pools, steam (H₂O and other gases) vents, fractures, and warm ground (Fridriksson et al., 2006).

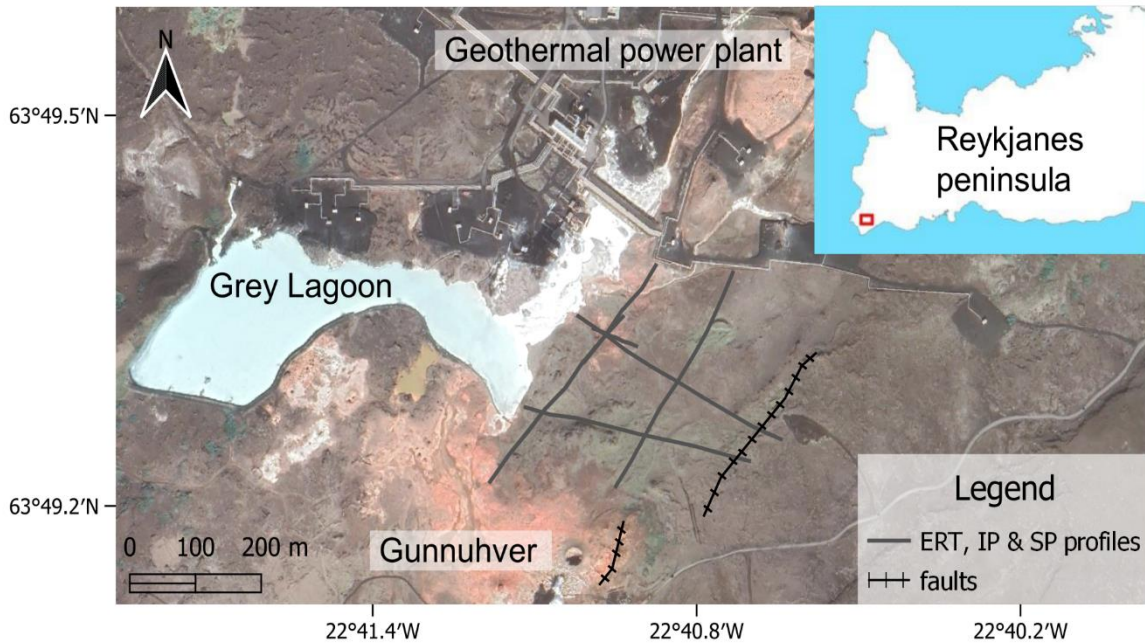


Figure 3: the location of the ERT, IP, and SP surveys in the Gunnuhver area

The most active parts of the Gunnuhver area are characterized by steam vent activity and steam-heated mud pools. In the other areas of the Gunnuhver site, the ground is warm in large patches. Regions of intensive geothermal activity are unvegetated areas and red soils of geothermally altered clay (Fig. 3). Characteristic vegetation of green moss (*Hypnum jutlandicum*) and creeping thyme (*Thymus praecox arcticus*) are observed in areas of less intense geothermal activity (Fridriksson et al., 2006).

The saline groundwater is observed about 0.5 m above sea level in natural conditions in the Gunnuhver area (Marteinsson et al., 2022). The direction of the shallow groundwater current was SW in natural conditions (Fridriksson et al., 2006). Evidence of boiling in the up-flow zone is the precipitation of calcite and the chloride concentration of the brine feeding the surface manifestations (Sigurdsson, 2010).

Iceland's climate is much milder than its name and location, next to the Arctic Circle, implies. The Gulf Stream partly flows along the southern and western coasts. This mild Atlantic air moderates the climate. However, it also comes in contact with the colder Arctic air. This leads to frequent changes in weather, storminess, and more rainfall in the southern part than in the northern part of Iceland (Einarsson, 1984).

One of the geothermal power plants of HS Orka is located next to the study area (Fig. 3). This power plant is since 2006 in full production. Before 2006, the geothermal surface activity was mainly concentrated south of the Grey Lagoon. Since the power plant starts working, the hot ground activity has expanded significantly (Fridriksson et al., 2016). The geothermal power plant is a high enthalpy geothermal system extracting geothermal fluid at km's depth. This fluid has seawater salinity and originates from the seawater source underneath the Reykjanes peninsula (Sigurdsson, 2010). The heat loss from areas of steaming ground can change due to variations in the production of the geothermal power plant (Óladóttir, 2012).

2.2 Volcanic hydrothermal systems

The dynamics of VHS are affected by several processes, which can be divided into two types: bottom-up and top-down processes (e.g. Peacock & Siler, 2021). In bottom-up processes, the discharge of mass and energy originating from the magma has a great influence on the water saturation and temperature of the shallow VHS. This can sometimes lead to an eruption.

The top-down processes occur at the surface without magmatic contribution. These processes can affect the underlying VHS, which can also possibly lead to an eruption. Seals can develop above vents through mineral precipitations. Volatiles can accumulate underneath the seals because of the clogging in the pore space in small-scale rock heterogeneities due to the mineral precipitations. Evidence for sealing processes has been found in the products of erupting volcanoes (Christenson et al., 2010). In acidic systems, sulphur-related minerals tend to seal, while in more neutral systems calcite or clays can lead to critical overpressure (Pardo et al., 2014).

The exact dynamics of the VHS are poorly known and difficult to study. Both bottom-up and top-down processes are used to explain the same eruption (Yamaoka et al., 2016). Sometimes clear physicochemical changes (volcanic tremors) precede VHS eruptions of steam and mud. These changes are however generally short-term precursors from minutes to hours (Kawakatsu et al., 2000).

Monitoring continuously the dynamic processes associated with VHS is mostly carried out using seismometers. However, according to Caudron et al. (2019), the high level of background seismic noise complicates the application of standard processing techniques. Other geophysical techniques such as gravimetry and muons monitoring have been applied to different volcanoes (Battaglia et al., 2016). These expensive methods require specific acquisition settings and characterize the system at a relatively low resolution (10^2 m to 10^3 m scale).

2.3 Electrical resistivity tomography in VHS

High-resolution spatial imaging (10 m scale) of the electrical properties of the subsurface can be obtained using ERT and IP. Electrical resistivity (ER) and its inverse electrical conductivity (EC) can be investigated using ERT. The chargeability can be studied using IP. Dynamical processes such as water content or temperature changes (Hermans et al., 2014; Uhlemann et al., 2017) are commonly monitored using ERT and IP (Singha et al., 2015). The electrical resistivity characterizes how easily an electrical current can flow through a medium in the subsurface and is sensitive to various parameters including porosity (total porosity, connectivity of the pore space, fractures), saturation, EC of the pore fluid and its temperature, presence of clay (surface conductivity) and (semi-)conductive minerals. The chargeability is the ability of the subsurface to store electrical charge and is linked to the presence of (semi-)conductive minerals, clay, and the structure of the pore space (Revil, Coperey, et al., 2017; Revil et al., 2015; Revil, Le Breton, et al., 2017). ERT has proven its effectiveness in measuring the physical properties of rocks in volcanic environments such as mineral alteration, rock permeability, temperature spatial distributions, and fluid saturation conditions (Ciraula et al., 2023b).

Temperature changes, saturation variation, and mineral precipitation are the main dynamical processes in VHS and influence its electrical properties (table 1). The major difficulty with VHS is that the main dynamic processes are often coupled (e.g. a simultaneous increase in temperature, decrease

in water saturation, and mineral precipitation). As a result, the prediction of the absolute change in electrical properties is complicated. The electrical conductivity of the fluid also influences the measured electrical signal.

Table 1: the main dynamical processes of VHS affecting the electrical conductivity and chargeability

Process	Influence of VHS	Relation with EC and chargeability
Temperature changes	Increasing temperature due to heat input from magma, and likely accompanied by the gas release or phase change	0-50 °C: linear change of 2 % °C ⁻¹ of EC (Hermans et al., 2014) > 50 °C: exponential increase of EC (Hayley et al., 2007)
Saturation variation	Decrease in liquid saturation due to increase in mineral precipitation or gas flux; increase in liquid saturation due to water infiltration	EC is approximately proportional to the square of the liquid saturation (Ramirez et al., 1993)
Mineral precipitation	Increase in chargeability and changing EC due to different mineral precipitation processes	Chargeability increase due to sulphides and clays precipitation and alteration (Benoit et al., 2019) EC increases due to dissolution processes (in saturated conditions) (Singha et al., 2015) EC decreases due to mineral precipitation (except conductive minerals or clays) in saturated pores (Wu et al., 2010)

The characterization of volcanoes using ERT (e.g. their structures, associated hydrothermal system, and presence of hot conductive fluids) is relatively common (e.g. Rosas-Carbajal et al., 2016; Soueid Ahmed et al., 2018; Troiano et al., 2019). However, in static surveys, the unambiguous interpretation of resistivity anomalies can be very difficult. Low resistivity measurements can either be related to the presence of highly weathered zones (clay/fractures) and/or the presence of high salinity/temperature fluids. Other geophysical techniques are needed to interpret the low-resistivity anomalies (e.g. Lévy et al., 2019). The geophysical method IP can reveal the presence of various mineral types in geothermal systems (e.g. Lévy et al., 2019; Revil et al., 2019). The quality of the IP data is among others influenced by the abundance of smectite. This clay has a naturally-high conductivity which is enhanced by high temperatures (Lévy et al., 2019).

Common secondary minerals in magmatic-hydrothermal systems are iron-sulphides (e.g. pyrite) and expandable clays (e.g. smectite) (Lévy et al., 2019). The sustained hydrothermal activity is represented by the abundant presence of these secondary minerals. The location of hydrothermal circulations can be mapped by the underground smectite and pyrite distribution. The salinity, the temperature of the fluids, and the presence of minerals with significant surface conduction, such as smectite influence the ERT measurements. The presence of sulphides and iron-oxides, conductive fluids, and clay minerals influence the measured IP signal (Lévy et al., 2019).

The dynamics of some VHS have been investigated using time-lapse or monitoring studies, where the same set of ERT measurements is repeated at various hourly and monthly intervals (e.g. Ciraula et al., 2023b; Di Giuseppe & Troiano, 2019; Turner et al., 2011), using electrode spacing varying from 2 to 5 m but only for a limited duration. The interpretation of the dynamical components of the system can be eased when considering some subsurface characteristics as constant (e.g. inactive part of VHS) (Linde et al., 2015). Laboratory and direct measurements remain necessary to calibrate and constrain ERT/IP data to local conditions or to differentiate between hypotheses (Hermans et al., 2014).

Long-term monitoring of dynamic natural systems such as saltwater intrusions (Nguyen et al., 2009), landslides (Uhlemann et al., 2017), soil moisture dynamics (Chambers et al., 2014), and permafrost (Mollaret et al., 2019) has been carried out using autonomous ERT/IP systems in remote locations automatically collecting/sending the ER and chargeability data of the subsurface at defined intervals. Geyser dynamics has been recently investigated using time-lapse ERT, transient electromagnetics, and other geophysical methods to image subsurface geyser structures and hydrothermal reservoir structures in a volcanic hydrothermal system (Ciraula et al., 2023b, 2023a). Pyrite mineralization has also been investigated using ERT and time-domain induced polarization at the Krafla caldera in the northeast of Iceland. In volcanic geothermal areas, H₂S can originate from the natural up-flow of magmatic fluids. The interaction of H₂S and basaltic rocks or the artificial re-injection of H₂S concerning geothermal exploitation can cause the mineralization of pyrite (Lévy et al., 2019).

Time-lapse ERT/IP at daily intervals for more than six months with an autonomous system has until the ERupT research project never been applied in a volcanic hydrothermal system to try to understand the dynamics of this complex system.

2.4 Self-potential in VHS

Complementary information to ERT and IP can be obtained using self-potential (SP). This geophysical method is influenced by fluid flow and diffusion/conduction processes and can provide valuable insights into local hydrogeology, preferential flow paths, fluid flow dynamics, macroscale structural features of volcanic systems, and on a variety of spatial and temporal scales when combined with other sources of prior information and/or data types (Finizola et al., 2002; Grobbe et al., 2021; Grobbe & Barde-Cabusson, 2019; Jardani et al., 2007).

Determining the source of the measured SP signals uniquely is challenging, especially when SP data is the only data collected (Grobbe & Barde-Cabusson, 2019). Contributions of shallow and deep SP sources can interfere with each other resulting in shallow source contribution acting as a parasitic signal on deep hydrothermal activities and structures, leading possibly to misinterpretations (Grobbe & Barde-Cabusson, 2019). The macroscale features and flow behaviour are interpreted as the primary contributors to the SP signals (Grobbe & Barde-Cabusson, 2019). SP anomalies can also be related to geothermal systems where strong thermal gradients exist in the subsurface (Zlotnicki & Nishida, 2003). The geothermal energy is then released through groundwater circulation, hot gas emission, and thermal conduction (Zlotnicki & Nishida, 2003).

In hydrothermal systems, the three main contributors to the electrical field measured with SP are the electrokinetic or streaming potential, the thermoelectric effect, and the electrochemical effect. The streaming potential is the major contributor to self-potential signals in VHS and is associated with

groundwater flow. The two other contributors to the SP signal are respectively related to a gradient in temperature and associated with a gradient in the chemical potential of charge carriers in isothermal conditions. These two contributors to the SP signal can however be safely neglected in VHS in the opinion of Revil et al. (2023). Due to streaming potential related to shallow water flow in the hydrothermal system, high amplitude SP anomalies are usually generated by hydrothermal systems in volcanic environments (Revil et al., 2023; Tarchini et al., 2019).

Positive SP anomalies can coincide with electrically conductive zones, can be associated with smaller structures and smaller hydrothermal systems, can result from the streaming current associated with the flow of pore water, and/or can result from up-flow of hydrothermal fluids (Grobbe & Barde-Cabusson, 2019; Revil et al., 2004, 2008; Tarchini et al., 2019).

Negative SP anomalies can be associated with the downward flow (e.g. drainage network) and infiltration/ percolation of cooling groundwater at relatively shallow levels (Grobbe & Barde-Cabusson, 2019; Revil et al., 2004, 2008), can result from the streaming potential from the circulation of meteoric water (Tarchini et al., 2019), can be generated by chemical reactions between volcanic gases (H_2S , SO_2 , CO_2) and groundwater (Zlotnicki & Nishida, 2003), can result from a decrease in temperature during cooling of lava flows, decrease in shallow hydrothermal activity and/or decrease in thermoelectric contributions (Grobbe & Barde-Cabusson, 2019).

Fluid-flow processes in some volcanic environments have already been studied using the self-potential method (Grobbe & Barde-Cabusson, 2019). The deep hydrothermal systems of La Fossa Di volcano (Italy) (Revil et al., 2008), Piton De La Fournaise (France) (Barde-Cabusson et al., 2009), and Teide (Spain) (Villasante-Marcos et al., 2014) are investigated by SP acquisitions along 2 to 10 km profiles with 20 m electrode spacing. Shallow hydrothermal systems are investigated in Piton De La Fournaise (France) (Barde-Cabusson et al., 2009) and Stromboli (Italy) (Finizola et al., 2002) with SP profiles of 4 to 10 km with an electrode spacing of 20 to 50 m. In Teide (Spain) (Villasante-Marcos et al., 2014) and Garrotxa (Spain) (Barde-Cabusson et al., 2014), the groundwater is investigated using SP along 1.6 to 10 km profiles with 20 m electrode spacing. While for this project, small-scale and higher resolution self-potential surveys (5 m spacing) in a volcanic environment were carried out.

3 Material and methods

3.1 Electrical resistivity tomography

The electrical resistivity ρ (in $\Omega\cdot\text{m}$) is a material's property characterizing how easily electrical current can flow through it and varies with temperature. The electrical conductivity σ (in S/m) is the inverse of the electrical resistivity. Currents flow more easily through materials with low resistivity and high conductivity. The resistivity of the subsurface cannot directly be measured. The resistance R however can be measured according to Ohm's law. Ohm's law formulates that the difference of potential ΔV (in V) is equal to the multiplication of the current intensity I (in A) and the electrical resistance R (in Ω) of the material sample. The resistivity ρ and resistance R are linked through Pouillet's law:

$$R = \frac{\rho L}{S} \quad (1)$$

where L is the length of the sample and S is the section of the sample. The resistance depends on the geometry of the volume through which the current flows (Reynolds, 2011).

No unambiguous identification of rocks from resistivity values is possible, because of the great variability in resistivity values of geological materials (e.g. resistivity of clay 1-100 $\Omega\cdot\text{m}$ and basalt > 50 $\Omega\cdot\text{m}$) (Lowrie, 2007). Mainly three electrical conduction mechanisms are responsible for this variability: metallic conduction, electrolytic conduction, and surface conduction. Metallic or electronic conduction is the movement of electrons within the grains of (semi-)conducting minerals. Electrolytic conduction is the movement of ions in the water within the pore space. Pore fluids with a higher salinity are therefore more conductive. Surface conduction is described as the preferential flow paths for ions in the electrical double layer at the solid-fluid interface and depends mostly on the clay content. If the pore fluid is conductive, for example, consists of salt water, the surface conductivity of clay minerals is proportionally less important than electrolytic conductivity (Revil et al., 2012; Reynolds, 2011).

Archie's law can be used to determine the bulk resistivity of clay-free sediments. This law describes the link between the bulk resistivity ρ_b , porosity ϕ , saturation S and resistivity of the pore fluid ρ_w :

$$\rho_b = \frac{a}{\phi^m} \frac{1}{S^n} \rho_w \quad (2)$$

Where m is the cementation exponent, a is an empirical factor close to 1 and n is the saturation exponent, typically close to 2 (Archie, 1942). An additional term needs to be considered to account for the surface resistivity ρ_{surf} at low salinity and high clay content (Waxman & Smits, 1968):

$$\rho_b = \frac{a}{\phi^m} \frac{1}{S^n} \rho_w + \rho_{surf} \quad (3)$$

Resistivity methods are used for hydrogeology and assessment of geohazards e.g. image sinkholes (Jardani et al., 2007), cavities (Smith, 1986), landslides (Lapenna et al., 2005), geotechnical applications (Ha et al., 2010), contamination problems (Naudet et al., 2004), salt water intrusions (Hermans et al., 2012a), moisture content (Binley et al., 2002) and biodegradation of hydrocarbons (Atekwana et al., 2000). Resistivity methods are hence used in a wide range of applications to study multiple subsurface properties. Additional information is however needed to interpret the resistivity results quantitatively.

3.1.1 Principle of ERT

Electrical resistivity tomography (ERT) is an active geophysical method mapping the bulk electrical resistivity distribution in the subsurface. An electrical current is injected into the soil between two electrodes (current electrodes) (Hermans et al., 2014). The resulting electrical potential difference is measured simultaneously between two other electrodes (potential electrodes). The distribution of the potential due to an injected current can be solved with Poisson's equation, a combination of the Ampere-Maxwell equation and Ohm's law:

$$\nabla \vec{J}_s = \nabla(\sigma \nabla \phi) \quad (4)$$

where \vec{J}_s (in A/m²) is the current density from the source, σ is the electrical conductivity and ϕ (in V) is the electrical potential (Telford et al., 1990).

For a homogeneous subsurface, an analytical solution can be used to obtain the potential difference:

$$\Delta \phi = \frac{\rho I}{2\pi} \left(\frac{1}{|r_A - r_M|} - \frac{1}{|r_A - r_N|} - \frac{1}{|r_B - r_M|} + \frac{1}{|r_B - r_N|} \right) = \frac{\rho I}{K} \quad (5)$$

where ρ is the electrical resistivity, I is the injected current, r is the position of the respective electrodes, A and B are the current electrodes, N and M are the potential electrodes and K (in m) is the geometrical factor. The geometrical factor depends only on the geometry of the electrode array. However, the subsurface is heterogenous in field cases. The resistivity is not constant in these cases and the apparent resistivity is measured instead of the true resistivity. Equation 5 can not be solved analytically in heterogeneous media. Numerical methods are used to obtain a numerical solution for heterogeneous media (Reynolds, 2011; Telford et al., 1990).

3.1.2 Measuring principle

The value of the apparent resistivity depends on the geometry of the used electrode array, which is defined by the geometric factor K . Different electrode arrays are: the Wenner array, the Schlumberger array, the gradient array, the dipole-dipole array, and the pole-dipole array. All the different types of electrode arrays have particular advantages, disadvantages and sensitivities (Reynolds, 2011).

Multichannel data-acquisition systems record multiple data points simultaneously for each current injection. With these systems, the acquisition time is significantly reduced without compromising the data density. Multiple gradient, pole-dipole and dipole-dipole arrays are well-suited methods when using a multichannel acquisition system. (Dahlin & Zhou, 2004).

The multiple gradient array is expected to combine

the characteristics of pole-dipole, Wenner and Schlumberger arrays with a good signal-to-noise ratio and a high resolution. The multiple gradient is the electrode array used in this project. A current is injected with a current-electrode separation of $(s + 2)a$ (Fig. 4). At all the potential electrodes pairs with spacing a , the potential difference is simultaneously measured.

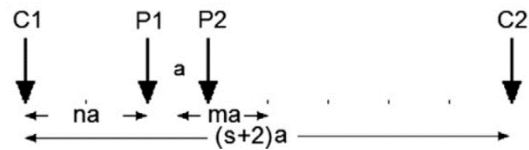


Figure 4: schematic visualization of the multiple gradient array with the total array length $(s + 2)a$, and the distance between the centre of the potential dipole pair P1-P2 and current pair C1-C2 ma (modified from Loke et al., 2013)

The n -factor defines the smallest relative spacing between current and potential electrodes. The separation factor s gives the highest amount of potential readings for a current injection (Dahlin & Zhou, 2006). The geometric factor K for the multiple gradient array can be written as (Loke et al., 2013)

$$K = 2\pi \left(\frac{1}{na} - \frac{1}{(n+1)a} - \frac{1}{(s+2-n)a} + \frac{1}{(s+1-n)a} \right)^{-1} \quad (6)$$

The apparent resistivity is visualized in a pseudosection using 2D lines by measuring at different locations along a profile with systematically larger spacing. The visualization of the data using this pseudosection depends on the type of configuration used for the data collection. For the entire area counts that the data density in the upper layer of the subsurface is higher since more electrode combinations measure shallow points (Reynolds, 2011).

The sensitivity pattern of the gradient array depends on the position of the potential electrodes as observed in figure 5. If there is a positive change in resistivity, the positive potential difference will be measured in the (+) field as deduced from the sensitivity function. This electrode array focuses on lateral sensitivity, meaning the vertical features are defined with relatively sharp vertical sensitivity (e.g. horizontal layers) (Dahlin & Zhou, 2006).

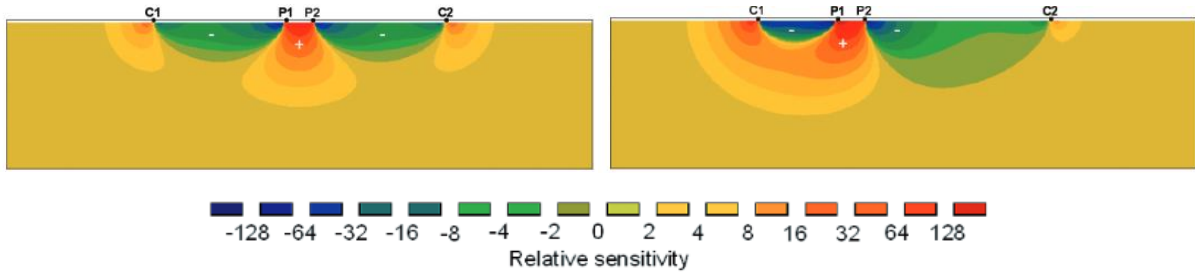


Figure 5: vertical section through sensitivity function along electrode layout for gradient array with different separation factors and n -factors (modified from Dahlin & Zhou, 2006)

3.1.3 Noise considerations

Misinterpretation of ERT images can be prevented with accurate quantification of measurement errors or noise (LaBrecque et al., 1996). The resolution of the electrical structure is limited by the measurement noise. Noise overestimation (gross smoothing of structure) and underestimation (artificial image structure) can result from incorrect noise estimation. Noise can be created by factors such as poor electrode contact, random errors, and sporadic errors (background noise) (LaBrecque et al., 1996). Repeatability tests or stacking is a method of noise quantification. An alternative method, the reciprocal error is defined as

$$e = R_n - R_r \quad (7)$$

where R_n is the 'normal' resistance measurement, R_r is the 'reciprocal' resistance measurement, and e is the measure of data noise. According to the principle of reciprocity, exchanging current electrodes with potential electrodes should not affect the measured resistivity (Parasnis, 1988; Slater et al., 2000). This method can detect errors that may not be apparent from repeatability checks because another injection electrode pair is used.

A linear error model can be used in which the magnitude of reciprocal error $|e|$ increases with the magnitude of measured resistance $|R|$:

$$|e| = a + b|R| \quad (8)$$

Parameters a and b are defined as respectively the minimum error and the increase in $|e|$ with $|R|$. Plots can be made of the reciprocal error against resistance for the background dataset. First, the obvious outliers, typically $|e| > 10\%$ of $|R|$, can be removed. Then the parameters of the error model can be defined by an envelope that encompasses all remaining measurements (Slater et al., 2000).

An overestimation of the error for all data points is accompanied by the conservative envelope method. This limits the artefacts of the inversion due to noise but might introduce an over-smoothed image. As an alternative, a less conservative method, the linear trend can be used. In this approach, the envelope curve is replaced by a linear regression error model based on a least-square fit (e.g. Van Riet et al., 2022).

An individual error can also be used to investigate the noise and obtain a less conservative inversion model. For each measurement point, the reciprocal error is calculated and used during the inversion (e.g. Hermans et al., 2012b).

3.1.4 Inversion principle

The forward problem, the estimation of the data d corresponding to a specific model m can be formulated as

$$d = f(m) \quad (9)$$

where f is the forward operator of the problem, i.e. the resolution of Poisson's equation (Eq. 4) for the set of quadrupoles of measurements. However, ERT aims to find a model m explaining the observed data d , an inverse problem. Different models can explain the observed data because there are more variables to be estimated than there is available data. The solution is thus non-unique. A regularization approach is generally used to minimize the data misfit with some prior assumptions of the model and to find a unique solution. The inversion process is carried out by an iterative minimization of the objective function:

$$\psi(m) = \psi_d(m) + \lambda\psi_m(m) \quad (10)$$

where m is the (unknown) model vector, $\psi_d(m)$ is the data misfit, $\psi_m(m)$ is the model functional with some assumed characteristic of the model and λ is the regularization parameter. The regularization parameter balances the two terms and is optimized at each iteration to minimize the data misfit in CRTomo (Thibaut et al., 2021). The iterative minimization of the objective function concerning the model vector m is a non-linear problem (Hermans et al., 2014). The second term on the right-hand side of equation 9 stabilizes the inversion process because inverting only with a data misfit criterion would lead to implausible and noisy results (Tikhonov et al., 1995).

The data and model misfit can be calculated based on an infinite number of norms. The two most used norms are the L_1 and L_2 norms. The L_2 norm is the least-square or smooth solution and assumes a Gaussian distribution of the errors. The L_1 norm or robust solution assumes a Laplace distribution of the errors. In this study, the data misfit (Eq. 11) and model misfit (Eq. 12) are both calculated with the L_2 norm. According to Kemna (2000), this can be formulated as

$$\psi_d = \left\| \frac{d - f(m)}{\epsilon} \right\|^2 = \sum_{i=1}^N \left(\frac{d_i - f_i(m)}{\epsilon_i} \right)^2 = \|W_d(d - f(m))\|^2 \quad (11)$$

$$\psi_m(m) = \iint \|\nabla m\|^2 dx dz \cong \|W_m(m)\|^2 \quad (12)$$

where ϵ_i is the standard deviation at data point i , derived from the error model (section 3.1.3), W_d is the data weighting matrix which is a diagonal matrix with $1/\epsilon_i$ as elements, W_m is the matrix evaluating the roughness of m and thus resulting in a smooth model. Alternative regularizations have been developed because the smoothing constraint often results in models that are not consistent with the expected (hydro)geological processes (e.g. Hermans et al., 2012). Iterations, until the misfit reaches a predefined level, are carried out to minimize the objective function of equation 10 (Hermans, 2014). Here, the misfit level is estimated from the noise estimations (Kemna, 2000), thus the data is fitted within its noise level.

The objective function expressed in terms of the defined operations is a substitution of equations 11 and 12 in equation 10 (Kemna, 2000).

$$\psi(m) = \|W_d(d - f(m))\|^2 + \lambda \|W_m(m)\|^2 \quad (13)$$

This function is solved iteratively. At each iteration, the regularization factor is optimized through a line search to minimize the weighted root mean square error. If the weighted root mean square error reaches one, a predefined number of iterations (20) is reached or no improvement of the weighted root mean square error between consecutive iterations is realized, the inversion stops (Thibaut et al., 2021). CRTomo is used to carry out the ERT inversions based on an iterative Gauss-Newton scheme to solve the inverse problem and a finite element approach to solve the forward model (Kemna, 2000).

3.1.5 Inversion principle with a reference model

The addition of prior information can reduce the number of mathematical solutions (Oldenburg & Li, 1999). This is very convenient given the non-unique character of the inversion principle. The prior information can be added as a reference model including relevant information collected apart from the ERT measurements at the study site.

The reference model m_{ref} is implemented in the objective function of the inversion:

$$\psi(m) = \|W_d(d - f(m))\|^2 + \lambda (\|W_m(m - m_{ref})\|^2 + \alpha \|m - m_{ref}\|^2) \quad (14)$$

where α is the closeness factor which weights the importance of the reference model during the inversion process (Dumont et al., 2016). The value of the closeness factor is chosen arbitrarily. A relatively low α will have a minor influence on the inversion result, whereas a relatively high α will result in an inverted model closer to m_{ref} . By using the closeness factor, some subjectivity is introduced in the inversion process (Hermans, 2014).

3.1.6 Time-lapse inversion principle

Time-lapse ERT is a powerful technique to explore the dynamic changes of subsurface properties using monitoring studies (Miller et al., 2008). Inverse time-lapse datasets can be inverted with different procedures: independent inversion, time-constrained inversion, and difference inversion (Miller et al., 2008). In this study, the time-constrained and difference inversion are used to invert the monitoring datasets. In the time-lapse time-constrained inversion, the background model m_0 is used as a reference model instead of the reference model m_{ref} and is the result of modifying equation 14:

$$\psi(m) = \|W_d(d - f(m))\|^2 + \lambda (\|W_m(m - m_0)\|^2 + \alpha \|m - m_0\|^2) \quad (15)$$

The variation of the data and model is formulated instead of the absolute values in the difference inversion (Kemna, 2000). Equation 13 is modified to result in the difference inversion (Kemna, 2000).

$$\psi(m) = \|W_d(d - d_0 + f(m_0) - f(m))\|^2 + \lambda \|W_m(m - m_0)\|^2 \quad (16)$$

The background or initial state is presented by d_0 and m_0 and their results are used as the basis for the following inversions. The inversion problem is solved iteratively like the absolute inversion. The systematic error assumed constant in subsequent data set, decreases because of the subtraction (LaBrecque & Yang, 2001).

Data error estimates are highly determining the image quality of time-lapse inversion (Lesparre et al., 2017). Methodologies to model the noise level using reciprocal data at each time step are proposed by Lesparre et al. (2017). The least-squares fit strategy to define the error model for each time step is carried out in this study (Lesparre et al., 2017).

3.1.7 ERT image appraisal tools

Caterina et al. (2013) compared different ERT image appraisal tools: model resolution matrix, cumulative sensitivity matrix, and depth of investigation index. These tools help to avoid over-interpretation of the inversion results due to the decrease of the sensitivity and resolution with depth. The cumulative sensitivity matrix and the depth of investigation index are used in this study.

The cumulative sensitivity matrix is used to make a quick assessment of image quality. The cumulative sensitivity can be defined as

$$S = \text{diag}\{J^T W_d^T W_d J\} \quad (17)$$

where J is the Jacobian matrix (Kemna, 2000). A rough estimation of how good the resistivity is represented by the data can be deduced from the sensitivity. High sensitivity means that changes in the parameter strongly influence the calculated data. Low sensitivity on the other hand means there is a small to non-existing influence. When prior information is used, low sensitivity does not directly mean that the model is not reliable (Hermans et al., 2014). The sensitivity is not depending on the resolution and is represented on a relative and logarithmic scale.

Another appraisal method used in this study is the depth of investigation index (DOI) proposed by Oldenburg & Li (1999) estimating the reliability (data dependence) of the calculated ERT model with depth. Two inversions of the same data set are carried out using different values of the reference resistivity (Marescot et al., 2003). The first reference resistivity value, q_A is generally calculated as 0.1 times the logarithm of the average measured apparent resistivity (Marescot et al., 2003). The second reference resistivity value, q_B is typically 100 times the first reference resistivity value (Deceuster et al., 2014). The DOI value for each model cell is given by

$$R_{AB}(x, z) = \left| \frac{q_A(x, z) - q_B(x, z)}{q_A - q_B} \right| \quad (18)$$

where $q_A(x, z)$ and $q_B(x, z)$ are the model cell resistivities obtained from respectively the first and second inversion (Deceuster et al., 2014). The absolute value of the DOI is used (Oldenburg & Li, 1999).

In parts of the model where two inversions generate the same resistivity values, the R value will approach zero (Marescot et al., 2003). The cell resistivity is well-constrained by the data in parts of the model with low values (Marescot et al., 2003). The R value will approach 1.0 in areas where the data do not contain much information about the cell resistivity and hence the model depends more on the

regularization procedure than on the actual data (Marescot et al., 2003). The cell resistivity will be similar to the reference resistivity in these areas (Marescot et al., 2003) and occurs at sufficiently great depths, near the ends of the survey line because of the sparser data coverage (Marescot et al., 2003). According to Oldenburg & Li (1999), DOI values of 0.1 or 0.2 are considered to delimit the reliable part of the inverted model. However, Caterina et al. (2013) proposed to use a gradient instead of a DOI value. The loss of reliability in the inverse model is considered when the DOI values start to significantly rise (Caterina et al., 2013).

3.1.8 ERT field measurements

During the field campaign between 29 August and 7 September 2022, ERT measurements were initially performed to characterize the study area. Multiple gradient ERT measurements were carried out along five profiles for the characterization. Profile 1, 2, 3, and 4 have a spacing of 5 m (Fig. 6). Profile 5 has a 1 m spacing to obtain higher resolution measurements. Profile 2, 3, 4, and 5 exist each of 72 electrodes. Profile 1 exists of 82 electrodes and was collected in two parts (profile 1a and 1b). Reciprocal ERT measurements were performed for profiles 2, 3, 4, and 5. Normal and reciprocal measurements were carried out right after each other to ensure resistivity distribution of the subsurface remained constant. ERT measurements of profiles 1a, 1b, 2, 3, 4, and 5 were carried out on respectively 30 August, 30 August, 31 August, 1 September, 2 September, and 3 September 2022. The normal ERT measurements lasted for 15 and 25 minutes and consisted of 1796 (profile 1b), 1803 (profile 2), and 1809 (profile 1a, 3, 4, and 5) data points. The reciprocal ERT measurements of the characterization profiles lasted 60 to 90 minutes per profile and consisted of 3249 measuring points.

For the ERT monitoring of the study area, one profile of 72 electrodes with a multiple gradient configuration and a spacing of 5 m was installed. Every day since 23 October 2022, 1 ERT measurement is carried out along the monitoring profile with both normal and reciprocal configurations. The location of the monitoring profile is similar to the location of profile 1a. The normal ERT measurement of the monitoring profile is around 8.30 AM. After the 30 minutes of normal ERT measurement, the reciprocal measurement takes place for about 60 minutes. The number of data points changes during the period 23/10/2022 – 27/02/2023 and has a minimum of 1611 and a maximum of 1624.

Electrodes are metal rods that are hammered in the soil. Connections from an electrical cable to the electrodes are made. These connections are taped for the monitoring profile to protect the electrodes, connectors, and cables from corrosion.

To measure the resistivity, a Syscal Pro. SWITCH 72 (IRIS INSTRUMENTS) is used. This device, together with 2 batteries (6FM100D-X), a Syscal Monitoring Unit (IRIS INSTRUMENTS), and a router were placed in a plastic box to protect the equipment from rain and snow (Fig. 7). The length of injection is about 1000 ms and the transmitted current is between 800 and 2500 mA for the normal ERT measurements. The used multiple gradient configuration has the parameters s as 2, 7, 9, and 12, and a as 1, 3, 4, 6, 9, and 11.

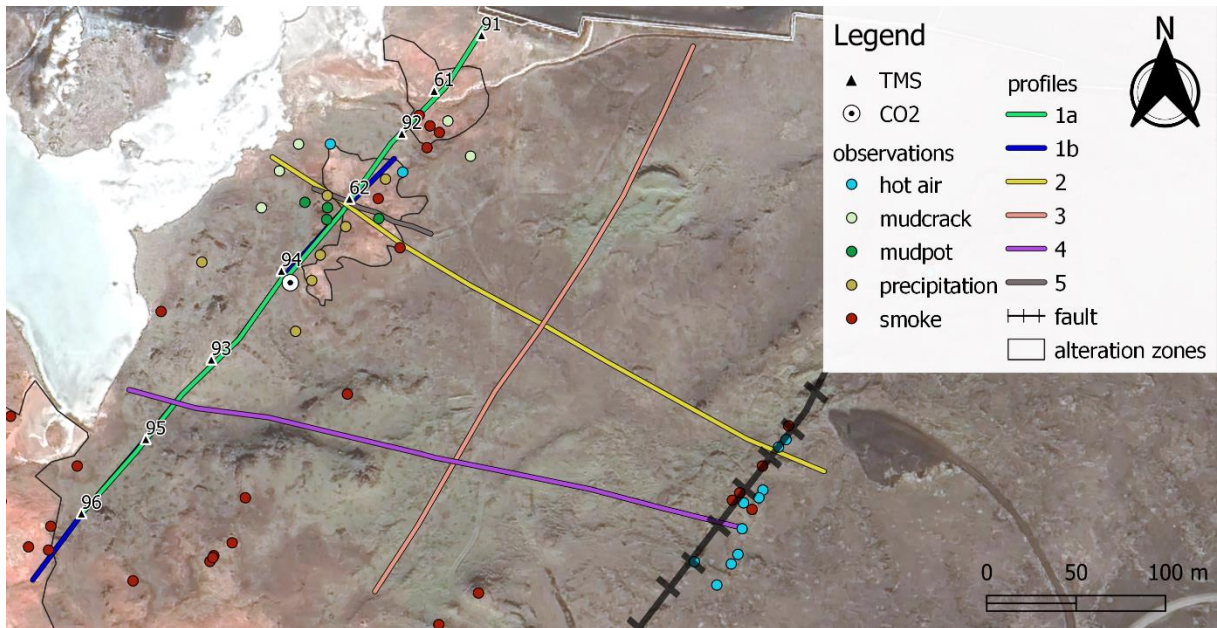


Figure 6: the locations of the ERT and SP profiles, the point observations, the location of the temperature and soil moisture sensors (TMS), and the location of the CO₂ measuring device in the Gunnuhver area



Figure 7: the box with ERT measuring equipment during the field campaign and the ERT electrode connected to the cable on the field; for the monitoring study, an extra battery and charger are present in the box

3.1.9 Pre-processing of ERT data

Firstly, the data quality is evaluated before the ERT data is inverted to ensure the profiles are viable for inversion. A first check is carried out using the variation coefficient. When the measurements start, the measured data points are stacked. The variation coefficient is equal to the standard deviation between the stackings, divided by the mean resistance of the data point. Repeatable measurements of the same data point are carried out until either the variation coefficient reaches a predetermined threshold (1 %) or the maximum number of stackings (3) is reached. The data points of low quality are filtered using the threshold. The absolute variation is obtained by multiplying with the resistance. Almost no problems with contact resistance were encountered during the ERT measurements.

All the negative resistance values are filtered out from the data files before inversion because these are physically implausible for positive geometrical factors.

First, five ERT measurements between 23/10/2022 and 22/02/2023 are selected based on the mean resistance and the coefficient of variation. These selected profiles are used to execute time-lapse

inversion because it is not manageable to test inversion parameters on all collected profiles during the monitoring. Only the ERT data acquired during the period of available temperature, humidity, CO₂, and precipitation data is used in this study.

For every ERT profile, a grid consisting of rectangular elements was created by Lore Vanhooren. The elevation of each ERT profile is implemented in its corresponding grid. Overall the cells get larger towards the edges. The electrodes used to carry out the ERT measurements are located on the first row of the grid. The thickness of the first row is 2.5 m and 0.5 m for profile 5. This is kept constant for 30 rows. Five cells extra in negative and positive x-direction and z-direction are implemented to minimize the boundary effects. Between subsequent electrodes, two cells are located. The mesh of profile 1 consists of 6228 nodes, 6020 cells, 172 columns, and 35 rows. The meshes of profile 1a, 1b, 2, 3, 4, and 5 consist each of 5508 nodes, 5320 cells, 152 columns, and 35 rows. The visualization of each mesh can be found in appendix A. The mesh of profile 5 is made without topography. Figure 8 is the visualization of mesh 1a shown with the position of the electrodes represented as red dots.

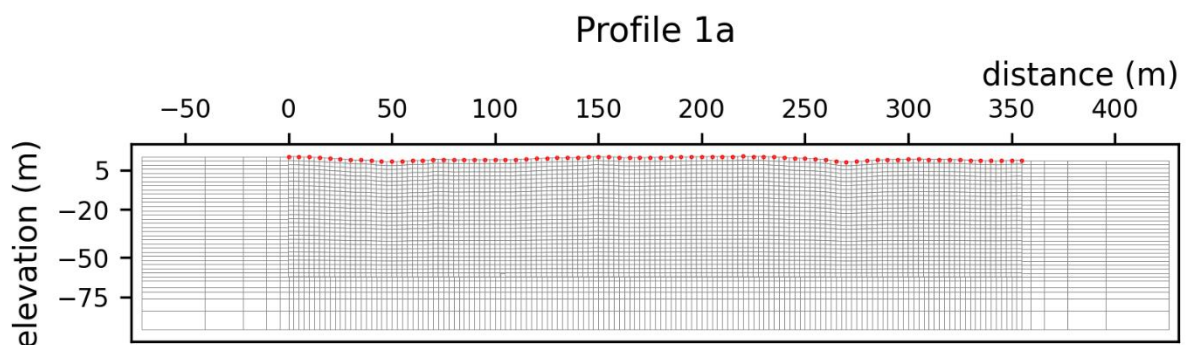


Figure 8: the grid of profile 1a with the location of the electrodes as red dots

Last, the maximum resistivity value of the visualized ERT profiles is set at 1000 $\Omega\cdot\text{m}$. This is not the maximum resistivity that can occur in the study area but a self-defined maximum. Note that the ERT profiles are only semi-quantitative interpretable based on relative variations. High resistivity values ($\rho > 300 \Omega\cdot\text{m}$) can correspond to unsaturated sediments or rocks while very low resistivity values ($\rho < 5 \Omega\cdot\text{m}$) can correspond to saltwater or zones with conductive minerals. In the intermediate range, more resistive zone typically correspond to lower salinity, lower temperatures, lower porosity, lower saturation, lower clay content, lower conductive material content, or a combination of several factors.

3.2 Self-potential method

The naturally occurring difference in electrical potential between two electrodes coupled to the Earth is measured with the self-potential or spontaneous potential method. No human-made source is needed to execute SP measurements which makes it a passive geophysical method. With this method, the measured natural variations of electrical potential (or electrical field) at the surface can be used to determine the causative current source in the ground and obtain information about groundwater flow, hydromechanical and geochemical disturbances in general (Revil & Jardani, 2013). More specifically, SP is used for, among others, detecting ore bodies, groundwater, and geothermal investigations, geological mapping, forecasting earthquakes and volcanic eruptions, and investigating volcanic plumbing and archaeological investigations (Revil et al., 2012; Reynolds, 2011).

Interpretations of the self-potential anomalies are only qualitative (Lowrie, 2007). The sign of the measured potential, positive or negative, is an important diagnostic factor in the interpretation of SP anomalies (Reynolds, 2011). The sources of the SP anomalies can be very diverse such as mineral deposits, topography, groundwater movement, vegetation, the geometry of geological structures, and combinations of different processes which complicates the interpretation of SP signals (Reynolds, 2011). Noise can originate from different transient sources such as telluric currents, spatial noise, and other artefacts associated with non-polarizing electrodes themselves (Revil et al., 2012).

This method offers very fast, low-cost, non-intrusive, and efficient data acquisition and is a highly mobile and light-weight technique, allowing for data acquisition of large areas and rough terrains (Arens et al., 2020; Grobde & Barde-Cabusson, 2019).

3.2.1 General acquisition

Nonpolarizable electrodes (e.g. Pb/PbCl₂, Cu/CuSO₄) are used to measure the relative electrical potential difference by connecting the electrodes to a voltmeter through an insulated electric cable. A high input impedance voltmeter (~ 10-100 MΩ) with a sensitivity of ± 0.1 mV is generally used. The non-polarizing electrodes are made of a metal (e.g. lead, copper) in contact with its salt (e.g. lead(II) chloride, copper sulfate solution) (Revil & Jardani, 2013).

Potential measurements are carried out at stations along a profile during the surveying procedure (e.g. gradient, field method) (Lowrie, 2007). Compared to the gradient method, the total field method (Fig. 9) results in a smaller cumulative error and is used in this study. Usually, the total field method provides data of better quality and allows more flexibility in placing the mobile electrode according to Reynolds (2011).

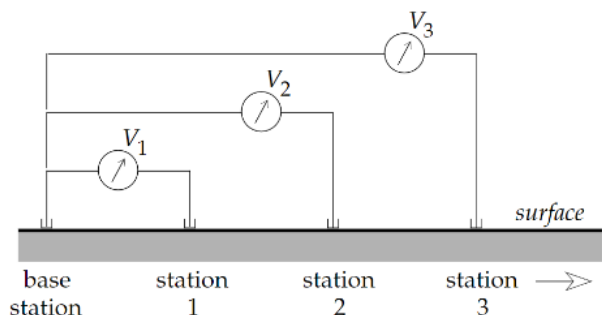


Figure 9: the field technique of measuring self-potential by the total field method (Lowrie, 2007)

The fixed electrode or reference electrode is placed at the beginning of the profile and is artificially chosen to be 0 mV. After a measurement, the second and moving electrode is relocated to the next position and again the potential difference between itself and the reference electrode is measured. At the end of the measured section, determined by the length of the wire, the moving electrode at its last position becomes the position of the new reference station for the next section until the end of the wire is reached again. An artificial value of 0 mV is also assigned to the new reference electrode at the start of the new section. For each section, the first pair of electrodes is remeasured when the section is completed to measure a possible shift in self-potential which can be corrected afterward. For each measurement point, a small hole (~ 5-10 cm deep) is dug and filled partly with saline bentonite mud (silt and smectite powder) to ensure good electrical contact between the electrode and the soil. Three repeated measurements at each station are carried out to systematically check the electrical potential stability.

Only relative trends that indicate the presence of subsurface anomalies can be used to interpret the data because all SP data points are relative measurements. According to Revil et al. (2008), the value of the self-potential itself is meaningless when interpreting self-potential data. Also, corrections need to

be carried out because several arbitrarily assigned 0 mV values for each new section are used to obtain the data (Fig. 10). The several SP sections need to be properly combined (reference correction) and corrected for drift occurring during the acquisition to re-establish the continuity of the electrical potential.

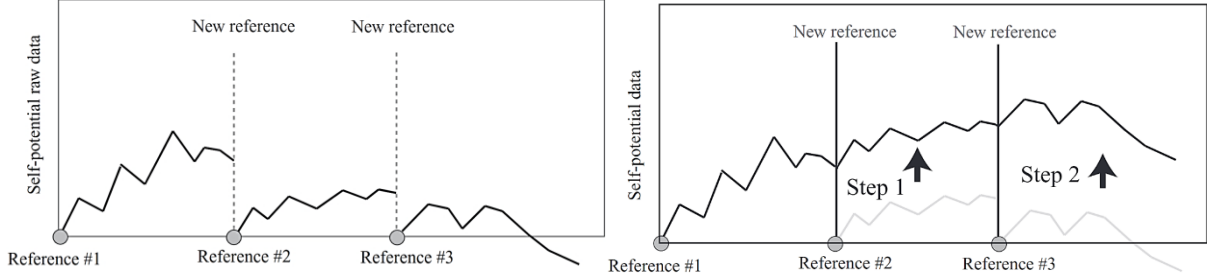


Figure 10: reference correction (modified from Revil & Jardani, 2013)

3.2.2 Fundamentals of the self-potential method

The occurrence of self-potential signals is associated with the existence of electrical currents in the ground, which are in turn related to thermodynamic non-equilibrium situations that affect the transport of charge carriers in the ground (Revil et al., 2012). SP signals can originate from a variety of coupled processes (Grobbe & Barde-Cabusson, 2019; Revil & Jardani, 2013). Fluxes or flow that are the result of an actuating gradient of a different type than the flux or flow phenomenon itself can be named coupled processes and can occur as transport processes in porous media (Grobbe et al., 2021). Between the actuating and resulting flux, an underlying symmetry for the phenomenological coefficients exists, namely the Onsager reciprocal relations (Onsager, 1931).

The electrical double layer (EDL) (Fig. 11) plays often an important role in the generation of SP signals (Grobbe et al., 2021; Grobbe & Barde-Cabusson, 2019). This layer exists at the surface between solid particles (e.g. grain surfaces in a rock formation) and pore water in a fluid-saturated porous media (Arens et al., 2020; Revil & Jardani, 2013), and describes an electrochemical system coating the surface of the minerals (Revil & Jardani, 2013).

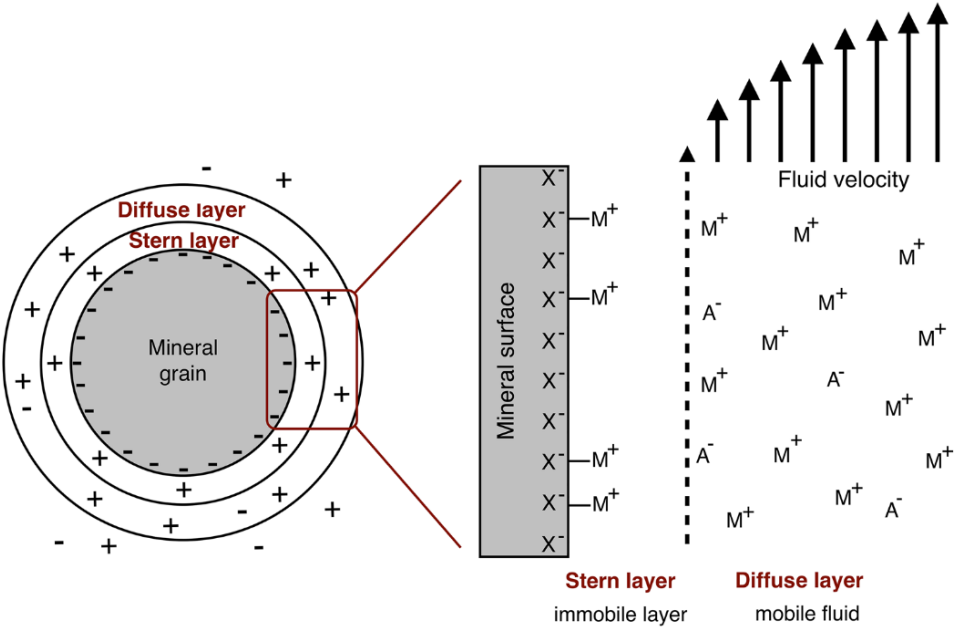


Figure 11: simplified illustration of electrical double layer (Arens et al., 2020)

Due to chemical reactions between the mineral surface and the pore water, a net charge is created on the mineral surface in a porous medium containing a fluid (Grobbe & Barde-Cabusson, 2019). The EDL is divided into the immobile Stern and mobile diffuse layers (Arens et al., 2020; Grobbe & Barde-Cabusson, 2019). The combined effect of the Stern and diffuse layer compensate surface charge (Grobbe & Barde-Cabusson, 2019). The Stern layer consists of adsorbed ions on the mineral surface (Revil & Jardani, 2013). An excess of ions of the opposite sign and a depletion of ions of the same sign is created concerning the free pore water located in the central part of the pores (Fig. 11) (Revil & Jardani, 2013). This results in the formation of a diffuse layer (Revil & Jardani, 2013).

According to Revil & Jardani (2013), three fundamental consequences are associated with the existence of the EDL: (1) the pore water is never neutral, (2) surface conductivity is created by an excess of electrical conductivity in the vicinity of the pore water-mineral interface (Eq. 3), and (3) the (non-dielectric) polarization of the porous material results from the double layer. The occurrence of SP signals associated with groundwater flow (streaming currents) is derived from the first consequence (Revil & Jardani, 2013). When interpreting direct current resistivity data, the understanding of electrical conductivity in porous materials is crucial, which stems from consequence two (Revil & Jardani, 2013). The third consequence plays an important role in the understanding of induced polarization (Revil & Jardani, 2013).

Electrokinetic, electrochemical, and thermoelectric effects are the most important source mechanisms in volcanic areas (Arens et al., 2020). In porous materials, the intensity of thermoelectric effects is extremely small (less than a few tenths of $\text{mV } ^\circ\text{C}^{-1}$) (Revil et al., 2004). Electrokinetic phenomena can occur as a consequence of the presence of EDL, such as the streaming potential phenomenon, where a hydraulic gradient creates an electric field (Revil & Jardani, 2013), and reciprocal electroosmotic phenomenon, where an electric field drives fluid flow (Grobbe et al., 2021). Further, electrochemical effects can also generate SP signals (Grobbe et al., 2021). These effects can be induced by the coupling between chemical gradients and electric current density or can be associated with redox processes, e.g. related to ore bodies, sulphides oxidation, and contaminant plumes (Grobbe et al., 2021). The thermoelectric effect is associated with the chemical potential gradients of the ions contained in the pore water in the presence of a temperature gradient according to Revil et al. (2004). The total thermoelectric coupling is partly dependent on the EDL (Revil & Jardani, 2013).

Macroscale structural and environmental features can additionally generate SP signals such as topographic effects and hydrothermal circulation effects (Grobbe et al., 2021; Grobbe & Barde-Cabusson, 2019). Therefore, SP measurements can be complemented with electrical resistivity tomography surveys or other geophysical methodologies informing on the subsurface electrical conductivity when interpreting them (Grobbe et al., 2021).

3.2.3 SP measurements in the study area

All five locations of the ERT profiles were used to perform SP data acquisitions with the same spacings as the ERT measurements. The used nonpolarizable electrodes were made of Cu/CuSO_4 (Fig. 12). The multimeter *Fluke 289* was used as a voltmeter. The insulated wire that connects both electrodes had a length of 30 m, which is rather short for carrying out SP measurements. A mix of bentonite, water, and salt was used to improve the electrical contact between the electrodes and the ground. The mix

was poured into the holes some minutes before measuring. The number of SP measurements was for profiles 1, 2, 3, 4, and 5 respectively 110, 90, 93, 93, and 77. The SP data was acquired on 30/08/2022 (profile 1), 31/08/2022 (profile 1), 01/09/2022 (profile 2 and 3), 02/09/2022 (profile 4), and 03/09/2022 (profile 4 and 5) during cloudy, rainy and sunny periods, the typical Icelandic weather.

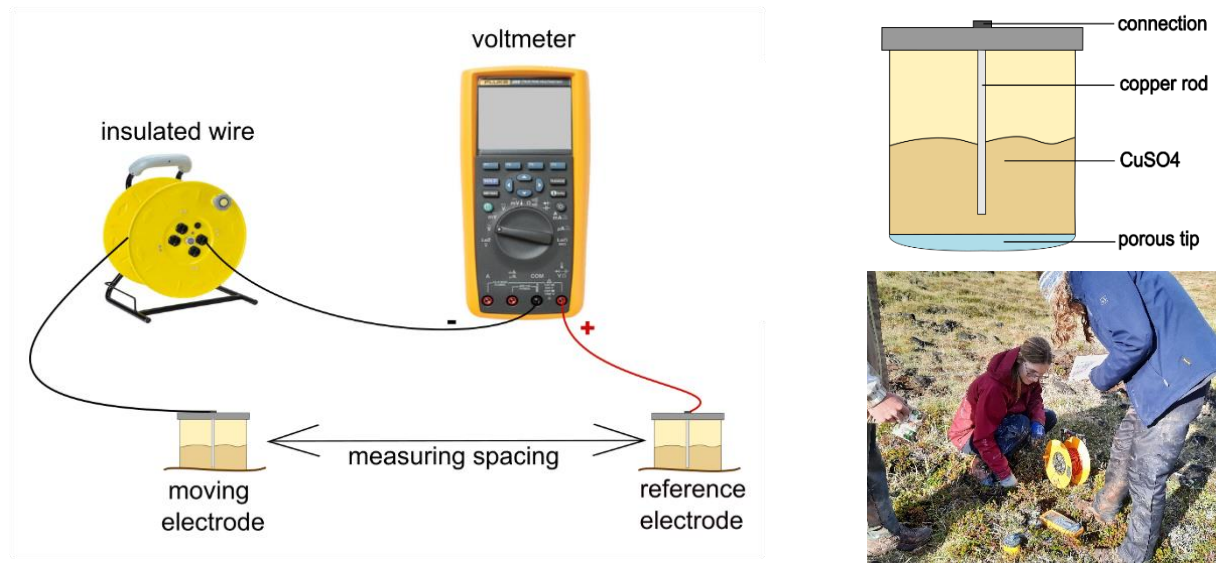


Figure 12: configuration of the self-potential survey with a schematic representation of the Cu/CuSO₄ electrode (not to scale) and a picture of the SP acquisition during the fieldwork

The closed loop technique was not used, which introduces a systematic error in the measured SP data (Grobbe et al., 2021). A correction for the closure error could therefore not be performed. The closure error is due to the propagation of errors in the changes of the reference electrode. This can result in the accumulation of errors toward the end of the profiles (Revil & Jardani, 2013).

According to Revil & Jardani (2013), there is always a temperature dependency on the potential of the electrodes. Cu/CuSO₄ electrodes have a substantially higher temperature dependence (0.7-0.9 mV °C⁻¹) (Antelman, 1989) than Petiau (Pb/PbCl₂) electrodes (Revil & Jardani, 2013). Temperature dependency is minimized in the Petiau electrodes, which have a temperature dependence in the order of 0.2 mV °C⁻¹ (Revil & Jardani, 2013). In the acquired SP data, this temperature dependency is not significant compared to the amplitude of the measured signal.

As stated by Revil & Jardani (2013), the use of salty water during SP mapping is strongly recommended to avoid. Highly variable and localized diffusion potential is created between the electrodes and the ground in the presence of salty water. Drying the saline solution results in potential changes over time (Revil & Jardani, 2013).

The usage of bentonite at each SP point helps hold the potential drop between the electrodes and the ground constant in space and time (Revil & Jardani, 2013). In the opinion of Revil & Jardani (2013), the bentonite should be poured into the SP holes 10 minutes before measuring to stabilize. For this study, the bentonite was poured into the SP holes a few minutes before measuring.

3.3 Temperature, soil moisture, CO₂ and precipitation data

The Temperature-Moisture-Sensor (TMS) is used to measure long-term temperature and soil moisture (Wild et al., 2019). This elongated device has an underground part where the soil moisture

sensor is located. The soil moisture sensor works on the time-domain transmission principle. Grain size analysis should be carried out to calibrate the volumetric soil moisture data so quantitative interpretations can be made. In this study, the soil moisture data is only relatively interpretable. The soil moisture reflects the saturation level of the subsurface which is influenced by the precipitation. Three other independent sensors measure the air, surface, and soil temperature simultaneously. Every 15 minutes, temperature and soil moisture measurements are carried out. According to Wild et al. (2019), the TMS has sufficient memory to acquire data for almost 15 years. Along the monitoring profile, two small and six larger TMS were installed (Fig. 6). The middle (surface) sensor measures the temperature at a specific depth as shown in table 2. The deep (soil) temperature sensor measures 6 cm deeper than the middle temperature sensor. The median temperature and soil moisture of each day is calculated for each sensor on each TMS device. The atmospheric temperature is calculated as the average of atmospheric temperatures measured on the eight TMS devices.

Table 2: depth from the surface in cm for each middle/surface temperature sensor

TMS device	61	62	91	92	93	94	95	96
Depth (cm)	0.0	0.0	15.0	12.5	12.0	22.5	15.0	22.0

Carbon dioxide measurements are carried out by the Vaisala CARBICAP® (Vaisala, 2023). This is based on single-beam and dual-wavelength non-dispersive infrared (NDIR) technology. Common drift factors, which are normally associated with all other NDIR sensors, are eliminated with this type of CO₂ measuring instrument. One measurement device is installed in the study area (Fig. 6). Every hour the device measures the CO₂ flux. The carbon dioxide flux per day is calculated as the median of the carbon dioxide flux measurements per day.

The used precipitation data is retrieved from the Icelandic Meteorological Office (Veður). They measure the amount of precipitation every 10 minutes in Grindavík (Fig. 2), about 12.5 km from Gunnhver. The precipitation for each day is calculated by the sum of the amount of precipitation observed every 10 minutes for each day.

All this data can be compared with the resistivity of one cell of the monitoring profile through time. These cells are chosen as the most shallow and closest resistivity cells of the 1a mesh to TMS 61 and TMS 94. All the raw data and results are stored in the 'erupt' OneDrive file of Lore Vanhooren.

4 Characterization study

4.1 Absolute inversion with error model

The measured resistivity of the subsurface using normal and reciprocal measurements should be identical according to the principle of reciprocity (section 3.1.3). However, due to measurement errors or noise in the study area, this is not the case. Reciprocal measurements were carried out for profiles 2, 3, 4, and 5. No reciprocal measurements were executed for profiles 1a and 1b as mentioned before. The error model of profile 1 is therefore determined using the overlapping part of profiles 1a and 1b. The electrodes of profile 1a are used as normal measurements and the electrodes of profile 1b as reciprocal measurements.

The envelope function (Slater et al., 2000) to determine the error model is not used in this project. This is a subjective and conservative approach. In the construction of a trendline (Fig. 13), a less conservative approach is used to estimate the errors (Koestel et al., 2008). The linear error model method is however more susceptible to artefacts. Generally, 10 % is chosen as a threshold value (Slater

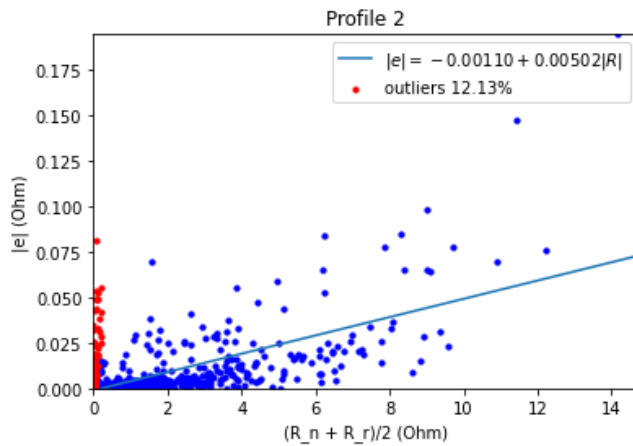


Figure 13: linear error model of profile 2 with threshold 10 %

et al., 2000). The cut-off value of 5 % is also explored because a relatively low amount of outliers is observed using the 10% threshold (Appendix B) (table 3). The cut-off value of 5% results however in too many outliers for profiles 1 and 2 and is hence not used further in the characterization study.

The reciprocal error $|e|$ varies between 0 and 0.2 Ω . The outliers are mainly values with an average resistance between 0 and 1 Ω .

Parameters a and b are defined as respectively the absolute error and the increase in the magnitude of the reciprocal error with the magnitude of measured resistance for the dataset after the removal of the outliers. For different thresholds, the parameters a and b , and the percentage of outliers of each characterization profile are listed in table 3. The higher value of parameter b of profile 1 compared to profiles 2, 3, 4, and 5 is probably due to the slightly different location of the overlapping electrodes of profiles 1a and 1b (Fig. 6).

Table 3: parameters of error model per characterization profile

Profile characterization	10 %			5 %		
	a (Ω)	b (%)	outliers (%)	a (Ω)	b (%)	outliers (%)
1 (1a+1b)	-0.00095	2.029	3.36	-0.00125	2.044	20.61
2	-0.00110	0.502	12.13	-0.00125	0.505	17.31
3	0.00043	0.294	3.31	0.00009	0.302	6.79
4	0.00027	0.258	3.08	-0.00003	0.266	6.16
5	0.00008	0.791	0.17	0.00004	0.755	1.23

In the constant linear error model, the error parameters are constant during the inversions of the different profiles. While in the variable linear error model, specific parameters for each profile are used during the inversions. The individual error is determined by calculating the reciprocal error (Eq. 7) for each measuring point of each profile. Individual errors could only be determined for profiles 2, 3, 4, and 5.

4.1.1 The constant error model

Inversions of profile 1 are carried out using the parameters b is 1 %, and a is 0.01, 0.005, 0.001, 0.0005, 0.0001, and 0.00005 Ω to investigate which a value should be used to improve the inversion (Fig. 14).

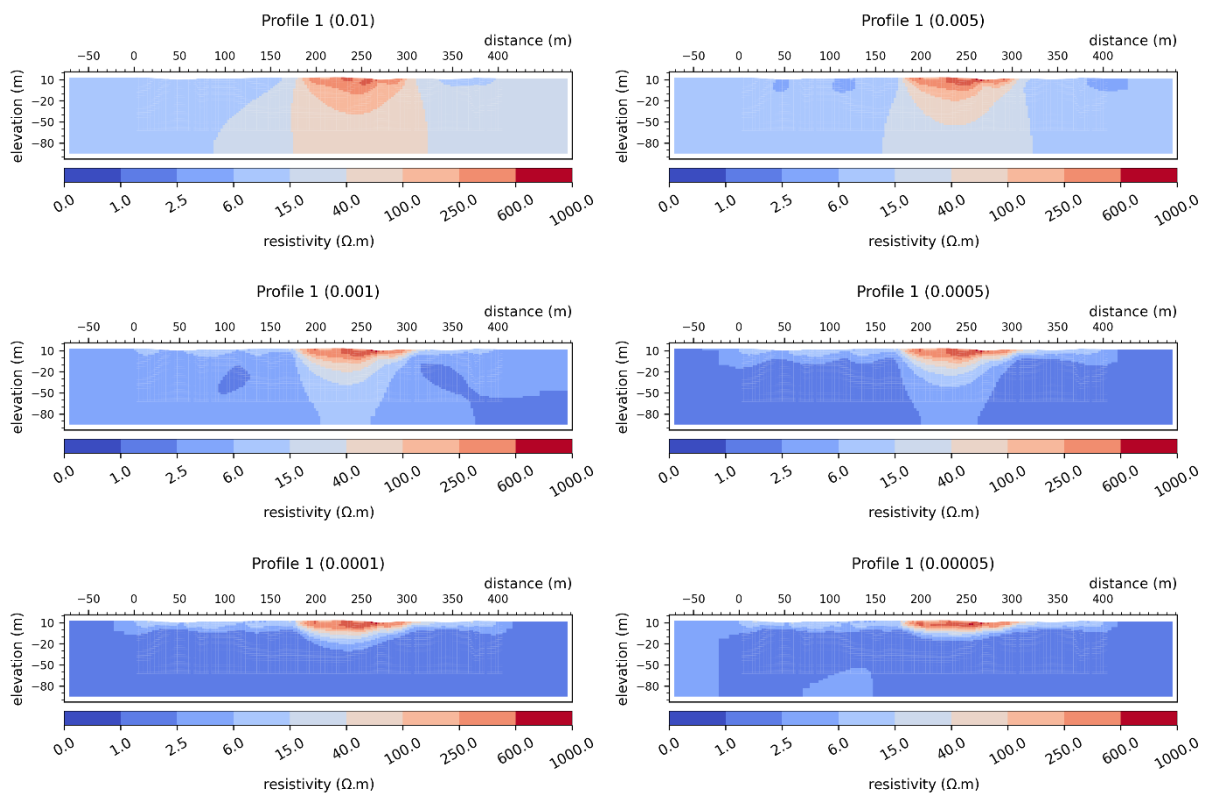


Figure 14: resistivity models of absolute inversions of profile 1 with the a value between brackets

Values of a closer to 0 result in inversions with lower resistivity values in deeper zones, a smaller zone of lower resistivity beneath the high resistive zone, and more delineated shallow low resistive zones (Fig. 14). This is expected, lower a values will force the inversion to fit the low resistance data better. The number of iterations for a are 0.01, 0.005, 0.001, 0.0005, 0.0001, and 0.00005 Ω respectively 4, 4, 6, 6, 7, and 5.

Further, absolute inversions of the characterization profiles using the constant linear error model are carried out with parameters a is 0.0005 Ω and b is 1 % (Appendix B). This specific value of parameter b is chosen as a compromise between the calculated b value of 2 % for profile 1 and values 0.3 - 0.8 % for the other profiles (Table 3). Parameter a is chosen as 0.0005 Ω because this is the smallest value without creating a too optimistic inversion model.

The result of an absolute inversion with the constant error model parameters of profile 2 is shown in figure 15. The decrease of resistivity below high resistive zones is very smooth.

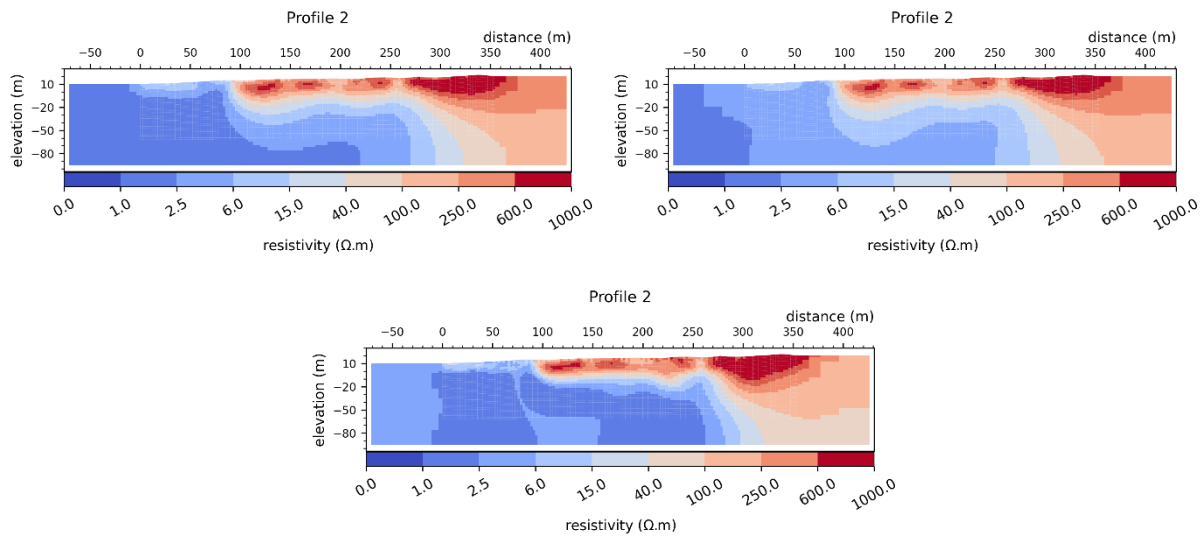


Figure 15: resistivity models of absolute inversions of profile 2 with the constant error model (left), the variable error model (right), and the individual error (middle)

4.1.2 The variable error model

To limit the smoothing, the variable error model is used for the absolute inversions of profiles 2, 3, 4, and 5. The parameters a and b used for the absolute inversions of profiles 2, 3, 4, and 5 with the variable error model are specific for each profile and are defined by the 10 % cut-off. A negative minimum error is observed for profile 2. This is not realistic. A positive value of 0.00110Ω was therefore used during the inversion.

The inversion with the specific error model parameters results in an ERT profile with more smoothing (Fig. 15). Higher resistivity values are observed with depth compared to the inversions with the constant error model. This can be explained by the parameter a . The latter is for profile 2 higher in the inversion with the variable error model (0.00110Ω) compared with the constant error model (0.0005Ω).

For the inversions of profiles 3, 4, and 5, the parameter a is lower in the variable error model than in the constant error model (table 3). Less smoothing is therefore observed in the inversion results of these profiles (Appendix B).

4.1.3 The individual error

The individual error, a less conservative method, is used for profiles 2, 3, 4, and 5 during the absolute inversions (Appendix B). Twenty iterations, the self-defined maximum of iterations, were reached for each inversion of each profile.

The inversion of profile 2 using the individual error results in less smoothing compared with the absolute inversion using the linear error models (Fig. 15). Between 270 and 350 m, a deeper resistive zone is observed compared with the inversion with linear error models. The lowest resistive zone occurring beneath 0 m elevation is not observed over the whole profile in contrast to the inversion with linear error models but is surrounded by a zone of slightly higher resistivity values. Small vertical

structures are observed around 75 m and 260 m along profile 2. These can be small artefacts because these vertical structures are not expected based on the measuring configuration (section 3.1.2).

4.2 Absolute inversion with a homogeneous reference model

To optimize the ERT results, reference model inversions with the different types of error models are carried out for the five characterization profiles. The reference model consists of one background value that is allocated to each cell of the grid. The weights of this allocation or closeness factor is kept constant and amounts 0.01. This value determines the importance of the background value for each cell during the inversion (Eq. 14). Prior knowledge about the study area provides a more realistic solution in the determination of the background value. There was however no prior knowledge available for this study area. The determination of the background value is therefore based on the average apparent resistivity which varies over the five profiles and was chosen as 1.0 Ω .m.

The depth of investigation (DOI) and the cumulative sensitivity matrix are used to determine the reliability of the calculated ERT model with depth (Caterina et al., 2013; Oldenburg & Li, 1999). To determine the DOI, two inversions are carried out with a varying reference model. The values of the reference models are determined as 0.1 and 10 times the average of the measured apparent resistivity values (Oldenburg & Li, 1999). DOI values between 0 and 0.2 represent zones that are well-constrained by the data (Oldenburg & Li, 1999). The sensitivity model visualises how specific areas of the imaging region are 'covered' by the data according to Caterina et al. (2013).

4.2.1 The constant error model

For profile 1, two different inversions with a homogeneous reference model but with different error model parameters are carried out. The first inversion has error model parameters a is 0.0005 Ω and b 1 %. The second inversion has the same value for parameter b , but the value for parameter a is 0.0001 Ω . These different a parameters are chosen to determine which value is better to use during the inversions with a conservative error model (Fig. 14).

The first inversion shows a zone of DOI values smaller than 0.2 in the first 30 m depth (Fig. 16). This is also the depth where a rapid increase of DOI values is observed and so a loss of reliability can be derived (Caterina et al., 2013). The sensitivity model shows a similar range of interpretable depth intervals. From the DOI of the second inversion ($a = 0.0001 \Omega$), a loss of reliability between -20 and -50 m elevation is observed. Lenses of higher DOI values are observed in the lowest DOI-value zone. The inversion with parameter a is 0.0005 Ω is more conservative and is chosen to use during the further inversion with a constant linear error model.

Based on the DOI and sensitivity models, the depth of investigation and high sensitivity zone is lower than expected based on the electrode configuration of 72 electrodes with 5 m spacing. This is probably related to the extremely high conductivity at shallow depths in the study area.

A shallow high resistive zone is observed along profile 1 between 180 and 300 m (Fig. 16). In the shallow parts left and right of the high resistive ($> 40.0 \Omega$.m) zone, lower resistive (2.5-15.0 Ω .m) zones are observed. Beneath these shallow high and lower resistive zones, one big low ($< 2.5 \Omega$.m) resistive zone is observed.

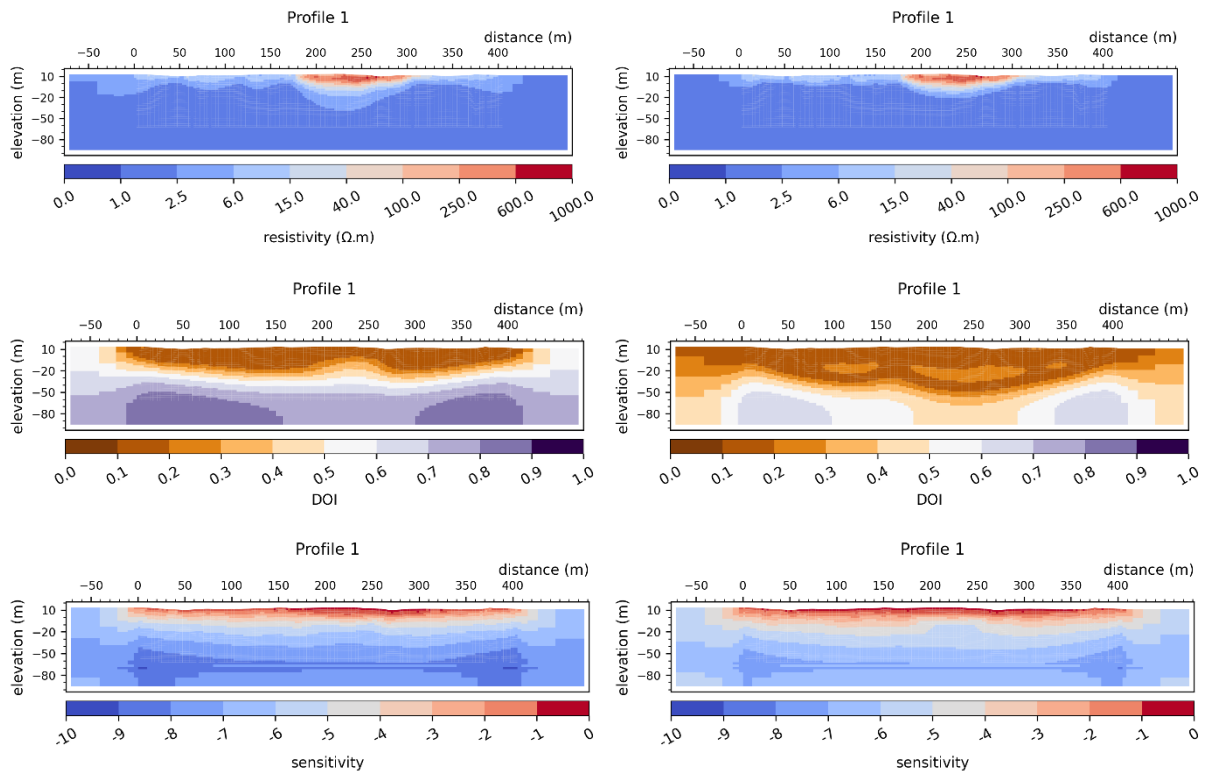


Figure 16: resistivity, DOI, and sensitivity model of the reference model inversion of profile 1 with a is 0.0005 and b is 1 % (left column) and a is 0.0001, and b is 1 % (right column)

The sensitivity model of profile 2 shows relatively high sensitivity until about -30 m elevation (Fig. 17). Depths larger than 40 m can be interpreted but with caution. Similar caution is needed for the edges of the grid where the sensitivity is also lower. The maximum reliable depth interval observed from the DOI model of profile 2 amounts 50 m. Small lenses of higher DOI values are observed in the 0.1-0.2 DOI value zone. The inversion, sensitivity, and DOI models of profiles 3, 4, and 5 can be found in appendix B.

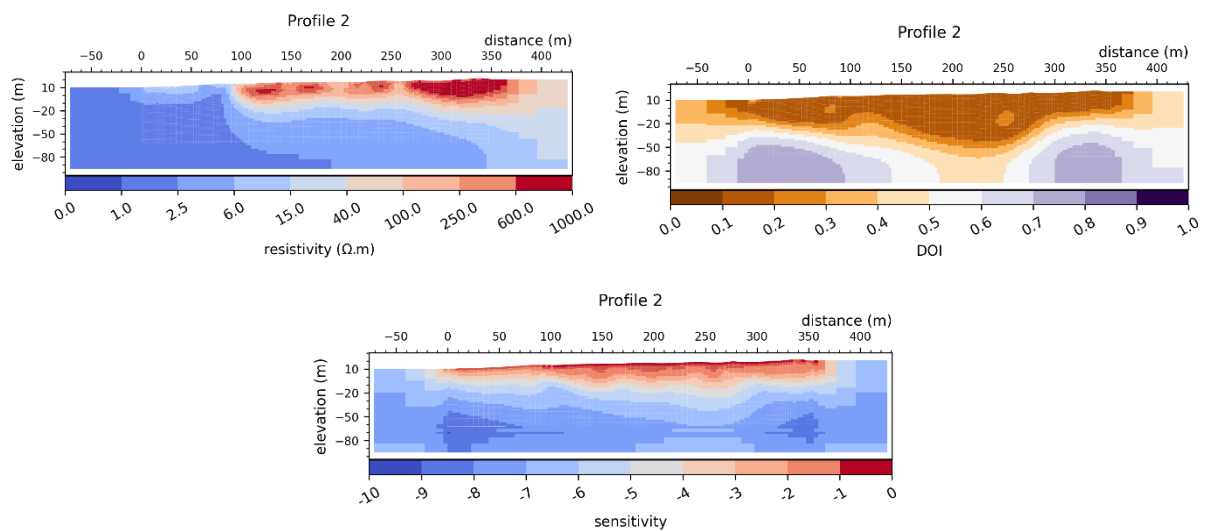


Figure 17: resistivity, DOI, and sensitivity model of the reference model inversion with the constant error model of profile 2

Shallow high resistive zones with varying dimensions and resistivity values are observed between about 100 and 360 m along profile 2 (Fig. 17). A lower (2.5-15.0 $\Omega\cdot\text{m}$) resistive zone is observed between 0 and 50 m at shallow depth. A low (< 2.5 $\Omega\cdot\text{m}$) resistive zone is again situated beneath the shallow low and high resistive zones. The shallow high (> 40.0 $\Omega\cdot\text{m}$) and low (2.5-15.0 $\Omega\cdot\text{m}$) resistive zones can be related to surface manifestations such as respectively unaltered rocks and clay/altered zones.

4.2.2 The variable error model

To investigate slightly less conservative reference model inversions, the variable error model is used. This error model consists of the parameters a and b shown in table 3. The reference model inversion with the variable error model of profile 2 (Fig. 18) shows less smoothing compared with the inversion with the constant error model (Fig. 17). The reference model inversion with the variable error model of profile 2 results also in less smoothing compared with the absolute inversion without the use of a reference model and with the variable error model (Fig. 15).

To check the reliability of this type of inversion, the DOI was calculated. According to the DOI of profile 2, the inversion is reliable until 100 m depth between 200 and 250 m along the profile. The usage of the variable error model resulted in constraining the resistivity at depth to be low. The results of the inversions, DOI, and sensitivity models of profiles 3, 4, and 5 are shown in appendix B.

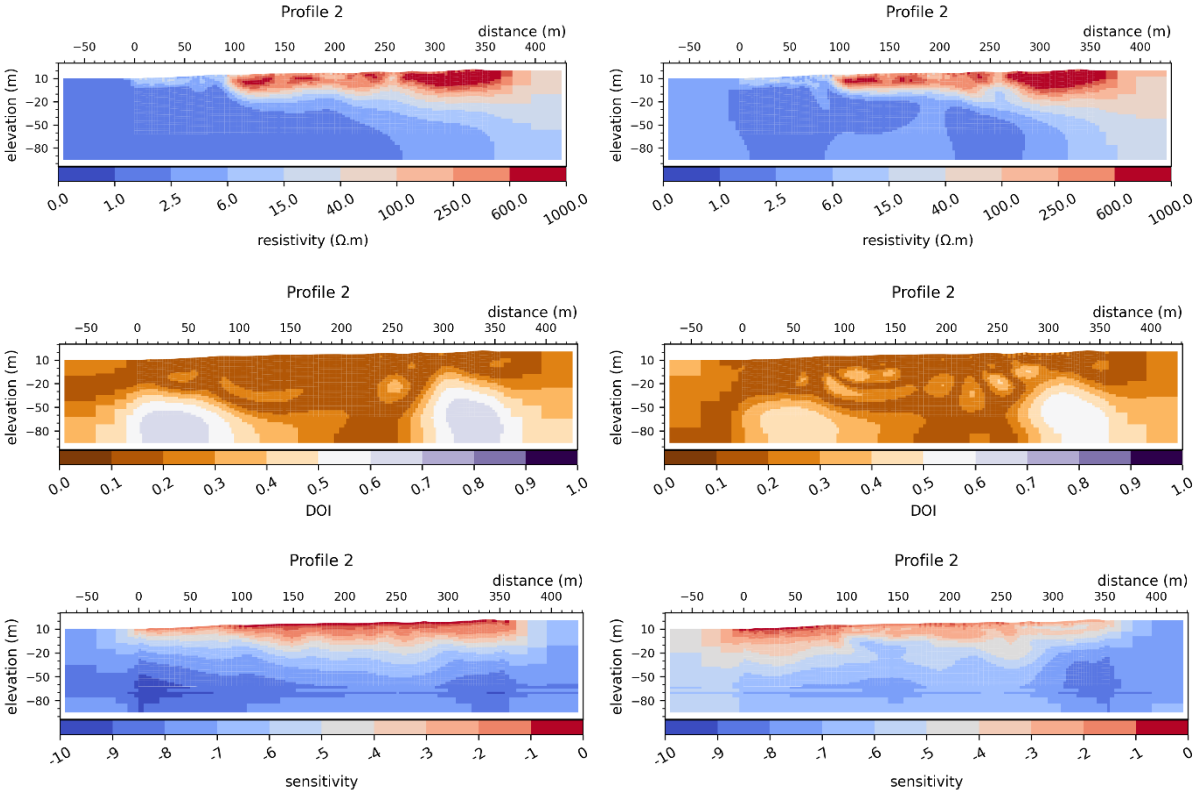


Figure 18: resistivity, DOI, and sensitivity model of the reference model inversion of profile 2 with the variable error model (left column) and the individual error (right column)

4.2.3 The individual error

Due to the use of the reference model, the resistivity value decreases more rapidly with depth beneath the highest resistive zone (Fig. 18). The zone of the low (< 2.5 $\Omega\cdot\text{m}$) resistivity values is

observed in blobs instead of a homogeneous low resistive zone observed in the inversions with the other error models. Profile 2 has DOI values between 0 and 0.2 in very deep zones (Fig. 18). A lot more lenses of higher DOI values are observed compared with the DOI of profile 2 using the variable error model. These lenses are probably partly artefacts. From profiles 3, 4, and 5 similar DOI results are observed (Appendix B).

A possible manner to keep using the individual error but in a more conservative way is to use a safety factor multiplying the estimated individual error. This is however not further tested because no individual error could be calculated for each profile. The individual error is hence not used further in this study.

4.2.4 Discussion

Similar results are observed from the absolute inversions with the variable error model (Fig. 15) and the reference model inversion with the constant error model (Fig. 17). The reference model ensures the constraining of the inversion at depth. The absolute inversion with the variable error is preferred because less subjectivity is included. The value of the reference model is namely chosen without prior knowledge. The risk of having artefacts is higher with the variable error model compared with the constant error model but can be limited by error model calculations.

All three types of error models show similar results in the shallow subsurface of the reference model inversion results. The individual error is however most likely too optimistic for this characterization study. The self-defined limit of iterations is always reached and small artefacts are observed in the inversion results. Only small differences between the two reference model inversion results with the constant and the variable error model are observed. Both inversion results can be used to make qualitative interpretations. More delineated structures are observed in the results of the reference model inversions with the variable error model. This inversion type is hence used for the interpretation of the characterization study.

4.3 Self-potential results

After applying the drift correction per section and the reference correction for the entire profile, each profile was plotted with error bars of one standard deviation. Anomalies are observed on the five graphs of the five profiles (Fig. 4.20, 4.22). Relative variations in the observed SP signals, not the absolute values of the SP anomalies, should be interpreted because SP measurements are relative measurements (Grobbe et al., 2021). In the opinion of Grobbe & Barbe-Cabusson (2019), the interpretations of SP data always benefits from a joint study with results obtained from other data types. Combining SP data and other geophysical and/or geochemical data types, and basic geology knowledge of the study area is therefore essential (Grobbe & Barde-Cabusson, 2019). The SP results are hence only discussed in detail in the next section.

The SP signal is reasonably constant along profile 3 compared to the other profiles, which is also expected based on field observations and ERT measurements. The closure correction (Revil & Jardani, 2013) could not be used at the five profiles because of the measurement configuration. Profile 3 is therefore used as a base for the calibration of profiles 1, 2, and 4.

Profile 3 has intersection points with profiles 2 and 4 at respectively 180 and 275 m. Profile 1 intersects profiles 2 and 4 at respectively 125 and 280 m. By calibration with profile 3, the SP signal of profile 1 is two times recalculated, one time through profile 2 and the other time through profile 4. If the measurements would be perfect, profile 1 determined through profile 2 should be the same as profile 1 determined through profile 4. A difference of 22.5 mV is however observed between the SP signal of profile 1 at 280 m through profile 2 and at 280 m through profile 4 (Fig. 19).

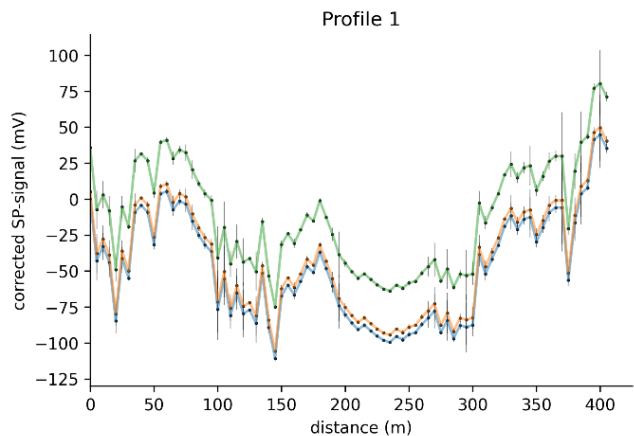


Figure 19: original corrected SP-signal of profile 1 in blue, determined through profile 2 in green, and determined through profile 4 in orange

Although the closure correction could not be carried out which can lead to an accumulation of errors towards the end of the profiles (Revil & Jardani, 2013), the SP results can partly be interpreted. The scale of the corrected SP signal is between -125 and 100 mV. The error determined by recalibration is 22.5 mV. This is 10 % of the range of the corrected SP signal. The big trends of the SP signal are therefore interpretable considering the 10 % error range and the error bars of 1 standard deviation.

4.4 Discussion

The results of the reference model inversions with the variable error model are combined with the IP and SP results for the characterization of the study area. The visual observations along profile 1a made during the field campaign are also used in combination with the geophysical results for interpretation. Part of the ERT and IP results are removed to avoid confusion as the deeper zones and sides of the profiles are less reliable.

Low resistive zones (2.5-15.0 Ω .m) are observed along ERT profile 1 at 0-180 and 300-410 m (Fig. 20). From the SP results are positive anomalies observed in these zones which can indicate up-flow of hydrothermal fluids (Grobbe & Barde-Cabusson, 2019). Mud cracks, smoke, and other field observations were observed during the field surveys in these zones. The IP results show very small chargeability values for these shallow low resistive zones. The low chargeability is also influenced by the resistivity. Charging conductive zone is namely more difficult. No IP signal was therefore recorded at depth. The normalized chargeability is calculated to visualize the altered zones more clearly. Note that the IP and normalized chargeability results are only preliminary results.

Between 0 and 180 m, and 300 and 410 m, alteration zones are situated and created by ongoing hydrothermal activity based on the observed SP anomalies, the low chargeability, the higher values of the normalized chargeability, the low resistivity occurring in these shallow zones, and the visual observations (Fig. 20). Around 50, 120 and 400 m along ERT profile 1, even smaller resistivity values (< 6.0 Ω .m) are observed. Precipitation of clay, smoke, mud pools, hot air, mud cracks, and high ground temperatures are observed in these three highly altered zones. The very low resistivity is maybe partly created by the occurrence of clays, for example, smectite. This clay has a high conductivity which can be enhanced by high temperatures (Lévy et al., 2019).

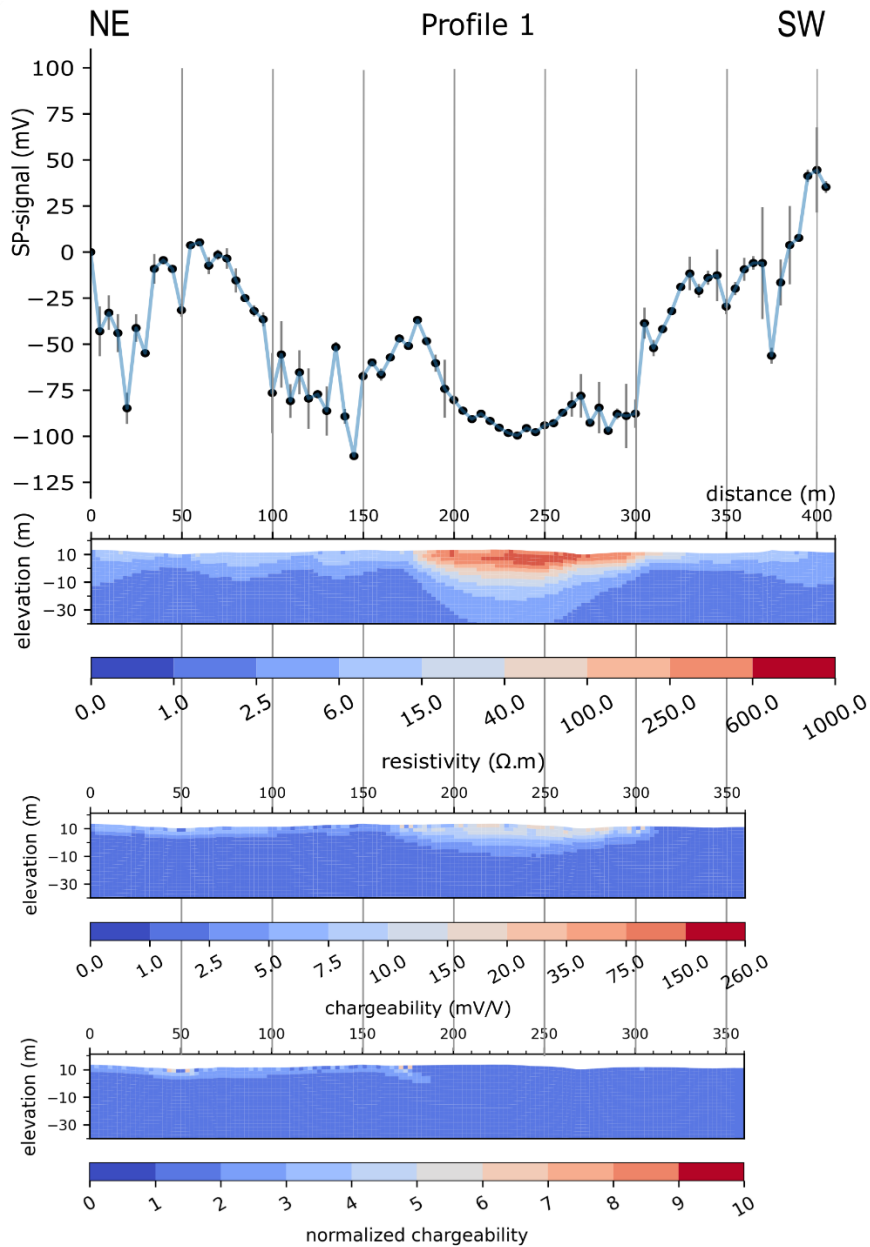


Figure 20: SP, ERT, and IP results of characterization profile 1

A high resistive zone ($> 40.0 \Omega.m$) is located between the low resistive zones at 180 to 300 m along ERT profile 1 (Fig. 20). Higher chargeability values compared with the neighbouring zones are observed on the IP result of profile 1. However, no higher values are observed on the normalized IP results. A reasonably low and constant SP signal is observed between 180 and 300 m. The high resistivity, medium chargeability, constant SP signal, and visual observations of outcropping rocks are due to the presence of basalts. These rocks are probably less hydrothermally altered compared with the other zones along profile 1.

The low resistive zones between 0 and 180 m, and 300 and 410 m along profile 1 can thus be interpreted as hydrothermal alteration zones with the highest altered zones located at around 50, 120, and 400 m along profile 1 (Fig. 21). In between the low resistive zones, a high resistive zone is situated and is interpreted as basalts with the lowest grade alteration observed in the study area. Due to the

geothermal activity of the VHS, the produced heat will warm up the subsurface fluids. These fluids can migrate to the surface and warm up the ground, create mud pools, or contribute to the precipitation of clays.

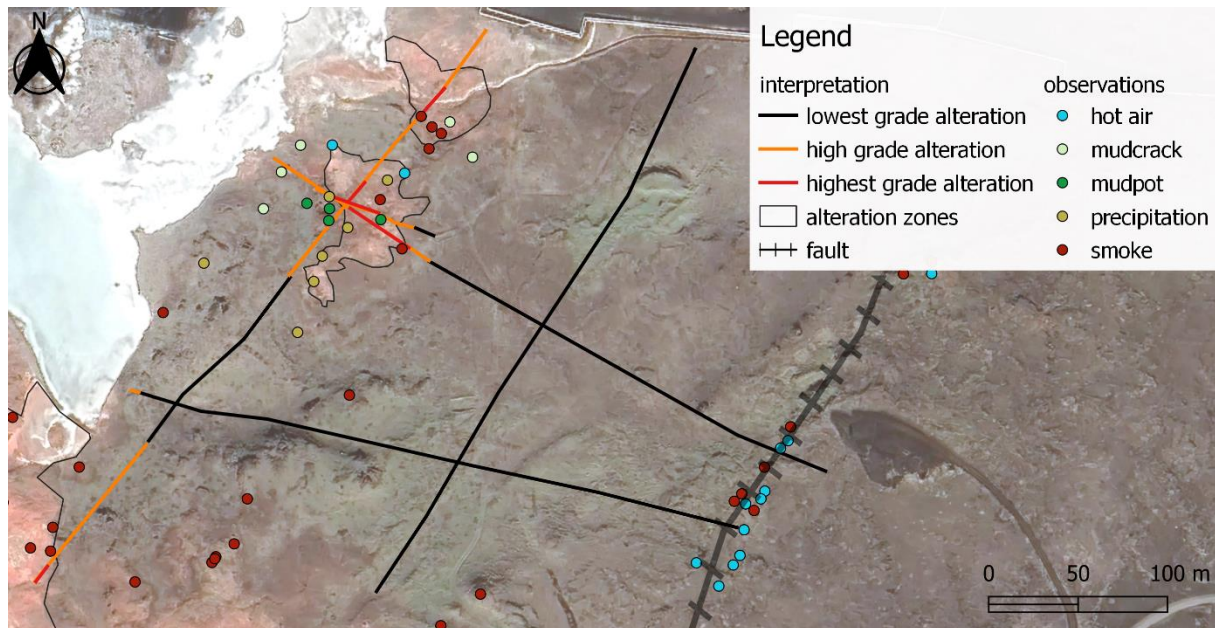


Figure 21: interpretation of alteration grade of characterization profiles 1, 2, 3, 4, and 5 in the study area

On the ERT inversion of profile 2, two distinguishable zones are observed (Fig. 22). Until about 90 m along ERT profile 2, low resistive values are observed, while from 90 m onwards, a shallow high resistive zone is observed. In the first 90 m of the SP signal, positive anomalies are observed. A relatively constant SP signal is observed from 90 to 270 m. The SP signal drops after 260 m, while the ERT model shows a homogeneous high resistive zone. The IP result shows a noisy model probably due to overfitting. Higher normalized chargeability values are observed in the first 90 m. Profile 2 crosses at around 50 m profile 1 so in an alteration zone. The first 90 m of profile 2 reflects probably a hydrothermal alteration zone because of the low resistivity and varying SP signal. To the SE, basalts are more prominently outcropping (Fig. 21).

The SP signal is relatively constant along profile 3 (Fig. 22). However, two small positive SP anomalies are observed around 175 and 300 m. High resistivity values are observed along ERT profile 3 with a thickness of about 30 m. The resistivity values decrease to the SW, where an alteration zone is situated (Fig. 21). Lower resistivity values are observed between 170-210 m, and 290-360 m along ERT profile 3. The IP inversions show slightly higher chargeability in two zones that have the same location as the higher resistivity values. This is due to the high resistivity zone because higher resistivity leads to measurements of higher potential values. The normalized chargeability model of profile 3 shows no higher values between 170-210 m, and 290-360 m. The upper 30 m of this profile is probably characterized by basalts with varying grades of alteration.

Along ERT profile 4, mainly a shallow high resistive zone is observed (Fig. 22). This high resistive zone thickens to the east. In the first 70 m along profile 4, the high resistivity values are only observed in the first 5 m. The SP measurement of the first 70 m result in a variable signal. The normalized chargeability has slightly higher values beneath a zone similar to the shallow high resistive zone along

the entire profile 4. Note the IP and normalized chargeability profiles have opposite directions compared with the SP and ERT profiles. Profile 4 probably reflects basalt with varying grades of alteration (Fig. 21).

The deeper part of the ERT profiles is dominated by very low resistivity values ($< 2.5 \Omega.m$) (Fig. 20, 22). This deeper zone reflects probably the hot and saline groundwater.

Profile 5 is measured with an electrode spacing of 1 m, which results in a 72 m long ERT profile instead of a 360 m long ERT profile as in profiles 1a, 2, 3, and 4. The resolution is therefore also higher in profile 5. This profile is potentially sensitive to other phenomena such as patterns of fluid circulation. Based on the visual observations during the field campaign, a very clayey zone is located from 0 to 57 m along profile 5. When electrodes were pulled out, the electrodes were very warm and steam was sometimes escaping from the holes created by the electrodes. At 3 and 4 m, no SP measurements were carried out during the field campaign, because a large mud pool was crossed. From 57 to 72 m, relatively un-weathered basalt was observed during the field campaign. Positive anomalies are observed along SP profile 5 (Fig. 22). Maybe these positive SP anomalies are the result of the up-flow of hydrothermal fluids. From the normalized chargeability, higher values are observed between 0 and 4 m, and between 18 and 38 m. The higher normalized chargeability values are reaching the surface between 26 and 28 m. To the east of the ERT profile 5, higher resistivity values are observed, which are the result of the less altered basalts in the subsurface. The lowest resistivity values observed on ERT profile 5 could be the result of the hot saline groundwater.

In the study area, the low resistive zones or high conductive zones correspond to shallow altered zones with varying degrees of hydrothermal alteration situated in the SW and NE of the study area. The alteration zones are linked to fluid dynamics. The very low resistivity observed at depth corresponds most likely with the hot saline groundwater. In the hydrothermal alteration zones, warm grounds, mud pools and precipitation of clays occur. Lateral variations are also observed in resistive and conductive zones. These variations are however more difficult to interpret. The more resistive zones are less altered zones consisting of basaltic rocks where the dissolution of the basaltic rock occurs continuously and clay-sized alteration minerals can potentially precipitate.

Positive SP anomalies are coinciding with active and hydrothermal altered zones, while low and stable SP results are observed in more resistive zones. The positive SP anomalies could be the result of the up-flow of hydrothermal fluids (Grobbe & Barde-Cabusson, 2019). Downward flow or chemical reactions between volcanic gases (H_2S , SO_2 , CO_2) and groundwater could be resulting in the negative SP anomalies (Grobbe & Barde-Cabusson, 2019; Zlotnicki & Nishida, 2003).

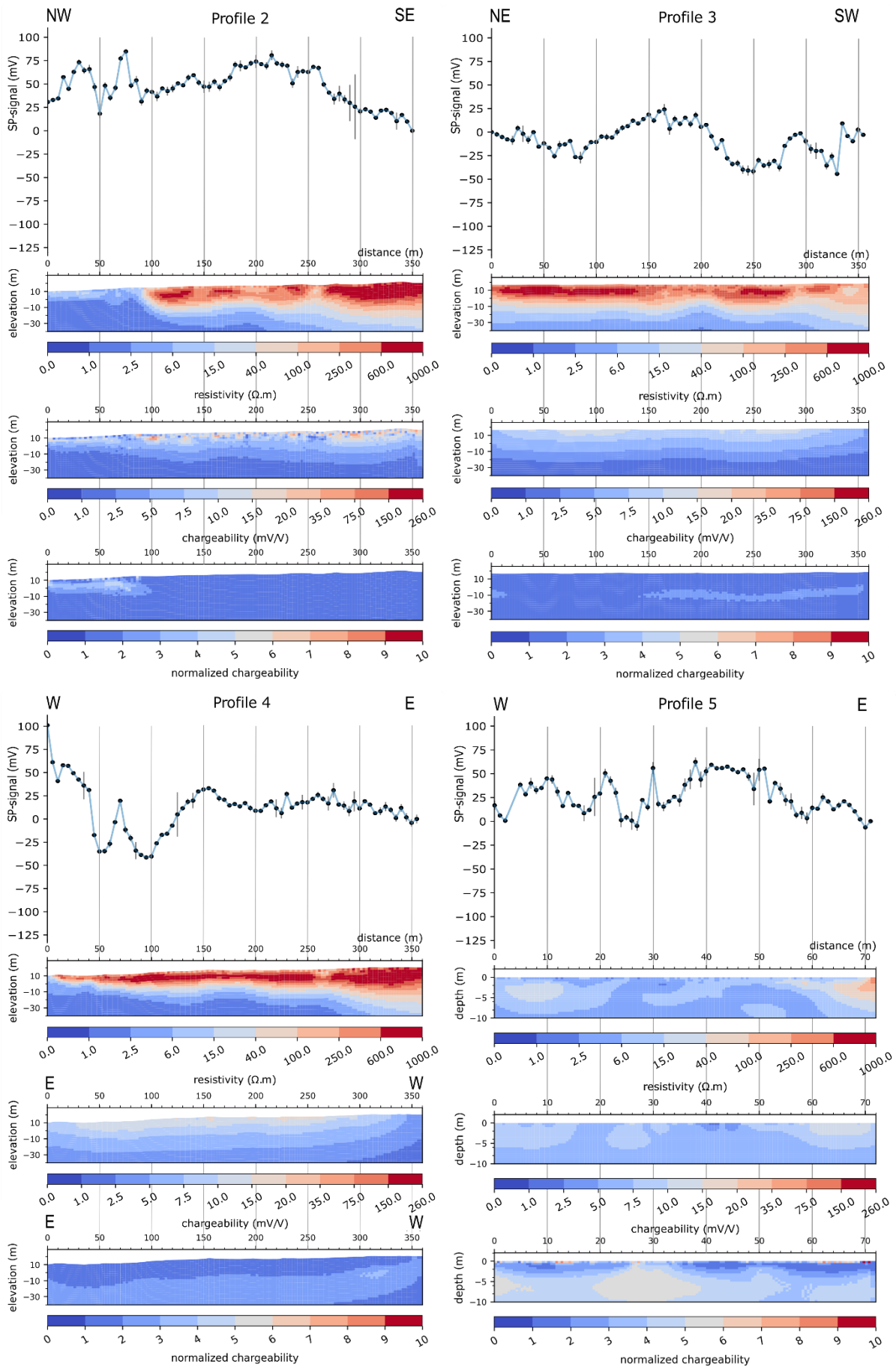


Figure 22: SP, ERT, and IP results of characterization profiles 2, 3, 4, and 5

5 Monitoring study

Absolute and time-lapse inversions with the constant and variable linear error model are used to investigate the ERT measurements collected since 23/10/2022. Five profiles (23/10/2022, 13/11/2022, 20/12/2022, 15/01/2023, and 17/02/2023) are selected and the inversions are partly shown here. The time-lapse inverted profiles from 24/10/2022 until 27/02/2023 are available online as Graphics Interchange Format (GIF).

5.1 Absolute inversion with error model

The constant linear error model has equal parameters as in the characterization study, so a is 0.0005 Ω and b is 1 %. The variable linear error model consists of error parameters specific to each monitoring profile. The specific error parameters for each day can be calculated because every day one reciprocal measurement is carried out since 23/10/2022.

The calculation of the parameters and outliers of the linear error model are listed in table 4 for a cut-off value of 10 and 5 %. The cut-off value of 5 % is not used because of the high amount of outliers. The minimum, maximum, and mean amount of outliers with a cut-off range of 10 % is respectively 7.76, 23.61, and 15.39 % between 23/10/2022 and 22/02/2023.

Table 4: parameters of error model per monitoring profile

Profile monitoring	10 %			5 %		
	a (Ω)	b (%)	outliers (%)	a (Ω)	b (%)	outliers (%)
23/10/2022	0.00015	0.487	14.80	0.00008	0.416	30.62
13/11/2022	0.00018	0.350	8.70	0.00007	0.300	19.15
20/12/2022	0.00023	0.651	18.86	0.00006	0.532	38.58
15/01/2023	0.00023	0.648	22.59	0.00008	0.520	44.76
17/02/2023	0.00019	0.497	14.06	0.00010	0.438	32.08

The amount of outliers obtained with a threshold of 10 % varies in the five chosen monitoring profiles. The locations of the outliers of the chosen monitoring profiles are visualized in pseudosections (Appendix C). No trend in the outliers locations is observed in the pseudosections between the day with the lowest and highest amount of outliers of the five profiles (Fig. 23).

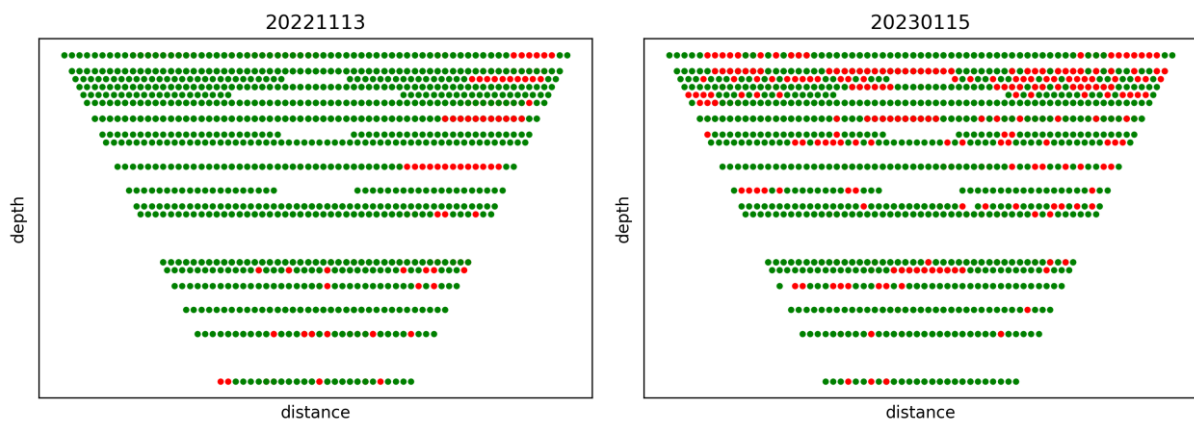


Figure 23: the pseudosection of day 13/11/2022 and day 15/01/2023 with in red the outliers

The average resistance, the amount of outliers, and the parameters a and b of the error calculations of the monitoring profiles are plotted in function of the time (Fig. 24). The global changes in the data sets are shown by the average resistance. The number of outliers and the parameters a and b of the error calculations are characteristic of the data quality and could be for example influenced by the contact resistance, so the surface conditions. The four variables show a similar trend except for February. The average resistance increases during February while the other variables do not show this increasing trend.



Figure 24: the average resistance in Ohm, the absolute error a in Ohm, the increase in the magnitude of the reciprocal error with the magnitude of measured resistance for the dataset after removal of the outliers b in percent and the number of outliers in percent between 23/10/2022 and 22/02/2023

The dashed lines highlight the chosen five days (23/10/2022, 13/11/2022, 20/12/2022, 15/01/2023, and 17/02/2023) (Fig. 24). The green band highlights the days 20/01/2023 and 21/01/2023. An abrupt drop in average resistance, a decrease in parameters a and b , and a small increase in outliers is observed between these two days.

More delineated, so less smoothed shallow high and low resistive zones are observed in the inversion with the variable error model in contrast to the inversion with the constant error model of the profile collected on 13/11/2022 (Fig. 25). The other absolute inversion results without the reference model can be found in appendix C.

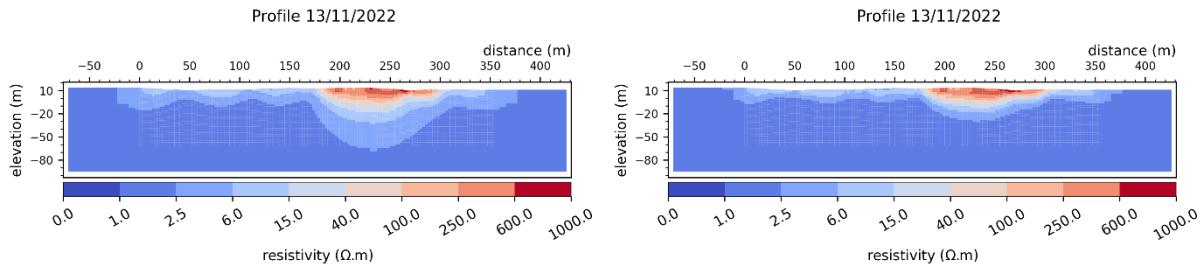


Figure 25: the absolute inversion with the constant (left) and the variable (right) error model

5.2 Absolute inversion with a homogeneous reference model

The reference model consists of the background value 1.0Ω and the closeness factor 0.01, which is identical to the homogeneous reference model of the characterization study. Again, inversions are carried out using a constant and variable error model. The sensitivity and DOI models are also used to investigate the reliability of the inversion. Note that the interpretation of these models remains subjective.

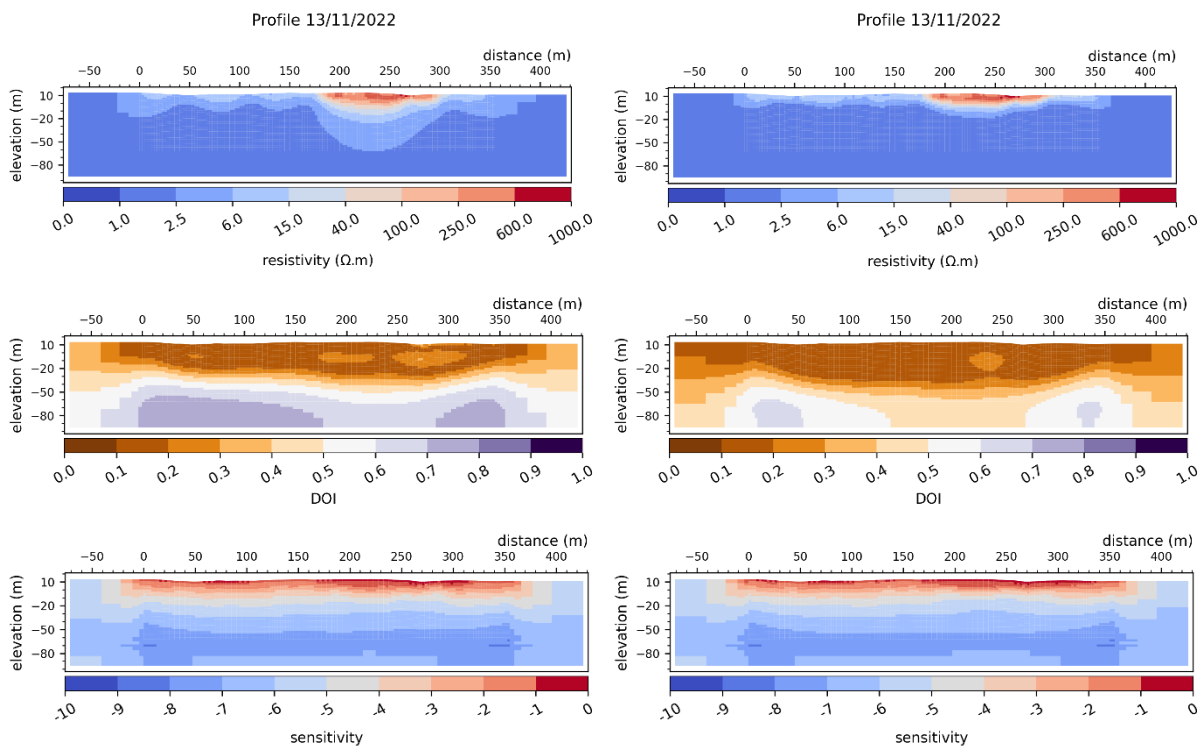


Figure 26: the reference model inversions with the constant (left column) and variable (right column) error model: the resistivity, DOI, and sensitivity models

The DOI model of the reference model inversions with and constant error model show DOI values smaller than 0.2 in the upper 30 m (Fig. 26). In the DOI models of profile 23/10/2022, 13/11/2022 and 15/01/2023, lenses with higher DOI values are observed (Appendix C). Based on the sensitivity of the reference model inversions with constant error model, the parameters have a small influence on the inversion results in the upper 30 m. The big structures of shallow high and low resistive zones remain observable in the reference model inversions with the constant error model. The use of the reference model in the absolute inversion has not improved the resistivity plot much compared with the disuse of the reference model.

The reference model inversion with the variable error model results in a DOI model with lower DOI values (Fig. 26). The zone of DOI values lower than 0.2 is deeper compared with the DOI model of the inversions with a constant error model. Also, higher DOI values in lenses situated in the upper 50 m of the model are observed in all the DOI models of the reference model inversion with the variable error model (Appendix C). The sensitivity model shows a similar result as the sensitivity model of the reference model inversion with the constant error model. Less smoothing is observed in the resistivity plot of the variable error model compared with the resistivity plot of the constant error model.

Inversions with the variable error model, a less conservative model, result in visualizing the high resistivity zone with less smoothing. While this smoothing, the slow decrease of resistivity values with depth, is observed in the inversions with the conservative constant error model. The use of the less conservative model results in inversions that are constrained by the deep data points with low resistance.

5.3 Time-lapse inversion

In time-lapse inversions, the differences in resistivity (in %) between inversions are calculated for each timestep with the initial time-step (background) used as a reference. That way, the inversion minimizes the differences with the reference image, and only the necessary features are created in the solution. The differences in resistivity (in %) between inversions of a profile is calculated using

$$\Delta\rho = \frac{\rho_i - \rho_{BG}}{\rho_{BG}} * 100 \quad (19)$$

where ρ_i and ρ_{BG} are respectively the resistivity of the time-lapse section and the resistivity of the background section. Quantitative interpretations of the inversion results can be made using this equation (Hermans, 2014). A negative percentage change of resistivity corresponds to a decrease in resistivity and is visualized with brownish colours in this study. Positive percentages correspond to an increase in resistivity or decrease in conductivity and are shown in greenish colours. Only differences in resistivity values between -50 and 50 % are visualized. This is sufficient to show the main changes and to allow small discrepancies to be visualized. Values of differences in resistivity between -10 and 10 % are considered artefacts. The closeness factor of the time-constrained inversions is 0.01 which is the same value as during the reference model inversions. The latter is also used to visualize the inversions between 24/10/2022 and 27/02/2023 with differences in resistivity ([Reference_model_constant_error.gif](#) and [Reference_model_variable_error.gif](#)). The background model for the time-constrained and difference inversion is the reference model inversion of the profile collected on 23/10/2022 with the constant or variable error model, depending on the used error model during the inversion.

Based on the sensitivity models of the time-lapse inversions with the constant and variable linear error model, the parameters are influencing the inversion results the least in the upper 40 m (Fig. 27). The edges of the grid, before 0 m and after 360 m, do not have sufficient reliability. The following inversion models are therefore visualized by cropping at depth and on the sides.

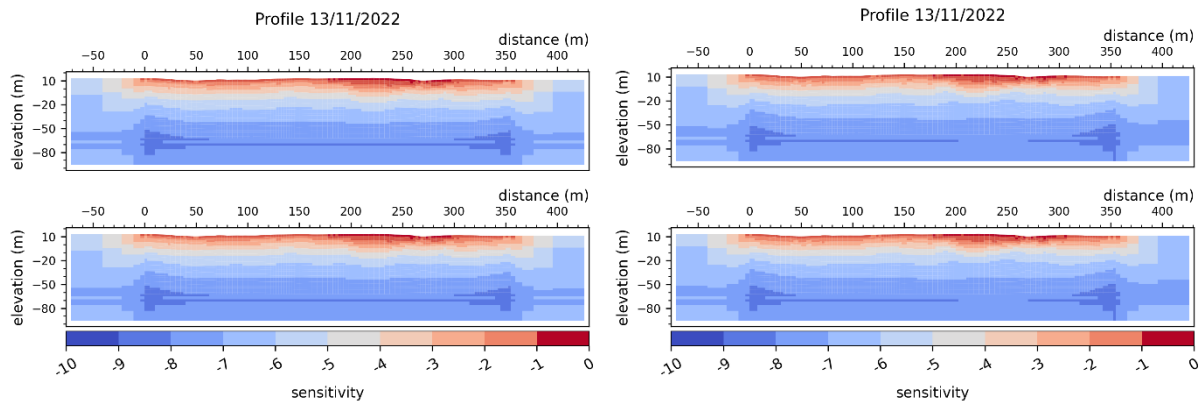


Figure 27: sensitivity models of the difference (upper row) and the time-constrained (lower row) time-lapse inversions with the constant (left column) and the variable (right column) error model

5.3.1 Time-constrained inversion

Time-constrained inversions with the constant error model are shown in the left column of figure 28. On 13/11/2022, very shallow increases in resistivity are observed around 10, 50, 110, 125, 160-180, and 260-340 m. The highest shallow increase in resistivity is observed between 260 and 300m. Between 180 and 260 m, a larger zone of resistivity increase is observed starting at 10 m depth. A small zone of decreasing resistivity is observed at 310 m. This small zone is larger in profile 20/12/2022. The shallow zones of increased resistivity of profile 20/12/2022 are similar to profile 13/11/2022. These shallow zones of increasing resistivity have higher values in profile 15/01/2023. Beneath this shallow increased resistivity zones are decreasing zones in resistivity observed at 20-90 m and 150-330m on profile 15/01/2023. These decreasing resistivity zones are also observed on profile 17/02/2023. The shallow increased resistivity zones of profile 17/02/2023 are similar to profile 15/01/2023. The GIF of the time-constrained inversion with constant error can be consulted via [Time constrained constant error.gif](#).

In the right column of figure 28, the time-constrained inversions with the variable error model are shown. From the ERT profile of 13/11/2022 is a zone of increased resistivity observed between 180 and 280 m with a maximum depth of 40 m. Between 260 and 280 m the highest increased resistivity zone is observed. Shallow increased resistivity zones are observed on profile 20/12/2022 around 50, 130, 320, 350, and between 180 and 290 m. A large zone of decreased resistivity is located beneath these shallow zones between 180 and 300 m with the largest decrease between 200 and 250 m. The shallow increase resistivity zones are also observed on profile 15/01/2023. On the latter are however larger zones of increased resistivity observed between 30-90 and 170-270 m instead of the decreased resistivity zone of profile 20/12/2022. The shallow zones of increased and decreased resistivity are similar in profile 17/02/2023 compared with profile 15/01/2023. A deeper zone of increased resistivity is observed between 260 and 280 m along profile 17/02/2023. The GIF of the time-constrained inversion with variable error can be consulted via [Time constrained variable error.gif](#).

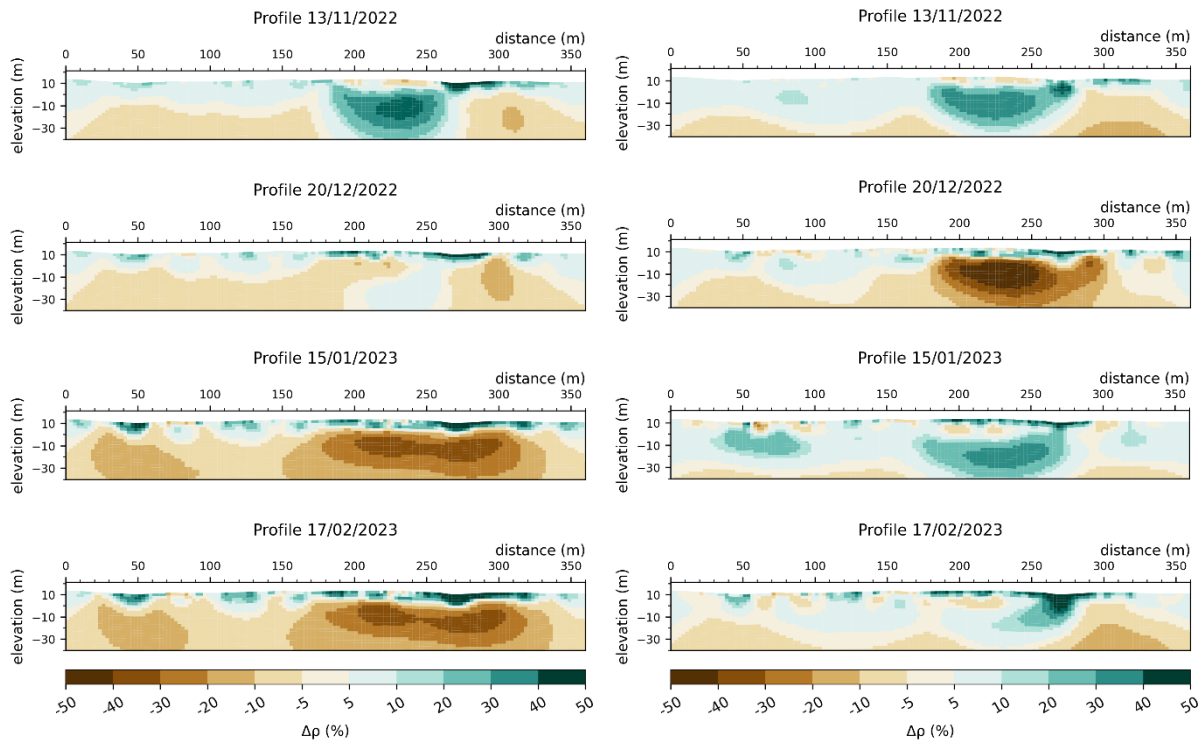


Figure 28: the time-constrained time-lapse inversions with the constant (left column) and the variable (right column) error model

The large zone of increased resistivity is observed on both time-constrained inversions with the constant and the variable error model of profiles 13/11/2022 (Fig. 28). This large zone is connected to a shallow increased resistivity zone at 260-280 m on the variable error model inversion and 260-340 m on the constant error model inversion. In the latter is the large zone also connected to a shallow zone of increased resistivity around 180 m. The shallow increased resistivity zones are larger on the constant error model inversion than on the variable error model inversion. The shallow increases and decreases of resistivity are similar in both inversions of profile 20/12/2022. On the constant error model inversion at 300 m is a zone of decreased resistivity observed. The variable error model inversion shows a zone of decreased resistivity between 180 and 300 m. The constant error model inversion of profile 15/01/2023 is very different compared with the variable error model inversion of the same day. In the latter are deeper zones with increased resistivity observed, while in the inversion with constant error model deeper zones of decreased resistivity are observed. Similar differences are observed between the inversions with the constant and variable error model of day 17/02/2023. In the inversion with the constant error model, large elongated zones of decreasing resistivity are observed. In the inversion with the variable error model is however only one zone with increased resistivity observed at depth. The shallow increased resistivity zones are similar to the inversion with the constant and variable error model of day 17/02/2023.

5.3.2 Difference inversion

The left column of figure 29 shows the difference inversions with a constant error model of the days 13/11/2022, 20/12/2022, 15/01/2023, and 17/02/2023. The change in resistivity for each day is relative to 23/10/2022, the first day of measuring. On 13/11/2022, a small increase in resistivity is observed

between 200 and 300 m. No significant changes are observed on 20/12/2022. Along profile 15/01/2023, significant increases and decreases in resistivity are observed. At 50 m, a very shallow resistivity increase is observed. While only a few meters further along the profile, a very small decrease in resistivity is visualized. Between 200 and 300 m along the profile and in the first few meters depth, a high increase in resistivity is observed. Beneath this zone, a decrease in resistivity is observed until a depth of 20 m. On 17/02/2023, a strong increase in resistivity is observed between 200 and 300 m along the profile with a maximum depth of 30 m between 250 and 300 m. A small zone of decreasing resistivity is again observed between 200 and 250 m. The difference inversions with constant error models of the days between 24/10/2022 and 27/02/2023 are visualized as a GIF ([Difference_constant_error.gif](#)).

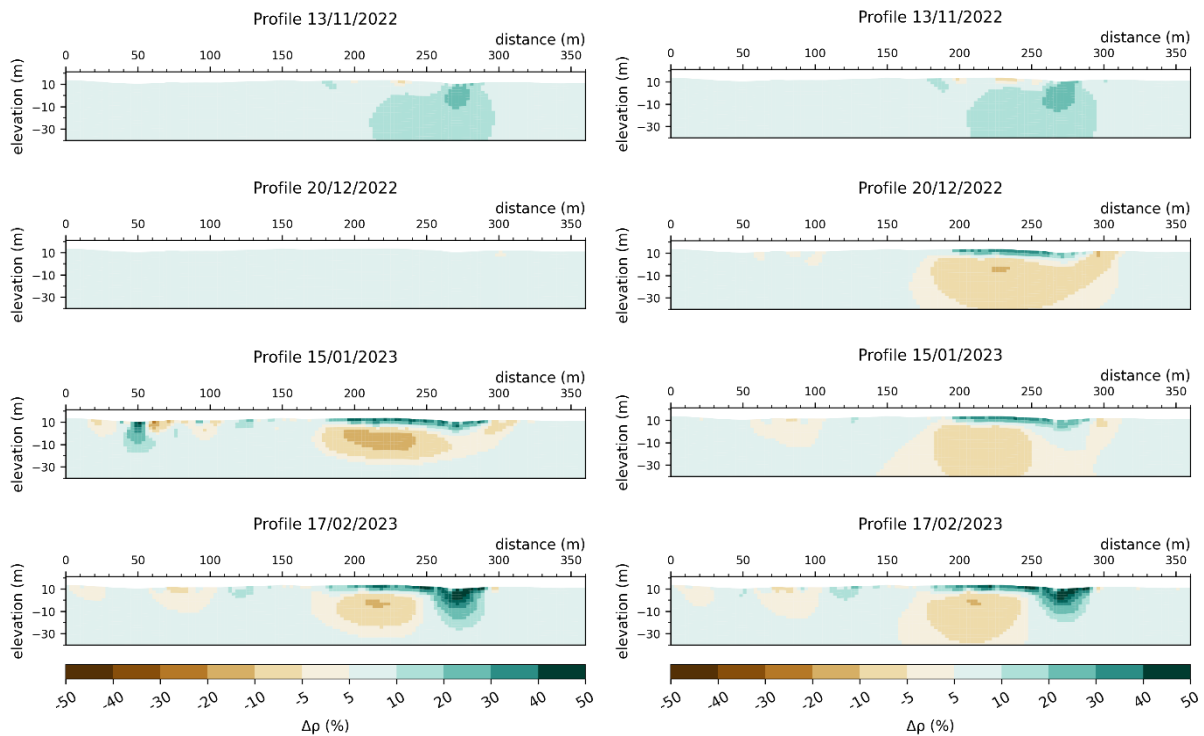


Figure 29: the difference time-lapse inversion with the constant (left column) and the variable (right column) error model

The difference inversions with the variable error model are shown in the right column of figure 29. A small increase in resistivity values is observed between 250 and 300 m along the profile collected on 13/11/2022. An increase of 10 to 20 % in resistivity is observed between 200 and 300 m with a large depth. The profile collected on 20/12/2022 shows a very shallow elongated zone of increased resistivity between 200 and 260 m. Beneath this zone, at about 0 m elevation a small zone of decreased resistivity is observed. The same shallow elongated high resistive zone is observed on profile 15/01/2023. This elongated zone is however deeper between 250 and 300 m compared with profile 20/12/2022. On profile 17/02/2023, the elongated zone observed on profiles 20/12/2022 and 15/01/2023 has even higher resistivity and deeper dimensions between 250 and 300 m. Around 50 m, 110-130 m, and 140 m small zones of increased resistivity are observed on profile 17/02/2023 and are often observed in the period between 23/10/2022 and 27/02/2023 ([Difference_variable_error.gif](#)). A small zone of decreased resistivity is observed around 210 m below the elongated increased resistivity zone.

The difference inversions with the constant and the variable error model show different results (Fig. 29). The variable error model inversion of profile 13/11/2022 shows larger zones of increasing resistivity compared with the constant error model inversion. The inversion of profile 20/12/2022 with the constant error model shows almost no variation while the inversion with the variable error model shows a significant shallow elongated zone of increased resistivity. On the inversion of profile 15/01/2023 with the variable error model is less variation observed in the first 150 m. Also, no zone with significant decreasing resistivity is observed on the inversion with the variable error model compared with the inversion with the constant error model. The variable error model inversion of profile 17/02/2023 shows a more shallow zone of increased resistivity between 260 and 290 m. The zone with decreasing resistivity is slightly smaller in the inversion with the variable error model compared with the inversion with the constant error model of profile 17/02/2023. Overall the difference inversions with the constant error model show fewer features compared with the difference inversions with the variable error model. The error level of the constant error model overestimates the daily error level used in the variable error model.

5.4 Results of temperature, soil moisture, CO₂ and precipitation data

In figure 30 the atmospheric, surface, and soil temperatures, the soil moisture, the CO₂ flux, and the precipitation data are plotted. The device measuring the CO₂ flux has a measuring limit of 20 volumetric percent. Note that the surface temperature is not for each TMS device the actual surface temperature because some devices are placed deeper in the ground (table 2). Between 01/12/2022 and 03/01/2023 the maximum of 20 vol% is constantly reached, maybe this is partly due to the snow cover on the measuring device. From 01/02/2023 onwards the CO₂ flux is very small. The amount of precipitation between 01/12/2022 and 19/01/2023 was very low. The soil moisture is depending among others on the precipitation, temperature, and soil characteristics. This signal varies the largest in TMS devices 92 and 96.

TMS devices 61 and 62 have similar trends in soil moisture, surface, and soil temperature (Fig. 30). Both devices are situated in the highest grade alteration zone with the same depth (Fig. 21). Between 15/11/2022 and 01/12/2022 the soil moisture of TMS 61 is relatively high. This matches the period of lower CO₂ flux. The soil moisture of TMS 61 decreases after the CO₂ flux increases between 31/11/2022 and 01/12/2022. Although the deep sensors of TMS 61 and 62 are the most shallow of the eight TMS devices, the highest soil temperatures are measured with these devices.

TMS 91 and 92 are located in the high grade alteration zone at a depth of respectively 15 and 12.5 cm (Fig. 6). The soil moisture signal of TMS 92 is very fluctuating (Fig. 30). Most peaks of this signal match the precipitation curve. From 31/11/2022 until 17/12/2022 the amount of precipitation is very small, while the soil moisture signal starts decreasing. During this period, the atmospheric, surface, and soil temperatures also decrease and the CO₂ flux reaches the maximum measuring limit.

TMS devices 93, 94, 95, and 96 are situated in the lowest grade alteration zone of the study area, namely in the basaltic rock (Fig. 6). The CO₂ flux measuring device is located close to TMS 94. The soil moisture increases every time positive atmospheric temperatures are reached (Fig. 30). The snow starts melting when positive atmospheric temperatures occur and water can infiltrate in the subsurface. During a period of negative atmospheric temperature, the soil moisture decreases and reaches minimum

values. The surface and soil temperatures of signals TMS 93, 95, and 96 show similar results, while TMS 94 shows a trend more similar to TMS 91. TMS device 94 is located in the basalt, but very close to an alteration zone which probably results in the observed signal.

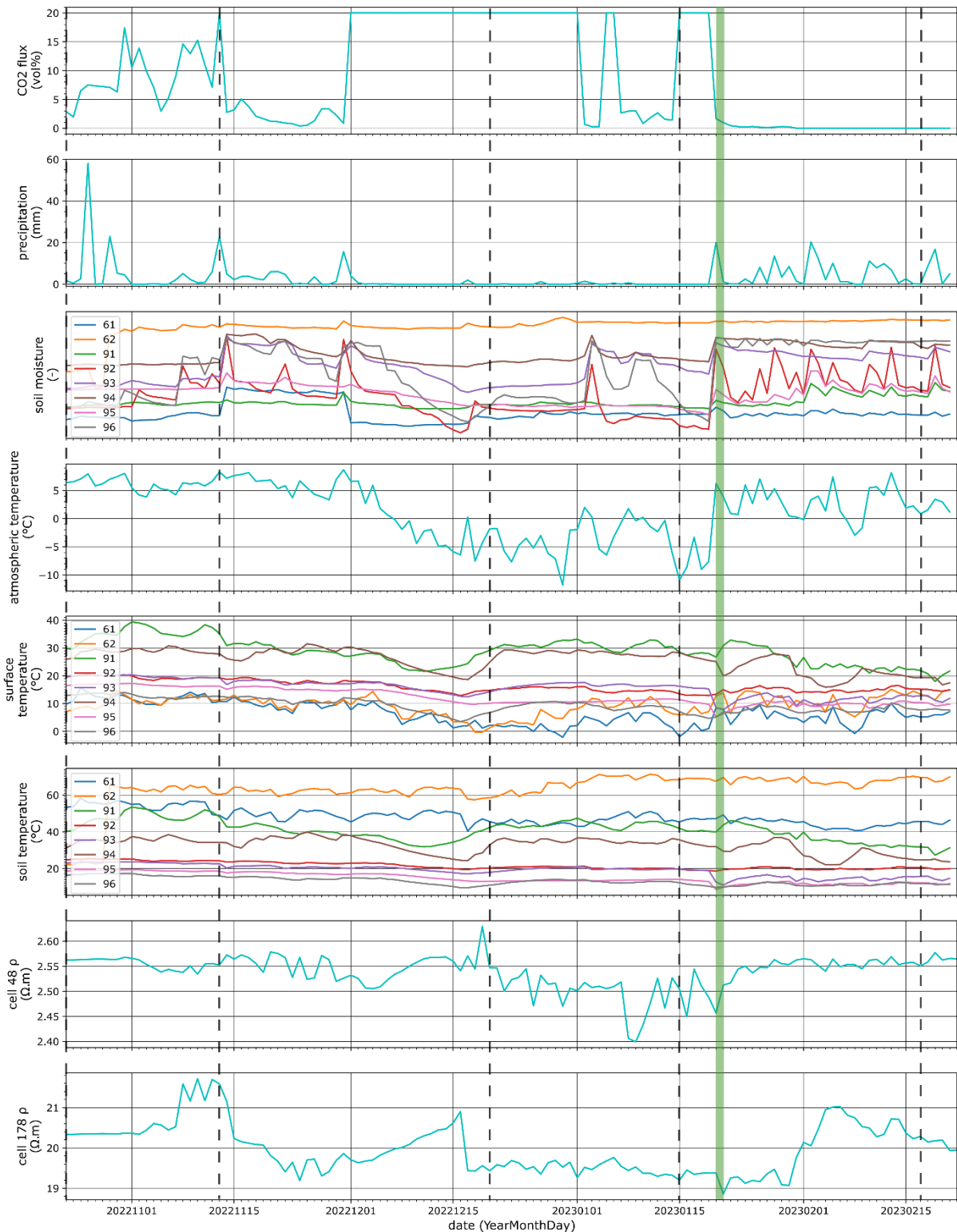


Figure 30: an overview of the CO₂ flux, precipitation, soil moisture, atmospheric temperature, surface temperature, soil temperature, resistivity at 9 m elevation at 48 m along profile 1a (cell 48 p) and resistivity at 12 m elevation at 178 m along profile 1a (cell 178 p), the dashed lines highlights the five chosen monitoring days, the green wider line highlights the two days with the drop in average resistance

No strong correlation between the resistivity of the cell closest to TMS 61 and the temperature, soil moisture, CO₂ and precipitation data is observed from the correlation matrix (Fig. 31). From the resistivity signal of the cell closest to TMS 61 is in figure 30 also no relation observed with the other data on that figure. The resistivity of the cell closest to TMS 94 appears to have an inverse signal with the surface temperature. Between the resistivity of the cell closest to TMS 94 and the temperature, soil moisture, CO₂ and precipitation data is however no strong correlation observed from the correlation matrix.

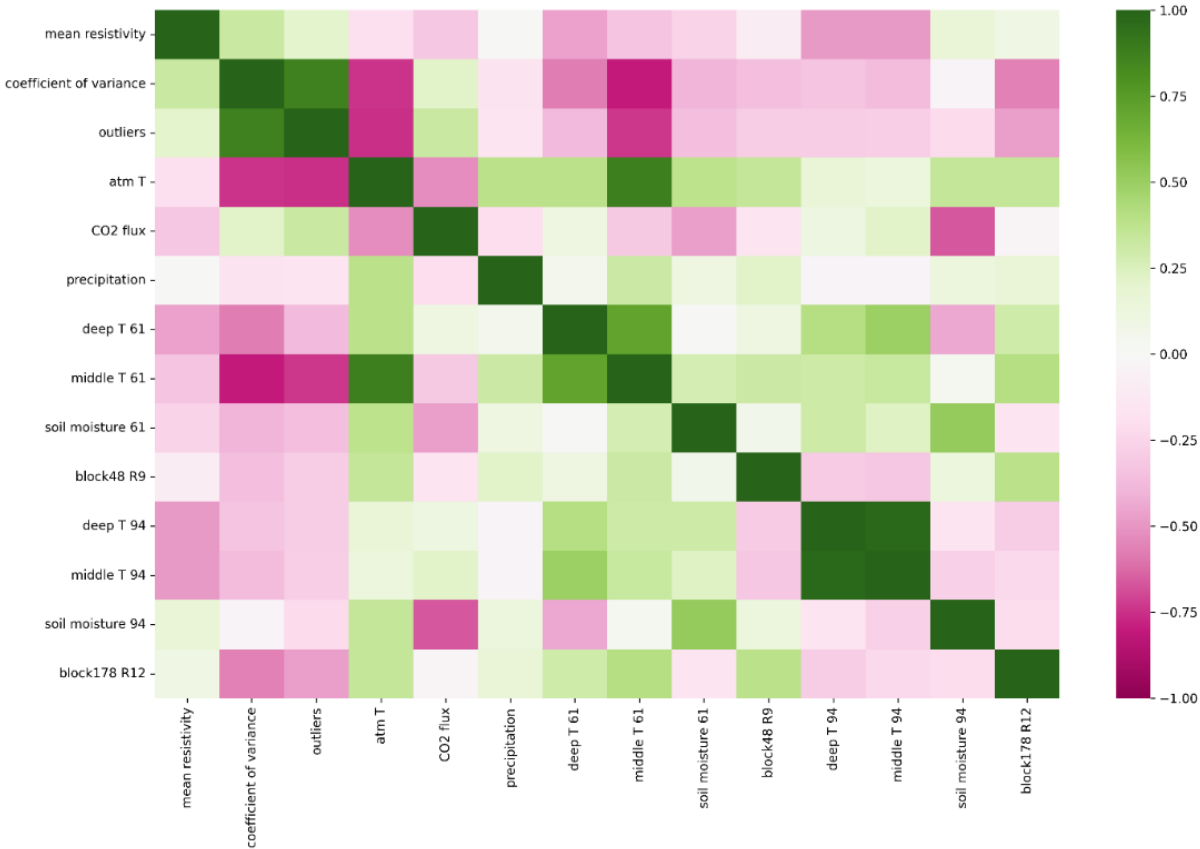


Figure 31: correlation matrix of the mean resistance (Ω), the coefficient of variance, the number of outliers (%), the average measured atmospheric temperature ($^{\circ}\text{C}$), the CO₂ flux (vol%), the precipitation in Grindavik (mm), the soil temperature at TMS 61 ($^{\circ}\text{C}$), the surface temperature at TMS 61 ($^{\circ}\text{C}$), the soil moisture at TMS 61 (-), the resistivity at 9 m elevation at 48 m along profile 1a ($\Omega.m$), the soil temperature at TMS 94 ($^{\circ}\text{C}$), the surface temperature at TMS 94 ($^{\circ}\text{C}$), the soil moisture at TMS 94 (-), the resistivity at 12 m elevation at 178 m along profile 1a ($\Omega.m$)

The mean resistance of each day varies gradually between 23/10/2022 and 22/02/2023 except between 20/01/2023 and 21/01/2023 (Fig. 24). Between these two days, a drop of 31.2% in mean resistance is observed. The time-lapse inversions of 20 and 21 January 2023 are shown to examine the differences (Fig. 32). The reference model inversion of the profile collected on the 20/01/2023 is used as a background model for the time-lapse inversions.

In the shallow subsurface of the time-constrained inversions, zones with increased resistivity are observed (Fig. 32). In the time-constrained inversion with the constant error model, two zones of decreased resistivity are observed at around 40-60 and 260-310 m. The time-constrained inversion with the variable error model shows only a decrease in resistivity around 180-330 m with the highest decrease around 275 m. A strong decrease in resistivity between 250 and 300 m is observed in the

difference inversion with the variable error model, while the difference inversion with the constant error model shows no significant changes in resistivity. The decreased resistivity zone around 270 m is observed on three out of four profiles.

A strong decrease in atmospheric temperature and precipitation is observed between 20 and 21 January 2023 (Fig. 30). The TMS closest to the 250-300 m zone is TMS 93. A small decrease in atmospheric, soil and surface temperature, soil moisture, precipitation and CO₂ flux is observed between these 2 days.

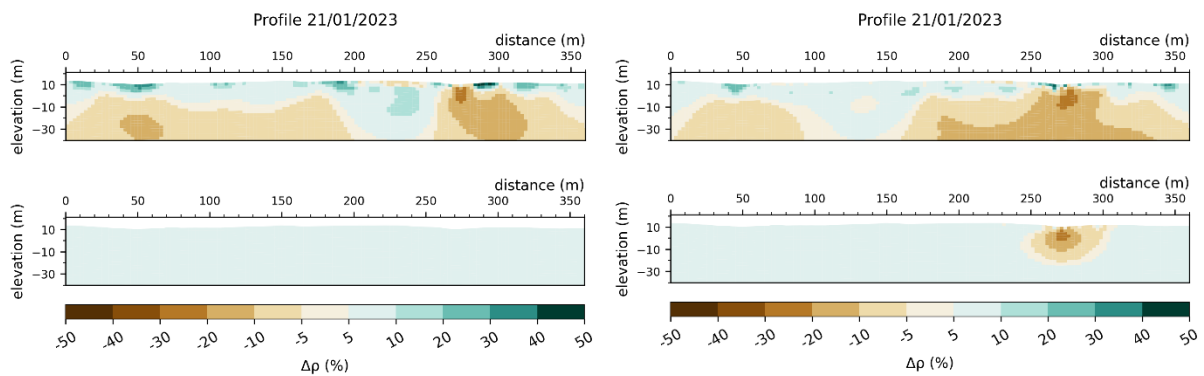


Figure 32: time-constrained (upper row) vs difference (lower row) time-lapse inversion with the constant (left column) and the variable (right column) error model

5.5 Discussion

As in the characterization study, absolute inversions with error models, and with and without a homogeneous reference model are carried out. Specific for the monitoring study, time-constrained inversions are carried out. The differences in resistivity are visualized for the reference model, time-constrained and difference inversion.

The difference inversions show probably the most realistic changes through time and are at this point the best choice to use for interpretations. This inversion method is based on the variation of the data/model instead of the absolute values. Only the strong changes are visualized with the difference inversion. Some features can be observed in both the difference inversions with the constant and variable error model (e.g. profile 13/11/2022). The features visualized in the difference inversions with the constant error model are however mostly less distinct, more smoothed and sometimes even not observable (e.g. profile 20/12/2022) compared with the difference inversions with the variable error model. The error model of the difference inversions with the constant error model is probably too conservative. Difference inversions with the variable error model have a higher amount of artefacts than with the constant error model. Still, the variable error model is reasonably conservative. The artefacts can result from the inversion method or are bad or noisy measurements. The noise has a great influence on the results and therefore the interpretation of the inversions. The noise analysis are very important to prevent artefacts resulting from the inversion method. These analysis are however reasonably difficult for long time-series.

At 50 and 120 m along the monitoring profiles, are consistently shallow zones of increased resistivity observed. These zones are also observed in the characterization study as low resistive zones. The latter are interpreted as areas with the highest grade alteration probably linked to fluid dynamics. Between

180 and 290 m along profile 1 of the characterization study, a very resistive zone is observed. In the monitoring study are zones of changing resistivity observed between 180 and 290 m. These variations in the monitoring profiles are consistent with ERT profile 1 of the characterization study. The ERT monitoring has been very likely measuring realistic changes.

A shallow increase in resistivity between 180 and 290 m is observed on the monitoring profiles. This zone corresponds to the resistive zone observed in characterization profile 1. The observed variations between 180 and 290 m on the monitoring profiles could correspond to saturation variations related to snow precipitation and colder periods. Snow accumulation results in no water infiltration. The upper part of the subsurface becomes drier. This variation should disappear once the snow melts if the snow is responsible for the observed variation. When positive atmospheric temperatures are observed after a period of negative atmospheric temperatures, the shallow zone of increased resistivity is still observed. Maybe this is due to the background profile which could be particularly conductive in this zone.

Below the shallow increased resistivity zone between 180 and 290 m, a small zone of decreasing resistivity is observed. The high resistivity of the surface can lead to a bad propagation of the injected current during the ERT measurements in the ground. For some inversion results this decreased resistivity zone is connected at zones of changing resistivity at the surface. Maybe warmer conditions at depth can cause the observed zone of decreasing resistivity. Another hypothesis can be that a cap-rock is formed at depth preventing geothermal fluids occurring at the surface. Very high chargeability values can indicate the presence of sulphides in a cap-rock. On the IP result of characterization profile 1 are however no high chargeability values observed. Note that this is still a preliminary IP result.

Between 260 and 290 m along the monitoring profiles is a deeper zone of resistivity increase observed for certain days. This zone is observed as a thinner high resistive zone on characterization profile 1. No significant changes are observed in the temperature, soil moisture, CO₂ and precipitation data on these days that may explain this deeper zone of resistivity change.

The reasoning behind the changes observed in the ERT inversion results is still unclear. If observed changes are permanent variations that enlarge with time, precipitation or alteration could be possible causes for the observed ERT signal. Fluid saturation and temperature variations could be possible reasons for the observed ERT changes that do not enlarge with time. The time-lapse inversion results show however regularly days with the same changes in resistivity. Probably fluid saturation and temperature variations are mainly responsible for the resistivity variations observed in the study area.

No strong relation is observed between the temperature, soil moisture, CO₂, precipitation data, and ERT data. The latter can not be explained solely by one or two variables such as temperature, soil moisture, or CO₂. The temperature sensors show common trends but with local anomalies caused by small-scale changes. The comparison between these local anomalies and ERT is difficult because of the difference in scales. Possibly other factors such as seasonal variation and the working of the geothermal power plant are influencing the recorded signals. Currently, chemical analysis and the sedimentological composition of the basalt and alteration zones are further investigated to calibrate the soil moisture measurements and provide knowledge about the mineralogy of the study area. Strength and strain sensors are also located in the study area which can help interpret the ERT results.

The use of another day as a background model (e.g. 27 or 28 October 2022) could result in better inversion results. The observed big variations of each day could be ruled out in the difference inversion. The resistivity values are very low in certain parts of the ERT profiles. This results in no big differences in resistivity observed in the absolute inversions when variations of 50 % occur, while in the difference inversions these variations are very clearly observable.

The Gunnuhver area is a dynamic system and it is possible to observe even daily variations in the ERT results. Consistent changes, observed in the time-lapse inversion results are proof of this dynamic system with similarities to the characterization study. A simplified schematic representation of the cross-section along the monitoring profile is shown in figure 33. The heat produced by the VHS will warm up the subsurface fluids. These fluids can migrate to the surface and warm up the ground, create mud pools, steam, or contribute to the precipitation of clays. Between 40-60 and 110-130 m along the monitoring profile the highest grade hydrothermal alteration zones are observed probably created and maintained by up-flow of hydrothermal fluids. The lowest grade alteration of the high resistive basaltic rock is located between 180 and 300 m along the monitoring profile. Hydrothermal fluids are probably not ascending to the surface because among others, no surface manifestations were observed. These fluids could possibly be stopped by a cap-rock formed at depth. Around 270 m strong changes are observed on the difference inversion results which indicate varying conditions probably related to temperatures and fluid saturation variations. At shallow depth, hot saline groundwater is expected flowing in the direction of the Grey Lagoon.

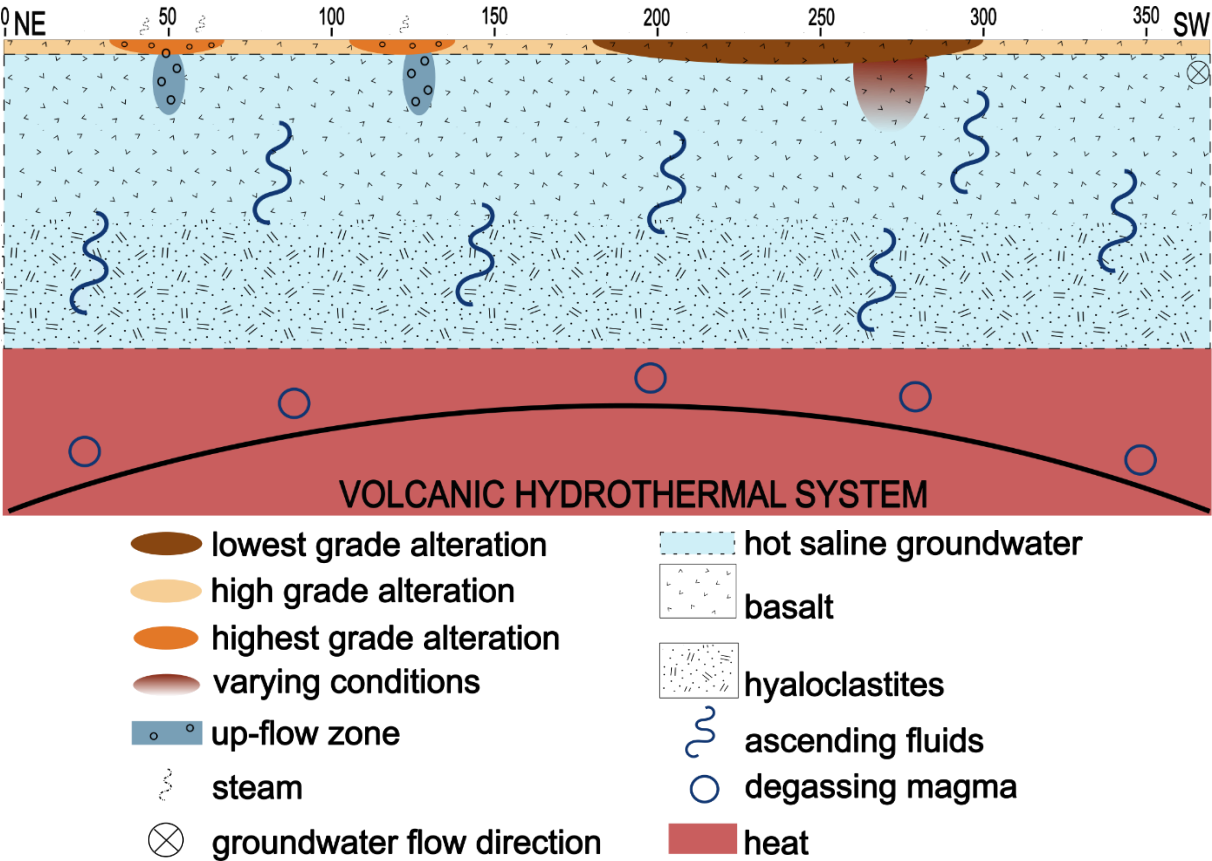


Figure 33: cross-section with interpretation of monitoring profile (not to scale)

6 Conclusion and future recommendations

During the field campaign between 29 August and 7 September 2022, ERT, SP, and IP data were collected along five profiles to characterize the Gunnuhver area. The ERT data is processed with absolute inversions using three types of error models with or without a reference model. All three types of error models show similar results in the shallow subsurface of the reference model inversion results and could be used to make qualitative interpretations. The individual error is however most likely too optimistic for this characterization study. The self-defined maximum of iterations is always reached and small artefacts are observed in the inversion results. More delineated structures are observed in the results of the reference model inversions with the variable error model. The results of this inversion type are hence used to characterize the study area.

Low resistive zones are observed on the ERT inversion results and correspond to shallow high grade alteration zones probably linked to fluid dynamics. In these hydrothermal alteration zones, warm grounds, mud pools and precipitation of clays occur. Lateral variations are also observed in resistive and conductive zones. These lateral variations are however more difficult to interpret. High resistive zones observed on the ERT inversions correspond to less altered zones and consist of basaltic rocks. The very low resistivity observed at depth on the ERT inversion results corresponds most likely with the hot saline groundwater.

The closure correction (Revil & Jardani, 2013) could not be implemented on the measured SP signals because of the measurement configuration. Low and stable SP results are observed in more resistive zones possibly due to downward flow or chemical reactions between volcanic gases (H_2S , SO_2 , CO_2) and groundwater (Grobbe & Barde-Cabusson, 2019; Zlotnicki & Nishida, 2003). Positive SP anomalies are coinciding with active and altered zones as probably the result of the up-flow of hydrothermal fluids (Grobbe & Barde-Cabusson, 2019).

Since 23 October 2022, daily ERT/IP measurements are carried out to monitor the volcanic hydrothermal system of Gunnuhver. Using the knowledge obtained from the characterization study, advanced inversion techniques for time-lapse ERT are investigated. Absolute inversions with the constant and the variable error model and with and without a homogeneous reference model are carried out. Further, the time-constrained and the difference time-lapse inversions are carried out with the constant and variable linear error model. The changes in resistivity are visualized for the reference model, the time-constrained, and the difference inversions.

The difference inversion results show probably the most realistic changes through time and are used for interpretations. The difference inversions with the constant error model are probably too conservative because of the less distinct, more smoothed and sometimes not observable features. The variable linear error model is also still a conservative model, which is probably not sufficient providing the best inversion results for this study. The time-lapse inversions can be optimized by further analysing the closeness factor of the reference model and the choice of the day used as the background model. Inversion results are sensitive to the noise level, definitely in terms of quantitative interpretations. The noise analysis are very important to minimize inversion artefacts, but can be challenging for long time-series. The error model can be further improved based on the methodology of Lesparre et al. (2017) which is specific for time-lapse data. Independent data could be collected to validate the inversion results, to decide which

inversion models are more realistic and to determine more realistic parameters to use during the inversion. More advanced time-lapse ERT inversion techniques could also be carried out (e.g. Karaoulis et al., 2014).

The ERT monitoring has been very likely measuring realistic changes. Consistent changes in resistivity in the shallow zones at 50 and 120 m are observed which match the low resistive zones of characterization profile 1. These zones are located in areas with the highest grade alteration probably linked to fluid dynamics. Installing deep sensors in these alteration areas could provide clarification. Between 180 and 290 m along characterization profile 1, a very resistive zone is observed which matches the changes in resistivity of the monitoring profiles. The most shallow part of this zone could correspond to saturation variations related to snow precipitation and colder periods. Beneath this zone, different changes in resistivity are observed. The high resistivity of the surface can lead to a bad propagation of the injected current during the ERT measurements in the ground. Maybe warmer conditions at depth can cause the observed zone of resistivity. Another hypothesis is the formation of a cap-rock at depth preventing the transport of geothermal fluids to the surface.

The causes of the observed changes in the ERT inversions are not yet clear. Probably fluid saturation and temperature variations could be partially the driving forces because of the constant changes in resistivity with time. The enlargement of ERT variations with time could be caused by precipitation or alteration. In the period between 23/10/2022 and 27/02/2023 no enlargement of ERT variations is however observed.

The temperature, soil moisture and CO₂ data show local anomalies caused by small-scale changes which can not be observed on the ERT results. Seasonal variations and the working of the geothermal power plant are examples of other factors probably influencing the recorded ERT signal.

The monitoring of the active geothermal area could be improved by including self-potential monitoring (Arens et al., 2022; Revil et al., 2023). The temperature, soil moisture, CO₂, and precipitation data can be investigated in more detail with for example moving window statistics. Time-series analysis of the ERT data could be carried out by classifying which type of cells have the same type of trend. The use of another day as a background model (e.g. 27 or 28 October 2022) could result in better inversion results. Apart from the ongoing investigation in the ERupT project, remote sensing could be used to monitor the geothermal activity in the study area (e.g. Óladóttir, 2012). Also, a shallow well could be installed to determine the depth, the chemical composition, the pH and the temperature of the groundwater and perform electromagnetic logging to validate the ERT results.

It can be concluded from the characterization and monitoring study that the Gunnuhver area is a dynamic system. Daily variations are observed in the ERT time-lapse inversions. Basaltic rocks with the lowest grade alteration represent the largest part of the study area. High grade alteration zones are located in the NW and SW of the study area with three zones where the highest grade of hydrothermal alteration occurs probably linked to fluid dynamics. At shallow depth, a very low resistive zone is observed most likely representing the hot saline groundwater. A lot more research should be carried out to reveal the dynamic behaviour of the volcanic hydrothermal system of Gunnuhver in more detail.

Bibliography

- Antelman, M. S. (1989). *The Encyclopedia of Chemical Electrode Potentials*. Plenum Press.
- Archie, G. E. (1942). The Electrical Resistivity Log as an Aid in Determining Some Reservoir Characteristics. *Transactions of the AIME*, 146(01), 54–62. <https://doi.org/10.2118/942054-G>
- Arens, F., Coco, A., Gottsmann, J., Hickey, J., & Kilgour, G. (2022). Multiphysics Modeling of Volcanic Unrest at Mt. Ruapehu (New Zealand). *Geochemistry, Geophysics, Geosystems*, 23(12). <https://doi.org/10.1029/2022GC010572>
- Arens, F., Gottsmann, J., Strehlow, K., Hickey, J., & Kilgour, G. (2020). Electrokinetic Contributions to Self-Potential Signals From Magmatic Stressing. *Geochemistry, Geophysics, Geosystems*, 21(12). <https://doi.org/10.1029/2020GC009388>
- Atekwana, E. A., Sauck, W. A., & Werkema, D. D. (2000). Investigations of geoelectrical signatures at a hydrocarbon contaminated site. *Journal of Applied Geophysics*, 44(2–3), 167–180. [https://doi.org/10.1016/S0926-9851\(98\)00033-0](https://doi.org/10.1016/S0926-9851(98)00033-0)
- Barde-Cabusson, S., Gottsmann, J., Martí, J., Bolós, X., Camacho, A. G., Geyer, A., Planagumà, L., Ronchin, E., & Sánchez, A. (2014). Structural control of monogenetic volcanism in the Garrotxa volcanic field (Northeastern Spain) from gravity and self-potential measurements. *Bulletin of Volcanology*, 76(1), 1–13. <https://doi.org/10.1007/s00445-013-0788-0>
- Barde-Cabusson, S., Levieux, G., Lénat, J. F., Finizola, A., Revil, A., Chaput, M., Dumont, S., Duputel, Z., Guy, A., Mathieu, L., Saumet, S., Sorbadère, F., & Vieille, M. (2009). Transient self-potential anomalies associated with recent lava flows at Piton de la Fournaise volcano (Réunion Island, Indian Ocean). *Journal of Volcanology and Geothermal Research*, 187(3–4), 158–166. <https://doi.org/10.1016/j.jvolgeores.2009.09.003>
- Battaglia, J., Métaixian, J. P., & Garaebiti, E. (2016). Short term precursors of Strombolian explosions at Yasur volcano (Vanuatu). *Geophysical Research Letters*, 43(5), 1960–1965. <https://doi.org/10.1002/2016GL067823>
- Benoit, S., Ghysels, G., Gommers, K., Hermans, T., Nguyen, F., & Huysmans, M. (2019). Characterization of spatially variable riverbed hydraulic conductivity using electrical resistivity tomography and induced polarization. *Hydrogeology Journal*, 27(1), 395–407. <https://doi.org/10.1007/s10040-018-1862-7>
- Binley, A., Winship, P., West, L. J., Pokar, M., & Middleton, R. (2002). Seasonal variation of moisture content in unsaturated sandstone inferred from borehole radar and resistivity profiles. *Journal of Hydrology*, 267(3–4), 160–172. [https://doi.org/10.1016/S0022-1694\(02\)00147-6](https://doi.org/10.1016/S0022-1694(02)00147-6)
- Burton, M., Hayer, C., Miller, C., & Christenson, B. (2021). Insights into the 9 December 2019 eruption of Whakaari/White Island from analysis of TROPOMI SO₂ imagery. *Science Advances*, 7(25). <https://doi.org/10.1126/sciadv.abg1218>
- Caterina, D., Beaujean, J., Robert, T., & Nguyen, F. (2013). A comparison study of different image appraisal tools for electrical resistivity tomography. *Near Surface Geophysics*, 11(6), 639–657. <https://doi.org/10.3997/1873-0604.2013022>

- Caudron, C., Girona, T., Taisne, B., Suparjan, Gunawan, H., Kristianto, & Kasbani. (2019). Change in seismic attenuation as a long-term precursor of gas-driven eruptions. *Geology*, *47*(7), 632–636. <https://doi.org/10.1130/G46107.1>
- Caudron, C., Girona, T., Lecocq, T., Ardid, A., Dempsey, D., and Yates, A.: *Towards monitoring phreatic eruptions using seismic noise*, EGU General Assembly 2023, Vienna, Austria, 24–28 Apr 2023, EGU23-7166, <https://doi.org/10.5194/egusphere-egu23-7166>, 2023.
- Chambers, J. E., Gunn, D. A., Wilkinson, P. B., Meldrum, P. I., Haslam, E., Holyoake, S., Kirkham, M., Kuras, O., Merritt, A., & Wragg, J. (2014). 4D electrical resistivity tomography monitoring of soil moisture dynamics in an operational railway embankment. *Near Surface Geophysics*, *12*(1), 61–72. <https://doi.org/10.3997/1873-0604.2013002>
- Chouet, B. A., & Matoza, R. S. (2013). A multi-decadal view of seismic methods for detecting precursors of magma movement and eruption. In *Journal of Volcanology and Geothermal Research* (Vol. 252, pp. 108–175). <https://doi.org/10.1016/j.jvolgeores.2012.11.013>
- Christenson, B. W., Reyes, A. G., Young, R., Moebis, A., Sherburn, S., Cole-Baker, J., & Britten, K. (2010). Cyclic processes and factors leading to phreatic eruption events: Insights from the 25 September 2007 eruption through Ruapehu Crater Lake, New Zealand. *Journal of Volcanology and Geothermal Research*, *191*(1–2), 15–32. <https://doi.org/10.1016/j.jvolgeores.2010.01.008>
- Ciraula, D. A., Carr, B. J., & Sims, K. W. W. (2023a). Geophysical Imaging of the Shallow Geyser and Hydrothermal Reservoir Structures of Spouter Geyser, Yellowstone National Park: Geyser Dynamics I. *Journal of Geophysical Research: Solid Earth*, *128*(2). <https://doi.org/10.1029/2022JB024417>
- Ciraula, D. A., Carr, B. J., & Sims, K. W. W. (2023b). Time-Lapse Geophysical Investigation of Geyser Dynamics at Spouter Geyser, Yellowstone National Park: Geyser Dynamics II. *Journal of Geophysical Research: Solid Earth*, *128*(2). <https://doi.org/10.1029/2022JB024426>
- Clifton, A. E., & Schlische, R. W. (2003). Fracture populations on the Reykjanes Peninsula, Iceland: Comparison with experimental clay models of oblique rifting. *Journal of Geophysical Research: Solid Earth*, *108*(B2). <https://doi.org/10.1029/2001jb000635>
- Dahlin, T., & Zhou, B. (2004). A numerical comparison of 2D resistivity imaging with 10 electrode arrays. In *Geophysical Prospecting* (Vol. 52).
- Dahlin, T., & Zhou, B. (2006). Multiple-gradient array measurements for multichannel 2D resistivity imaging. In *Near Surface Geophysics*.
- Deceuster, J., Etienne, A., Robert, T., Nguyen, F., & Kaufmann, O. (2014). A modified DOI-based method to statistically estimate the depth of investigation of dc resistivity surveys. *Journal of Applied Geophysics*, *103*, 172–185. <https://doi.org/10.1016/j.jappgeo.2014.01.018>
- Dekoninck, W. (2023). *Advanced data quality assessment of time dependent induced polarization data: A case study on the volcanic hydrothermal system in Reykjanes (Iceland)*. Department of Geology, Ghent University [unpublished Master's dissertation]
- Di Giuseppe, M. G., & Troiano, A. (2019). Monitoring active fumaroles through time-lapse electrical resistivity tomograms: an application to the Pisciarelli fumarolic field (Campi Flegrei, Italy).

- Journal of Volcanology and Geothermal Research*, 375, 32–42.
<https://doi.org/10.1016/j.jvolgeores.2019.03.009>
- Dimech, A., Cheng, L. Z., Chouteau, M., Chambers, J., Uhlemann, S., Wilkinson, P., Meldrum, P., Mary, B., Fabien-Ouellet, G., & Isabelle, A. (2022). A Review on Applications of Time-Lapse Electrical Resistivity Tomography Over the Last 30 Years : Perspectives for Mining Waste Monitoring. In *Surveys in Geophysics*. Springer Science and Business Media B.V.
<https://doi.org/10.1007/s10712-022-09731-2>
- Dumont, G., Pilawski, T., Dzaomuhó-Lenieregue, P., Hilgsmann, S., Delvigne, F., Thonart, P., Robert, T., Nguyen, F., & Hermans, T. (2016). Gravimetric water distribution assessment from geoelectrical methods (ERT and EMI) in municipal solid waste landfill. *Waste Management*, 55, 129–140. <https://doi.org/10.1016/j.wasman.2016.02.013>
- Einarsson, M. Á. (1984). Climate of iceland. In H. van Loon (Ed.), *World survey of climatology* (Vol. 15, pp. 673–697). Elsevier.
- Eiríksson, J., & Simonarson, L. A. (2021). *A Brief Resumé of the Geology of Iceland* (pp. 1–11). https://doi.org/10.1007/978-3-030-59663-7_1
- Finizola, A., Sortino, F., Lénat, J.-F., & Valenza, M. (2002). Fluid circulation at Stromboli volcano (Aeolian Islands, Italy) from self-potential and CO₂ surveys. *Journal of Volcanology and Geothermal Research*, 116(1–2), 1–18. [https://doi.org/10.1016/S0377-0273\(01\)00327-4](https://doi.org/10.1016/S0377-0273(01)00327-4)
- Fridriksson, T., Kristjánsson, B. R., Ármannsson, H., Margrétardóttir, E., Ólafsdóttir, S., & Chiodini, G. (2006). CO₂ emissions and heat flow through soil, fumaroles, and steam heated mud pools at the Reykjanes geothermal area, SW Iceland. *Applied Geochemistry*, 21(9), 1551–1569. <https://doi.org/10.1016/j.apgeochem.2006.04.006>
- Fridriksson, T., Padrón, E., Óskarsson, F., & Pérez, N. M. (2016). Application of diffuse gas flux measurements and soil gas analysis to geothermal exploration and environmental monitoring: Example from the Reykjanes geothermal field, SW Iceland. *Renewable Energy*, 86, 1295–1307. <https://doi.org/10.1016/j.renene.2015.09.034>
- Grobbe, N., & Barde-Cabusson, S. (2019). Self-Potential Studies in Volcanic Environments: A Cheap and Efficient Method for Multiscale Fluid-Flow Investigations. *International Journal of Geophysics*, 2019. <https://doi.org/10.1155/2019/2985824>
- Grobbe, N., Mordret, A., Barde-Cabusson, S., Ellison, L., Lach, M., Seo, Y. H., Viti, T., Ward, L., & Zhang, H. (2021). A Multi-Hydrogeophysical Study of a Watershed at Kaiwi Coast (O‘ahu, Hawai‘i), using Seismic Ambient Noise Surface Wave Tomography and Self-Potential Data. *Water Resources Research*, 57(4). <https://doi.org/10.1029/2020WR029057>
- Ha, H. S., Kim, D. S., & Park, I. J. (2010). Application of electrical resistivity techniques to detect weak and fracture zones during underground construction. *Environmental Earth Sciences*, 60(4), 723–731. <https://doi.org/10.1007/s12665-009-0210-6>
- Hayley, K., Bentley, L. R., Gharibi, M., & Nightingale, M. (2007). Low temperature dependence of electrical resistivity: Implications for near surface geophysical monitoring. *Geophysical Research Letters*, 34(18). <https://doi.org/10.1029/2007GL031124>

- Hermans, T. (2014). *Integration of near-surface geophysical, geological and hydrogeological data with multiple-point geostatistics in alluvial aquifers*. University of Liege.
- Hermans, T., Nguyen, F., Robert, T., & Revil, A. (2014). Geophysical methods for monitoring temperature changes in shallow low enthalpy geothermal systems. In *Energies* (Vol. 7, Issue 8, pp. 5083–5118). MDPI AG. <https://doi.org/10.3390/en7085083>
- Hermans, T., Vandenbohede, A., Lebbe, L., Martin, R., Kemna, A., Beaujean, J., & Nguyen, F. (2012a). Imaging artificial salt water infiltration using electrical resistivity tomography constrained by geostatistical data. *Journal of Hydrology*, *438–439*, 168–180. <https://doi.org/10.1016/j.jhydrol.2012.03.021>
- Hermans, T., Vandenbohede, A., Lebbe, L., Martin, R., Kemna, A., Beaujean, J., & Nguyen, F. (2012b). Imaging artificial salt water infiltration using electrical resistivity tomography constrained by geostatistical data. *Journal of Hydrology*, *438–439*, 168–180. <https://doi.org/10.1016/j.jhydrol.2012.03.021>
- Isaia, R., Di Giuseppe, M. G., Natale, J., Tramparulo, F. D. A., Troiano, A., & Vitale, S. (2021). Volcano-Tectonic Setting of the Pisciarelli Fumarole Field, Campi Flegrei Caldera, Southern Italy: Insights Into Fluid Circulation Patterns and Hazard Scenarios. *Tectonics*, *40*(5). <https://doi.org/10.1029/2020TC006227>
- Jardani, A., Revil, A., Santos, F., Fauchard, C., & Dupont, J. P. (2007). Detection of preferential infiltration pathways in sinkholes using joint inversion of self-potential and EM-34 conductivity data. *Geophysical Prospecting*, *55*(5), 749–760. <https://doi.org/10.1111/j.1365-2478.2007.00638.x>
- Karaoulis, M., Tsourlos, P., Kim, J. H., & Revill, A. (2014). 4D time-lapse ERT inversion: Introducing combined time and space constraints. *Near Surface Geophysics*, *12*(1), 25–34. <https://doi.org/10.3997/1873-0604.2013004>
- Kawakatsu, H., Kaneshima, S., Matsubayashi, H., Ohminato, T., Sudo, Y., Tsutsui, T., Uhira, K., Yamasato, H., Ito, H., & Legrand, D. (2000). Aso94: Aso seismic observation with broadband instruments. *Journal of Volcanology and Geothermal Research*, *101*(1–2), 129–154. [https://doi.org/10.1016/S0377-0273\(00\)00166-9](https://doi.org/10.1016/S0377-0273(00)00166-9)
- Kemna, A. (2000). *Tomographic Inversion of Complex Resistivity: Theory and Application*. Institutes für Geophysik der Ruhr-Universität Bochum.
- Koestel, J., Kemna, A., Javaux, M., Binley, A., & Vereecken, H. (2008). Quantitative imaging of solute transport in an unsaturated and undisturbed soil monolith with 3-D ERT and TDR. *Water Resources Research*, *44*(12). <https://doi.org/10.1029/2007WR006755>
- LaBrecque, D. J., Miletto, M., Daily, W., Ramirez, A., & Owen, E. (1996). The effects of noise on Occam's inversion of resistivity tomography data. *GEOPHYSICS*, *61*(2), 538–548. <https://doi.org/10.1190/1.1443980>
- LaBrecque, D. J., & Yang, X. (2001). Difference Inversion of ERT Data: a Fast Inversion Method for 3-D In Situ Monitoring. *Journal of Environmental and Engineering Geophysics*, *6*(2), 83–89. <https://doi.org/10.4133/JEEG6.2.83>

- Lapenna, V., Lorenzo, P., Perrone, A., Piscitelli, S., Rizzo, E., & Sdao, F. (2005). 2D electrical resistivity imaging of some complex landslides in Lucanian Apennine chain, southern Italy. *GEOPHYSICS*, *70*(3), B11–B18. <https://doi.org/10.1190/1.1926571>
- Lesparre, N., Nguyen, F., Kemna, A., Robert, T., Hermans, T., Daoudi, M., & Flores-Orozco, A. (2017). A new approach for time-lapse data weighting in electrical resistivity tomography. *Geophysics*, *82*(6), E325–E333. <https://doi.org/10.1190/GEO2017-0024.1>
- Lévy, L., Maurya, P. K., Byrdina, S., Vandemeulebrouck, J., Sigmundsson, F., Árnason, K., Ricci, T., Deldicque, D., Roger, M., Gibert, B., & Labazuy, P. (2019). Electrical resistivity tomography and time-domain induced polarization field investigations of geothermal areas at Krafla, Iceland: Comparison to borehole and laboratory frequency-domain electrical observations. *Geophysical Journal International*, *218*(3), 1469–1489. <https://doi.org/10.1093/gji/ggz240>
- Linde, N., Renard, P., Mukerji, T., & Caers, J. (2015). Geological realism in hydrogeological and geophysical inverse modeling: A review. *Advances in Water Resources*, *86*, 86–101. <https://doi.org/10.1016/j.advwatres.2015.09.019>
- Loke, M. H., Chambers, J. E., Rucker, D. F., Kuras, O., & Wilkinson, P. B. (2013). Recent developments in the direct-current geoelectrical imaging method. *Journal of Applied Geophysics*, *95*, 135–156. <https://doi.org/10.1016/j.jappgeo.2013.02.017>
- Lowrie, W. (2007). *Fundamentals of Geophysics*. Cambridge University Press. <https://doi.org/10.1017/CBO9780511807107>
- Marescot, L., Loke, M. H., Chapellier, D., Delaloye, R., Lambiel, C., & Reynard, E. (2003). Assessing reliability of 2D resistivity imaging in mountain permafrost studies using the depth of investigation index method. *Near Surface Geophysics*, *1*(2), 57–67. <https://doi.org/10.3997/1873-0604.2002007>
- Marks, N., Schiffman, P., Zierenberg, R. A., Franzson, H., & Fridleifsson, G. Ó. (2010). Hydrothermal alteration in the Reykjanes geothermal system: Insights from Iceland deep drilling program well RN-17. *Journal of Volcanology and Geothermal Research*, *189*(1–2), 172–190. <https://doi.org/10.1016/j.jvolgeores.2009.10.018>
- Marteinsson, K., Sigurgeirsson, M. Á., Sigurðarson, D., & Þorbjörnsson, D. (2022). *Sandvík-Eldisgarðar Grunnvatnslíkan Unnið fyrir Samherja fiskeldi ehf.* www.isor.is [in Icelandic]
- Miller, C. R., Routh, P. S., Brosten, T. R., & McNamara, J. P. (2008). Application of time-lapse ERT imaging to watershed characterization. *Geophysics*, *73*(3). <https://doi.org/10.1190/1.2907156>
- Mollaret, C., Hilbich, C., Pellet, C., Flores-Orozco, A., Delaloye, R., & Hauck, C. (2019). Mountain permafrost degradation documented through a network of permanent electrical resistivity tomography sites. *Cryosphere*, *13*(10), 2557–2578. <https://doi.org/10.5194/tc-13-2557-2019>
- Naudet, V., Revil, A., Rizzo, E., Bottero, J.-Y., & Bégassat, P. (2004). Groundwater redox conditions and conductivity in a contaminant plume from geoelectrical investigations. *Hydrology and Earth System Sciences*, *8*(1), 8–22. <https://doi.org/10.5194/hess-8-8-2004>
- Nguyen, F., Kemna, A., Antonsson, A., Engesgaard, P., Kuras, O., Ogilvy, R., Gisbert, J., Jorreto, S., & Pulido-Bosch, A. (2009). Characterization of seawater intrusion using 2D electrical imaging. *Near Surface Geophysics*, *7*(5–6), 377–390. <https://doi.org/10.3997/1873-0604.2009025>

- Óladóttir, A. A. (2012). *Application of soil measurements and remote sensing for monitoring changes in geothermal surface activity in the Reykjanes field, Iceland*. University of Iceland.
- Oldenburg, D. W., & Li, Y. (1999). Estimating depth of investigation in dc resistivity and IP surveys. *GEOPHYSICS*, *64*(2), 403–416. <https://doi.org/10.1190/1.1444545>
- Onsager, L. (1931). Reciprocal Relations in Irreversible Processes. I. *Physical Review*, *37*(4), 405–426. <https://doi.org/10.1103/PhysRev.37.405>
- Parasnis, D. S. (1988). Reciprocity theorems in geoelectric and geoelectromagnetic work. *Geoexploration*, *25*(3), 177–198. [https://doi.org/10.1016/0016-7142\(88\)90014-2](https://doi.org/10.1016/0016-7142(88)90014-2)
- Pardo, N., Cronin, S. J., Németh, K., Brenna, M., Schipper, C. I., Breard, E., White, J. D. L., Procter, J., Stewart, B., Agustín-Flores, J., Moebis, A., Zernack, A., Kereszturi, G., Lube, G., Auer, A., Neall, V., & Wallace, C. (2014). Perils in distinguishing phreatic from phreatomagmatic ash; insights into the eruption mechanisms of the 6 August 2012 Mt. Tongariro eruption, New Zealand. *Journal of Volcanology and Geothermal Research*, *286*, 397–414. <https://doi.org/10.1016/j.jvolgeores.2014.05.001>
- Peacock, J. R., & Siler, D. L. (2021). Bottom-Up and Top-Down Control on Hydrothermal Resources in the Great Basin: An Example From Gabbs Valley, Nevada. *Geophysical Research Letters*, *48*(23). <https://doi.org/10.1029/2021GL095009>
- Ramirez, A., Daily, W., LaBrecque, D., Owen, E., & Chesnut, D. (1993). Monitoring an underground steam injection process using electrical resistance tomography. *Water Resources Research*, *29*(1), 73–87. <https://doi.org/10.1029/92WR01608>
- Revil, A., Coperey, A., Shao, Z., Florsch, N., Fabricius, I. L., Deng, Y., Delsman, J. R., Pauw, P. S., Karaoulis, M., de Louw, P. G. B., van Baaren, E. S., Dabekaussen, W., Menkovic, A., & Gunnink, J. L. (2017). Complex conductivity of soils. *Water Resources Research*, *53*(8), 7121–7147. <https://doi.org/10.1002/2017WR020655>
- Revil, A., Finizola, A., & Gresse, M. (2023). Self-potential as a tool to assess groundwater flow in hydrothermal systems: A review. *Journal of Volcanology and Geothermal Research*, 107788. <https://doi.org/10.1016/j.jvolgeores.2023.107788>
- Revil, A., Finizola, A., Piscitelli, S., Rizzo, E., Ricci, T., Crespy, A., Angeletti, B., Balasco, M., Cabusson Barde, S., Bennati, L., Bolève, A., Byrdina, S., Carzaniga, N., Di Gangi, F., Morin, J., Perrone, A., Rossi, M., Roulleau, E., & Suski, B. (2008). Inner structure of La Fossa di Vulcano (Vulcano Island, southern Tyrrhenian Sea, Italy) revealed by high-resolution electric resistivity tomography coupled with self-potential, temperature, and CO₂ diffuse degassing measurements. *Journal of Geophysical Research: Solid Earth*, *113*(7). <https://doi.org/10.1029/2007JB005394>
- Revil, A., Finizola, A., Sortino, F., & Ripepe, M. (2004). Geophysical investigations at Stromboli volcano, Italy: Implications for ground water flow and paroxysmal activity. *Geophysical Journal International*, *157*(1), 426–440. <https://doi.org/10.1111/j.1365-246X.2004.02181.x>
- Revil, A., Florsch, N., & Mao, D. (2015). Induced polarization response of porous media with metallic particles -Part 1: A theory for disseminated semiconductors. *Geophysics*, *80*(5), D525–D538. <https://doi.org/10.1190/GEO2014-0577.1>

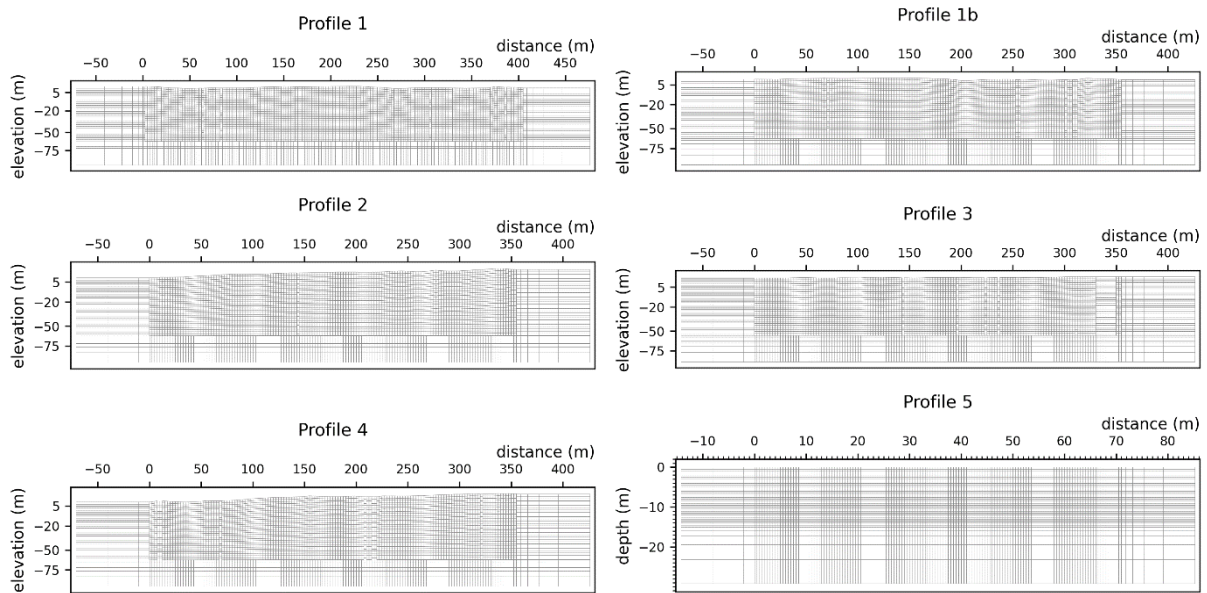
- Revil, A., & Jardani, A. (2013). *The Self-Potential Method: Theory and Applications in Environmental Geosciences*. Cambridge University Press.
- Revil, A., Karaoulis, M., Johnson, T., & Kemna, A. (2012). Review: Some low-frequency electrical methods for subsurface characterization and monitoring in hydrogeology. *Hydrogeology Journal*, 20(4), 617–658. <https://doi.org/10.1007/s10040-011-0819-x>
- Revil, A., Le Breton, M., Niu, Q., Wallin, E., Haskins, E., & Thomas, D. M. (2017). Induced polarization of volcanic rocks. 2. Influence of pore size and permeability. *Geophysical Journal International*, 208(2), 814–825. <https://doi.org/10.1093/gji/ggw382>
- Revil, A., Qi, Y., Ghorbani, A., Coperey, A., Ahmed, A. S., Finizola, A., & Ricci, T. (2019). Induced polarization of volcanic rocks. 3. Imaging clay cap properties in geothermal fields. *Geophysical Journal International*, 218(2), 1398–1427. <https://doi.org/10.1093/gji/ggz207>
- Reynolds, J. (2011). *An Introduction to Applied and Environmental Geophysics* (2nd ed.). Wiley-Blackwell.
- Rosas-Carbajal, M., Komorowski, J. C., Nicollin, F., & Gibert, D. (2016). Volcano electrical tomography unveils edifice collapse hazard linked to hydrothermal system structure and dynamics. *Scientific Reports*, 6. <https://doi.org/10.1038/srep29899>
- Sæmundsson, K., Sigurgeirsson, M., & Friðleifsson, G. Ó. (2020). Geology and structure of the Reykjanes volcanic system, Iceland. *Journal of Volcanology and Geothermal Research*, 391. <https://doi.org/10.1016/j.jvolgeores.2018.11.022>
- Sigurðsson, F., Kristmansdóttir, H., & Þórhallson, S. (1995). *Freshwater and seawater on Reykjanes and Reykjanes Peninsula*.
- Sigurdsson, O. (2010). The Reykjanes Seawater Geothermal System-Its exploitation under regulatory constraints. *Proceedings World Geothermal Congress*.
- Singha, K., Day-Lewis, F. D., Johnson, T., & Slater, L. D. (2015). Advances in interpretation of subsurface processes with time-lapse electrical imaging. *Hydrological Processes*, 29(6), 1549–1576. <https://doi.org/10.1002/hyp.10280>
- Slater, L., Binley, A. M., Daily, W., & Johnson, R. (2000). Cross-hole electrical imaging of a controlled saline tracer injection. *Journal of Applied Geophysics*, 44(2–3), 85–102. [https://doi.org/10.1016/S0926-9851\(00\)00002-1](https://doi.org/10.1016/S0926-9851(00)00002-1)
- Smith, D. L. (1986). Application of the pole-dipole resistivity technique to the detection of solution cavities beneath highways. *GEOPHYSICS*, 51(3), 833–837. <https://doi.org/10.1190/1.1442135>
- Soueid Ahmed, A., Revil, A., Byrdina, S., Coperey, A., Gailler, L., Grobde, N., Viveiros, F., Silva, C., Jougnot, D., Ghorbani, A., Hogg, C., Kiyani, D., Rath, V., Heap, M. J., Grandis, H., & Humaida, H. (2018). 3D electrical conductivity tomography of volcanoes. *Journal of Volcanology and Geothermal Research*, 356, 243–263. <https://doi.org/10.1016/j.jvolgeores.2018.03.017>
- Sternbergh, S. (2016). *Reykjanes Grey Lagoon: Precipitate chemistry and implications for metal rich scale precipitation, submarine hydrothermal vents, and environmental impact*. Reykjavik University.

- Symonds, R. B., Gerlach, T. M., & Reed, M. H. (2001). Magmatic gas scrubbing: implications for volcano monitoring. *Journal of Volcanology and Geothermal Research*, 108(1–4), 303–341. [https://doi.org/10.1016/S0377-0273\(00\)00292-4](https://doi.org/10.1016/S0377-0273(00)00292-4)
- Tarchini, L., Ranaldi, M., Carapezza, M. L., Di Giuseppe, M. G., Isaia, R., Lucchetti, C., Prinzi, E. P., Tramparulo, F. D., Troiano, A., & Vitale, S. (2019). Multidisciplinary studies of diffuse soil CO₂ flux, gas permeability, self-potential, soil temperature highlight the structural architecture of fondi di baia craters (Campi Flegrei Caldera, Italy). *Annals of Geophysics*, 62(1), 1–12. <https://doi.org/10.4401/AG-7683>
- Telford, W., Geldart, L., & Sheriff, R. (1990). Resistivity Methods. In *Applied Geophysics* (pp. 522–577). Cambridge University Press. <https://doi.org/10.1017/CBO9781139167932.012>
- Thibaut, R., Kremer, T., Royen, A., Kim Ngun, B., Nguyen, F., & Hermans, T. (2021). A new workflow to incorporate prior information in minimum gradient support (MGS) inversion of electrical resistivity and induced polarization data. *Journal of Applied Geophysics*, 187. <https://doi.org/10.1016/j.jappgeo.2021.104286>
- Thordarson, T., & Hoskuldsson, A. (2002). *Iceland*. Dunedin Academic Press.
- Tikhonov, A. N., Goncharsky, A. V., Stepanov, V. V., & Yagola, A. G. (1995). Numerical Methods for the Solution of Ill-Posed Problems. In *Numerical Methods for the Solution of Ill-Posed Problems*. Springer Netherlands. <https://doi.org/10.1007/978-94-015-8480-7>
- Troiano, A., Isaia, R., Di Giuseppe, M. G., Tramparulo, F. D. A., & Vitale, S. (2019). Deep Electrical Resistivity Tomography for a 3D picture of the most active sector of Campi Flegrei caldera. *Scientific Reports*, 9(1). <https://doi.org/10.1038/s41598-019-51568-0>
- Turner, G., Ingham, M., Bibby, H., & Keys, H. (2011). Resistivity monitoring of the tephra barrier at Crater Lake, Mount Ruapehu, New Zealand. *Journal of Applied Geophysics*, 73(3), 243–250. <https://doi.org/10.1016/j.jappgeo.2011.01.006>
- Uhlemann, S., Chambers, J., Wilkinson, P., Maurer, H., Merritt, A., Meldrum, P., Kuras, O., Gunn, D., Smith, A., & Dijkstra, T. (2017). Four-dimensional imaging of moisture dynamics during landslide reactivation. *Journal of Geophysical Research: Earth Surface*, 122(1), 398–418. <https://doi.org/10.1002/2016JF003983>
- Vaisala. (2023). *Carbon Dioxide Measurements*. <https://www.vaisala.com/en/measurement/carbon-dioxide-co2-measurements>
- Van Riet, B., Six, S., Walraevens, K., Vandenbohede, A., & Hermans, T. (2022). Assessing the Impact of Fractured Zones Imaged by ERT on Groundwater Model Prediction: A Case Study in a Chalk Aquifer in Voort (Belgium). *Frontiers in Water*, 3. <https://doi.org/10.3389/frwa.2021.783983>
- Villasante-Marcos, V., Finizola, A., Abella, R., Barde-Cabusson, S., Blanco, M. J., Brenes, B., Cabrera, V., Casas, B., De Agustín, P., Di Gangi, F., Domínguez, I., García, O., Gomis, A., Guzmán, J., Iribarren, I., Levieux, G., López, C., Luengo-Oroz, N., Martín, I., ... Trigo, P. (2014). Hydrothermal system of Central Tenerife Volcanic Complex, Canary Islands (Spain), inferred from self-potential measurements. *Journal of Volcanology and Geothermal Research*, 272, 59–77. <https://doi.org/10.1016/j.jvolgeores.2013.12.007>

- Waxman, M. H., & Smits, L. J. M. (1968). Electrical Conductivities in Oil-Bearing Shaly Sands. *Society of Petroleum Engineers Journal*, 8(02), 107–122. <https://doi.org/10.2118/1863-A>
- Wild, J., Kopecký, M., Macek, M., Šanda, M., Jankovec, J., & Haase, T. (2019). Climate at ecologically relevant scales: A new temperature and soil moisture logger for long-term microclimate measurement. *Agricultural and Forest Meteorology*, 268, 40–47. <https://doi.org/10.1016/j.agrformet.2018.12.018>
- Wu, Y., Hubbard, S., Williams, K. H., & Ajo-Franklin, J. (2010). On the complex conductivity signatures of calcite precipitation. *Journal of Geophysical Research: Biogeosciences*, 115(G2), n/a-n/a. <https://doi.org/10.1029/2009jg001129>
- Yamaoka, K., Geshi, N., Hashimoto, T., Ingebritsen, S. E., & Oikawa, T. (2016). Special issue “the phreatic eruption of Mt. Ontake volcano in 2014” the Phreatic Eruption of Mt. Ontake Volcano in 2014 5. Volcanology. In *Earth, Planets and Space* (Vol. 68, Issue 1). Springer Berlin. <https://doi.org/10.1186/s40623-016-0548-4>
- Zlotnicki, J., & Nishida, Y. (2003). Review on Morphological Insights of Self-Potential Anomalies on Volcanoes. *Surveys in Geophysics*, 24(4), 291–338. <https://doi.org/10.1023/B:GEOP.0000004188.67923.ac>

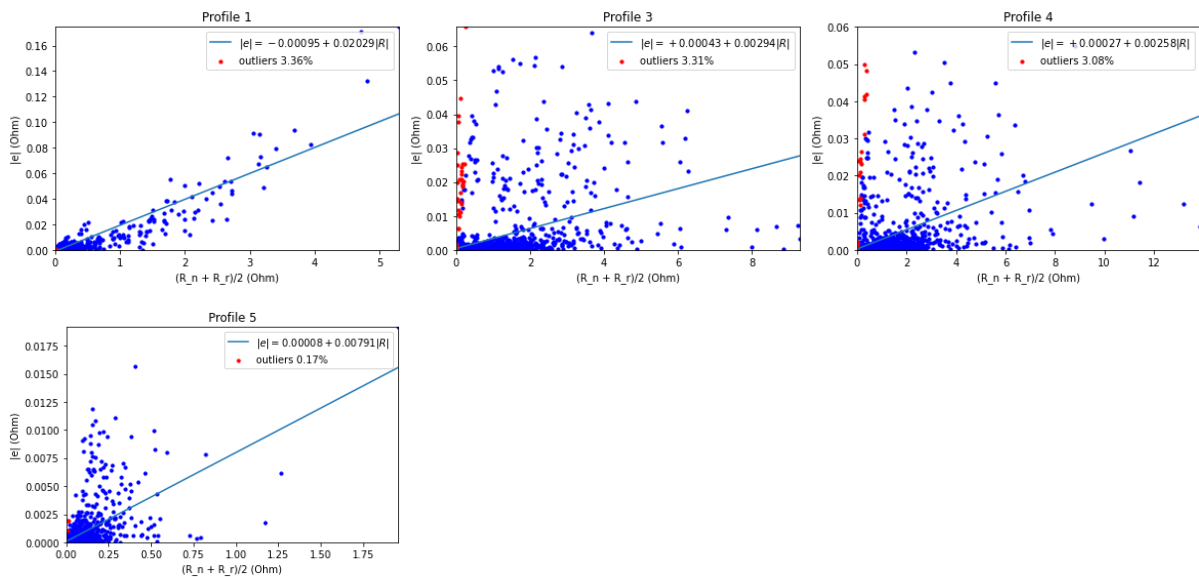
Appendices

A. Grid

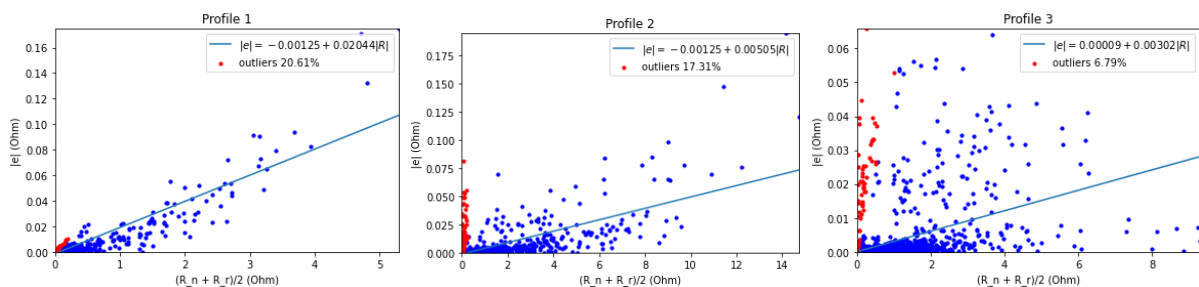


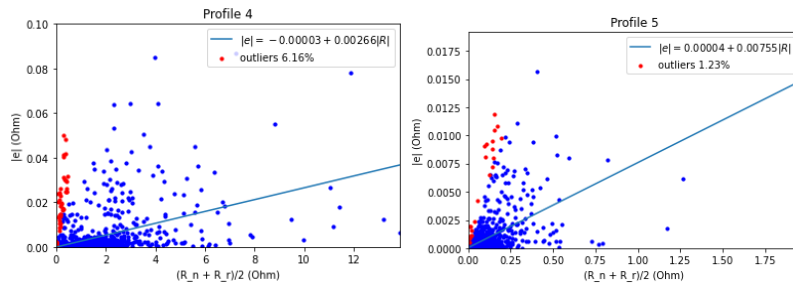
B. Characterization study

Error models of characterization profiles: 10 % threshold

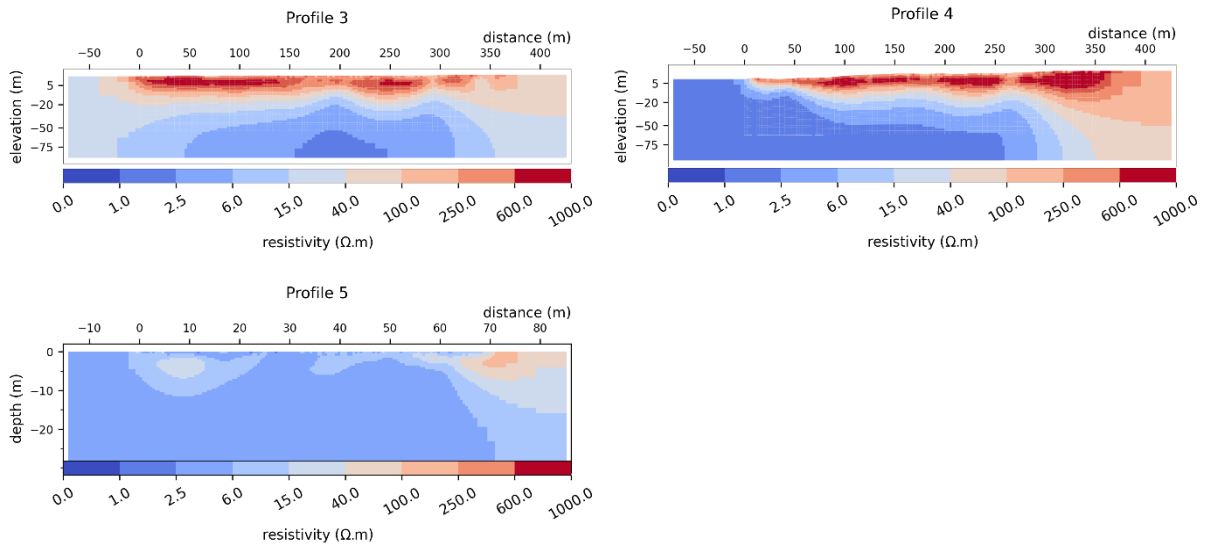


Error models of characterization profiles: 5 % threshold

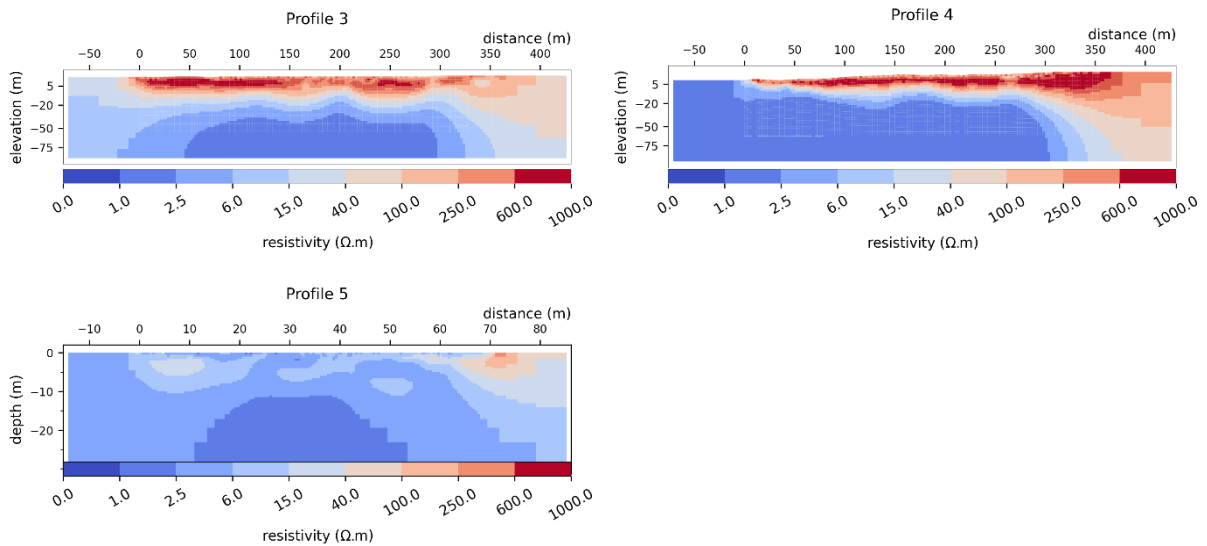




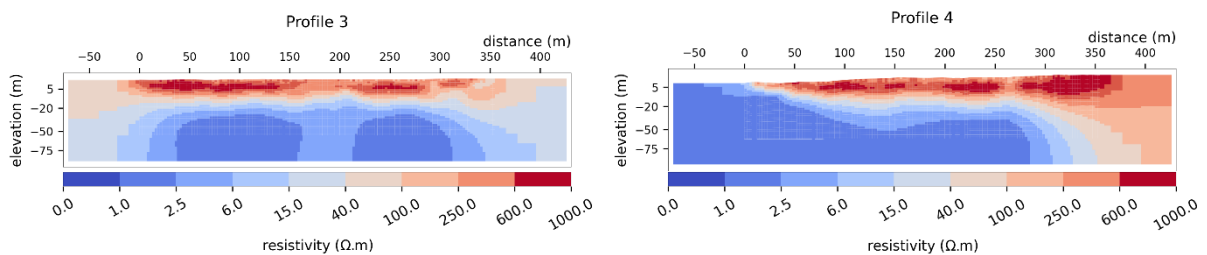
Absolute inversions with the constant error model: resistivity models

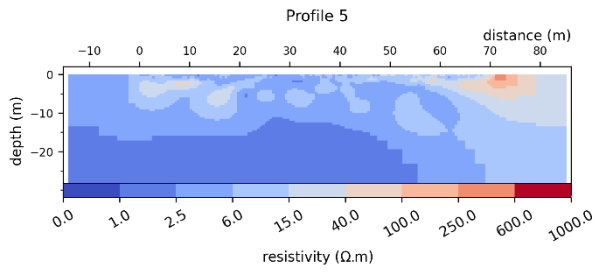


Absolute inversions with the variable error model: resistivity models

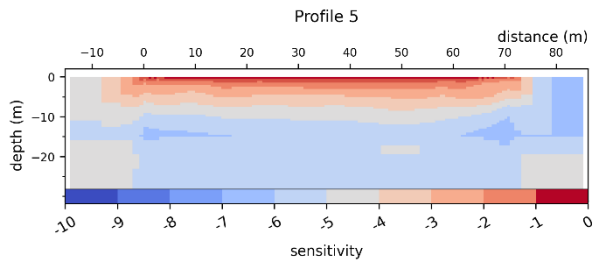
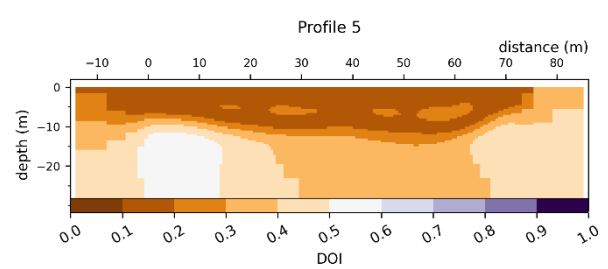
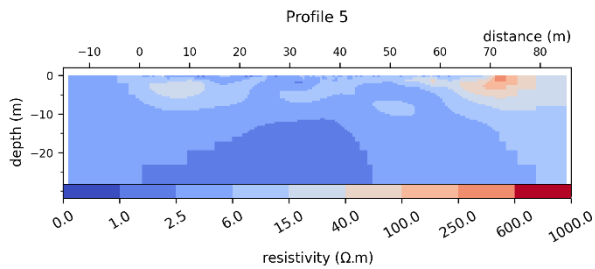
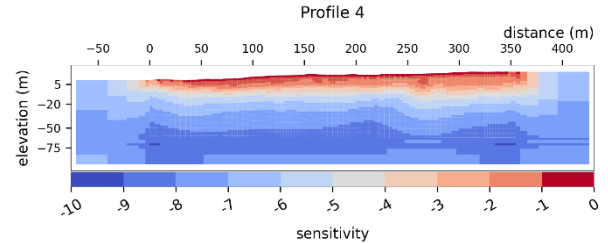
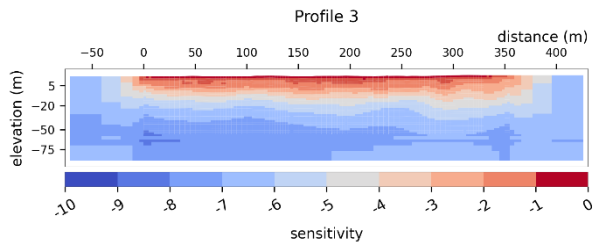
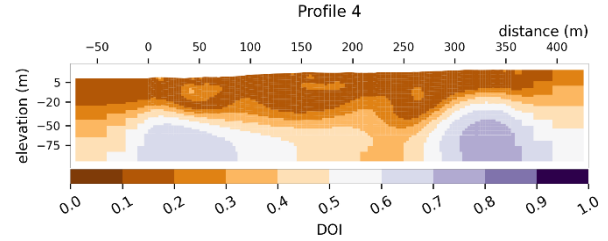
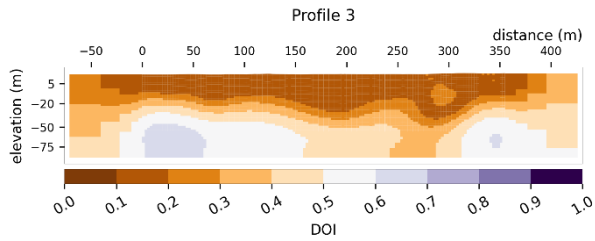
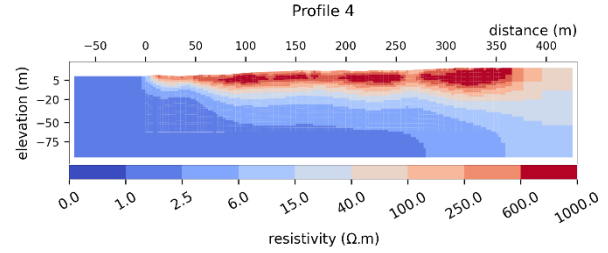
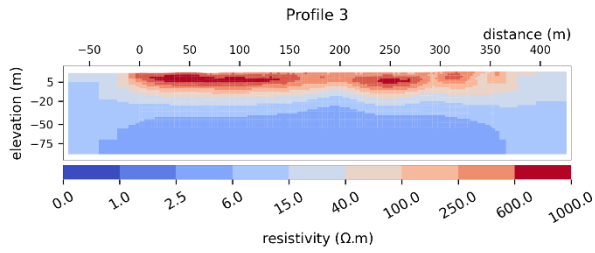


Absolute inversions with the individual error: resistivity models

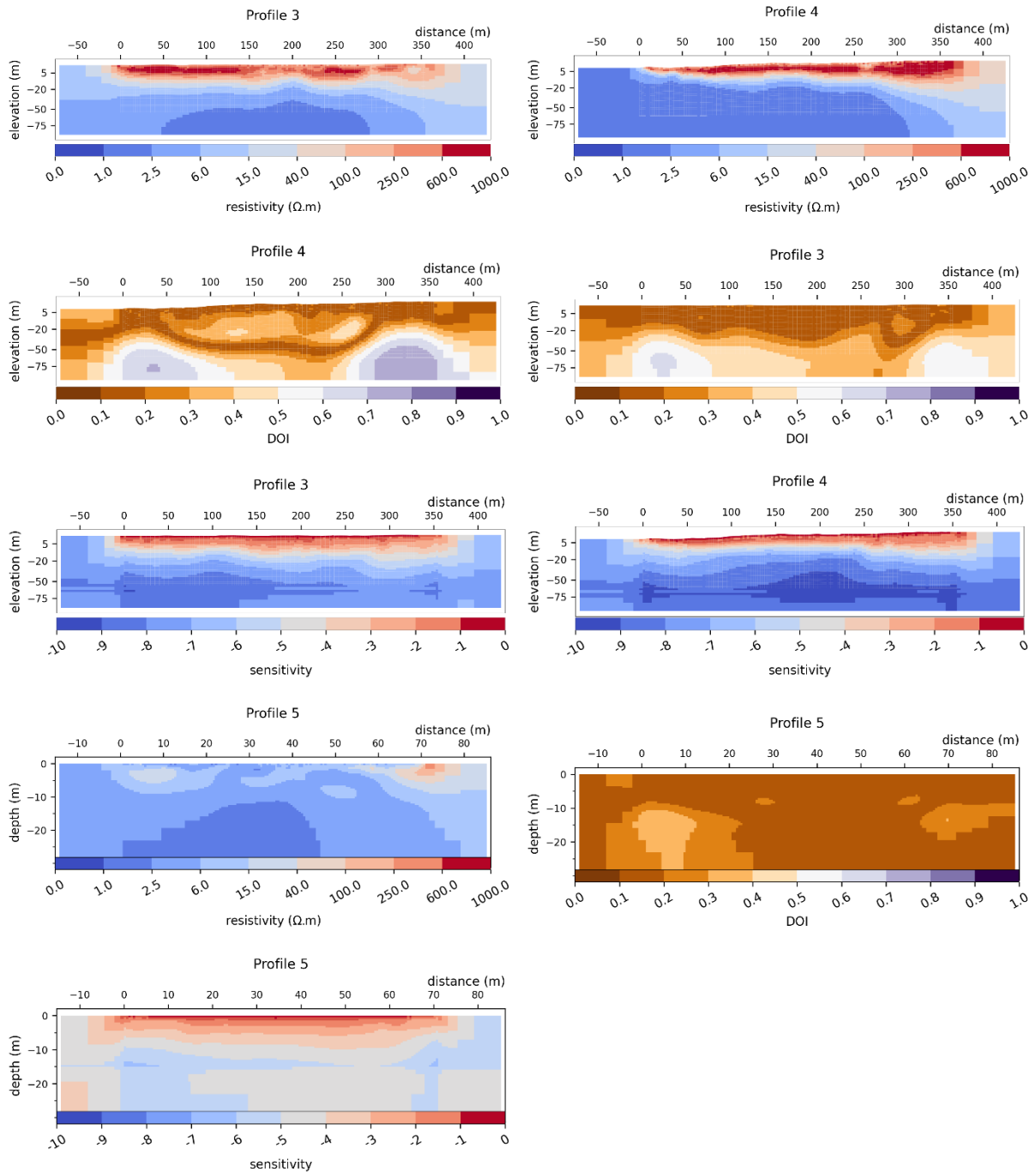




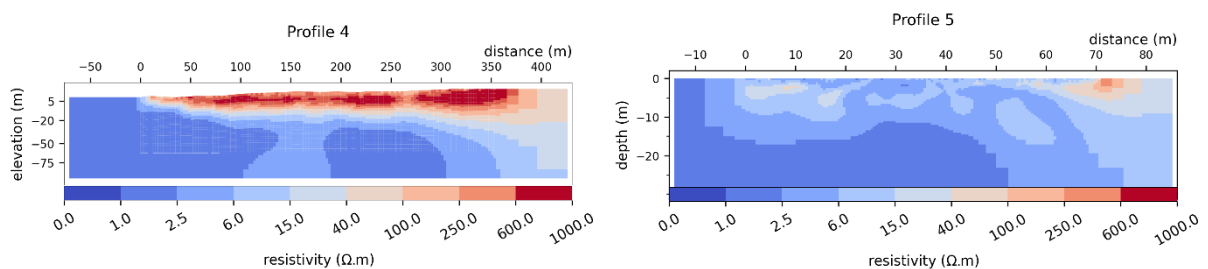
**Absolute inversions with a homogeneous reference model and the constant error model:
resistivity, DOI and sensitivity models**

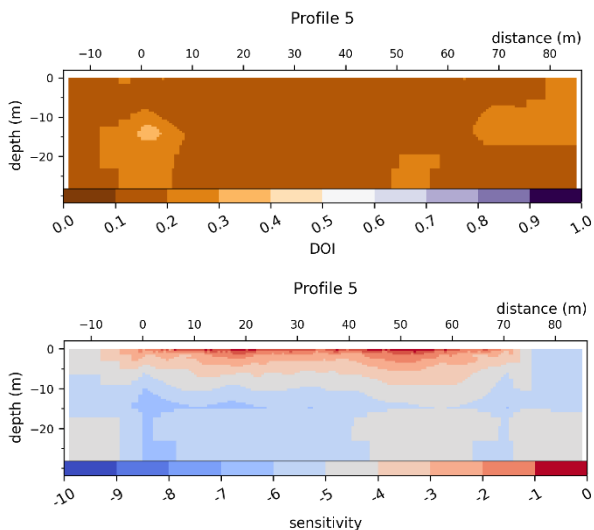
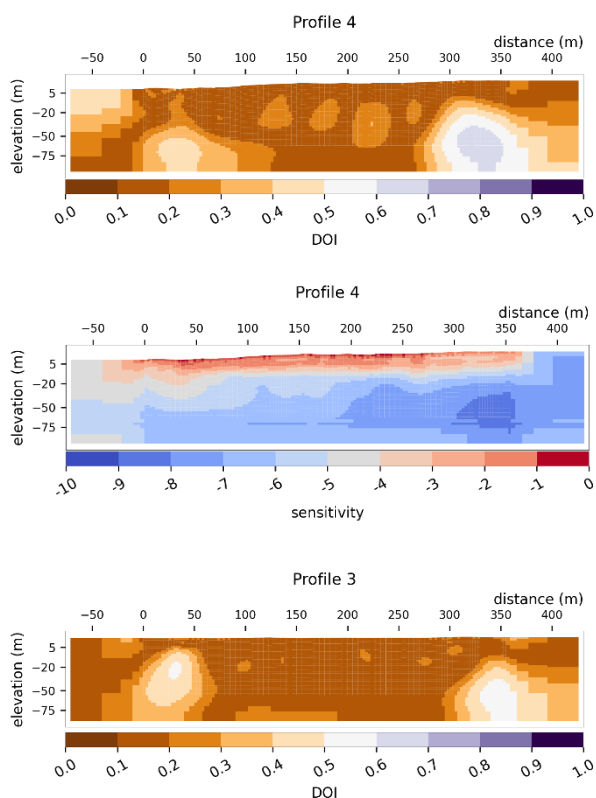


**Absolute inversions with a homogeneous reference model and the variable error model:
resistivity, DOI and sensitivity models**



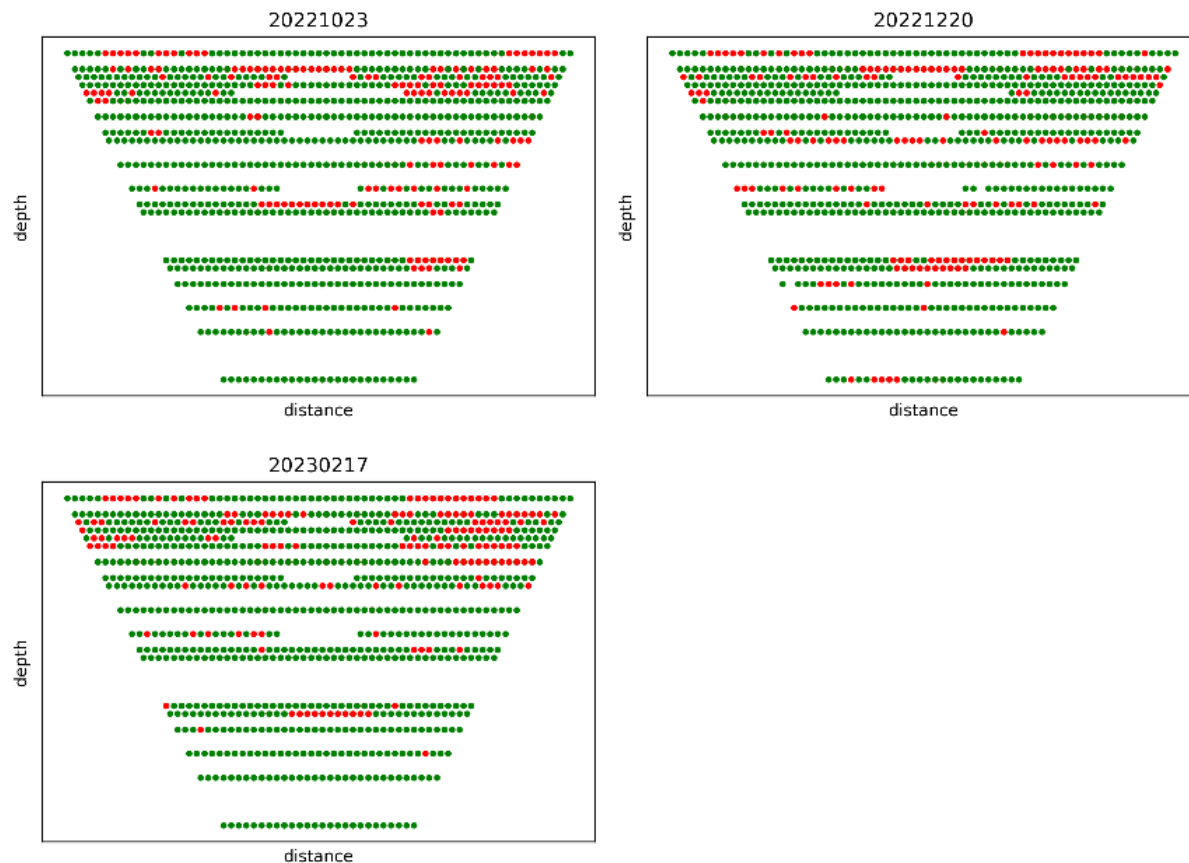
**Absolute inversions with a homogeneous reference model and the individual error: resistivity,
DOI and sensitivity models**



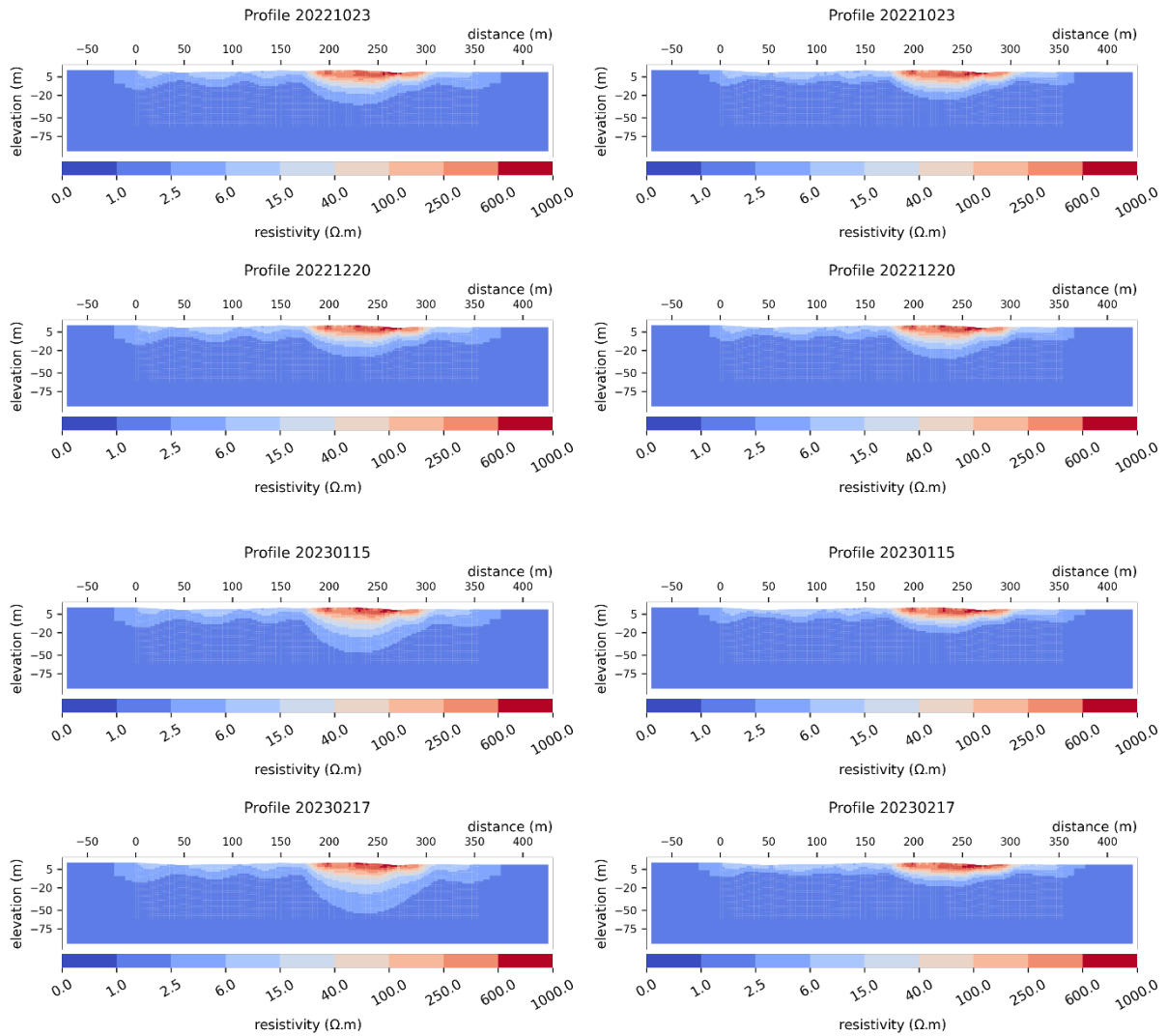


C. Monitoring study

Pseudosections with outliers



Absolute inversions: resistivity models with the constant (left column) and the variable (right column) error model



Absolute inversions with a homogeneous reference model with the constant (left column) and the variable (right column) error model: resistivity, DOI and sensitivity models

